Progress in numerical modeling of non-premixed combustion

Thesis by

Yuan Xuan

In Partial Fulfillment of the Requirements

for the Degree of

Doctor of Philosophy

California Institute of Technology

Pasadena, California

2014

(Defended May 12, 2014)

Acknowledgements

Funding from the U.S. Department of Energy-Basic Energy Sciences (DE-SC006591) is gratefully acknowledged. This research used computing resources of the National Energy Research Scientific Computing Center, which is supported by the Office of Science of the U.S. Department of Energy under Contract No. DE-AC02-05CH11231. This research also used the computing resources of the Extreme Science and Engineering Discovery Environment (XSEDE), which is supported by National Science Foundation grant number OCI-1053575.

This work has benefited greatly from discussions with many graduate students, post-doctoral fellows, and professors at the Graduate Aerospace Laboratories, among them, Siddhartha Verma, Phares Carroll, Gerry Della Rocca, Jason Rabinovitch, Shyam Menon, Pauline Vervisch, Remy Mevel, and Professor Beverley McKeon. I also deeply acknowledge Dr. Christopher Shaddix at Sandia National Laboratories and Professor Michael Mueller at Princeton University, Professor Christian Hasse at Freiberg University of Mining and Technology, and Professor Nobert Peters at RWTH Aachen for their valuable comments and fruitful discussions.

I would like to thank specifically my graduate research advisor, Professor Guillaume Blanquart, for the support, patience, and encouragement that he has given to me. I would also like to thank my committee members, Professors Joseph Shepherd, Dan Meiron, and Dale Pullin for their helpful comments on this thesis.

Abstract

Progress is made on the numerical modeling of both laminar and turbulent non-premixed flames. Instead of solving the transport equations for the numerous species involved in the combustion process, the present study proposes reduced-order combustion models based on local flame structures.

For laminar non-premixed flames, curvature and multi-dimensional diffusion effects are found critical for the accurate prediction of sooting tendencies. A new numerical model based on modified flamelet equations is proposed. Sooting tendencies are calculated numerically using the proposed model for a wide range of species. These first numerically-computed sooting tendencies are in good agreement with experimental data. To further quantify curvature and multi-dimensional effects, a general flamelet formulation is derived mathematically. A budget analysis of the general flamelet equations is performed on an axisymmetric laminar diffusion flame. A new chemistry tabulation method based on the general flamelet formulation is proposed. This new tabulation method is applied to the same flame and demonstrates significant improvement compared to previous techniques.

For turbulent non-premixed flames, a new model to account for chemistry-turbulence interactions is proposed. The validity of various existing flamelet-based chemistry tabulation methods is examined, and a new linear relaxation model is proposed for aromatic species. The proposed relaxation model is validated against full chemistry calculations. To further quantify the importance of aromatic chemistry-turbulence interactions, Large-Eddy Simulations (LES) have been performed on a turbulent sooting jet flame. The effects of turbulent unsteadiness on soot are highlighted by comparing the LES results with a separate LES using fully-tabulated chemistry. It is shown that turbulent unsteady effects are of critical importance for the accurate prediction of not only the inception locations, but also the magnitude and fluctuations of soot.

Contents

List of Figures

List of Tables

Chapter 1

Introduction

1.1 Background

Energy sustainability and the emission of pollutants will have defining importance in the present century[1]. Historically, the combustion of hydrocarbon fuels has been the principal source of energy due to their high energy density, ease of transport, and relative abundance. Although renewable energy and nuclear power are the world's fastest-growing energy resources, fossil fuels are estimated to continue to supply almost 80 percent of the world's energy through 2040, as reported in the International Energy Outlook (2013 report) [1]. Unfortunately, the combustion of fossil fuels not only generates greenhouse gases, but also produces pollutants, such as nitrogen oxides, sulfur dioxide, volatile organic compounds, and nano-sized particles, which can cause severe air quality degradation. Ever more stringent international regulations (e.g. ICAO CAEP2 standards) placed on industrial combustion system emissions make the design of cleaner and more efficient combustion devices a necessity.

The development of clean and efficient combustion systems introduces new challenges, not only in the manufacturing of these systems, but also at a more fundamental level. Although designs of the various combustion systems and their operating conditions may be very different, the turbulent reacting flows involved are subject to the same complexities. First, hundreds of species and thousands of reactions are generally required to describe correctly the chemical aspect of combustion [2, 3, 4, 5]. Second, the wide range of length and time scales present in turbulent reacting flows increases

the complexity of the systems [6]. Finally, but most importantly, the major complexity found in these combustion systems is due to the intrinsic interactions between small scale chemical processes and large scale flow features. These multi-physics and multi-scale problems are among the biggest challenges in fluid mechanics and are the real limiting factors in the development of more efficient and cleaner energy sources.

1.2 Computational modeling of non-premixed reacting flows

Towards this end, Computational Fluid Dynamics (CFD) has emerged as an indispensable industrial analysis and design tool over the past few decades. Its application to the modeling of complex reacting flows has been largely successful [7, 8, 9, 10]. However, the predictive capabilities of CFD tools remain limited by the assumptions and approximations made in the modeling of key physical processes. For instance, some modeling procedures that have been widely used in numerical combustion were developed for non-reacting, constant density flows [11, 12, 13, 14, 15]. These models were developed based on physical arguments with simplifying assumptions, and as a result, have demonstrated inconsistencies when applied in practical situations. This is reflected by the large variety of different combustion models that have been formulated [16] and the continuous effort that has been made to improve these models [6, 16].

One such research effort is the International Sooting Flame (ISF) workshop [17]. This open forum aims to identify common research priorities in the development and validation of accurate, predictive models for sooting flames and to coordinate research programs at the international level to address them. Well-defined target flames that are particularly suitable for model development and validation have been selected, spanning a variety of fuels and flame types, including laminar flames, turbulent flames, and pressurized flames. To enable accurate and efficient investigations of these laboratory-scale sooting flames, the current work aims to develop reliable computational tools for the modeling of laminar and turbulent non-premixed flames under atmospheric pressure.

1.3 Direct numerical simulations

In view of the difficulties in the reduced-order modeling of combustion, Direct Numerical Simulations (DNS) with finite-rate chemistry may seem to be more advantageous, since all the governing equations are solved in these simulations, without using any explicit simplifying assumptions. Indeed, DNS has been employed as a valuable research tool, and recent development in high-performance computing has enabled the application of DNS to more and more complex configurations [18, 19]. Some of the most recent DNS studies of non-premixed reacting flows with finite-rate chemistry are included in the following figure.

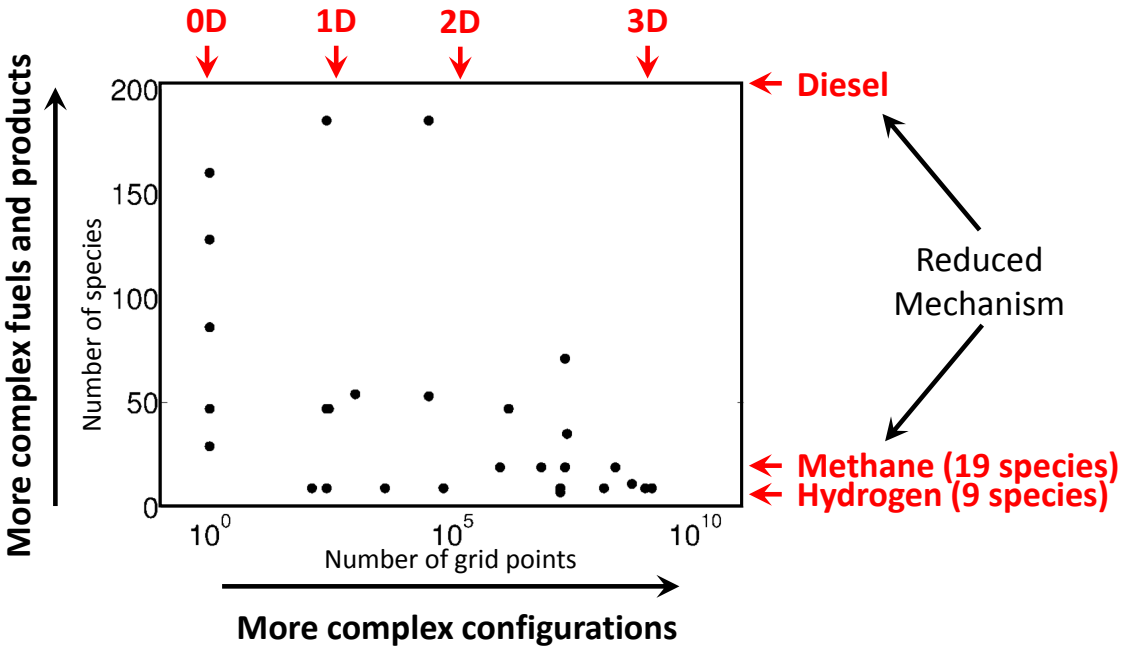

Figure 1.1: Recent DNS studies of non-premixed reacting flows with finite-rate chemistry.

DNS with finite-rate chemistry has been applied to zero-dimensional homogeneous reactor simulations [20, 21] and one-dimensional flame calculations [22, 23, 24, 25, 26] using detailed chemical mechanisms involving a large number of species. However, only skeleton-level chemical mechanisms have been used in three-dimensional turbulent non-premixed reacting flow simulations [27, 28, 29, 30, 31, 32]. Such chemical mechanisms are not sufficiently accurate for the combustion of large hydrocarbon fuels, especially for (the surogates of) practical fuels (*e.g.* diesel), and are not able

to provide a satisfactory description of complex chemical processes, such as low-temperature combustion and soot formation. Overall, the application of DNS with finite-rate chemistry to practical combustion systems using practical fuels (*e.g.* diesel) as a design tool is still prohibited by the associated extremely high computational cost. This is essentially due to the large number of species and reactions involved in the combustion process and the wide range of time and length scales that need to be resolved in the reacting flow field.

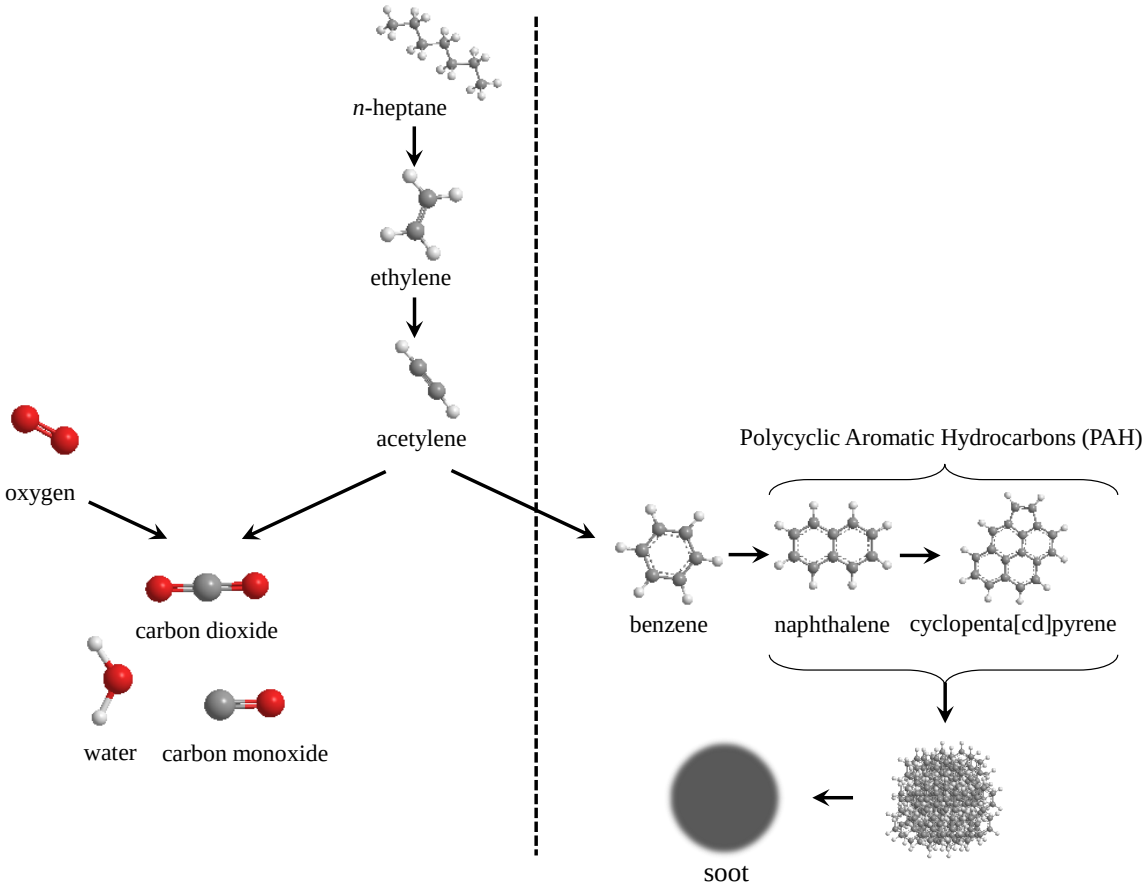

Figure 1.2: Schematic of the combustion of n-heptane. The part to the left of the dash line does not include any aromatic chemistry.

The general picture of the combustion of n-heptane is shown in Fig. 1.2. This fuel is representative of all alkane fuels and is known to be an important component for gasoline, diesel, and kerosene surrogates. N-heptane first goes through thermal cracking by having hydrogen atom abstraction and β-scission reactions. This process leads to the formation of important intermediate species such

as ethylene and acetylene. These species react with oxygen to form major combustion products such as carbon monoxide, carbon dioxide, and water. Simultaneously, these intermediate species (*e.g.* ethylene and acetylene) react with each other, which leads to the formation of the first aromatic species, namely benzene. Larger aromatic species with more than one aromatic rings, such as naphthalene, phenanthrene, and pyrene are then formed from benzene [2, 3]. Further collisions between these large aromatic compounds lead to the formation of soot particles [2, 3]. Typically hundreds of species and thousands of reactions are required to capture accurately enough the combustion process just described [3, 33]. Including such detailed chemical kinetics model burdens substantially reacting flow simulations, due to the large number of transported reactive scalars (*i.e.* species mass fraction).

Moreover, simulations of reacting flow systems using finite-rate chemistry are extremely challenging due to the multiple time scales involved in the various physical and chemical processes [34, 35, 36]. In particular, chemistry produces generally very small time scales which make the systems stiff. The high non-linearity in the Arrhenius form of the chemical reaction rate constants in the calculations of the species chemical source terms increases the stiffness of the systems [37]. In addition, for turbulent reacting flows, the difference between the thickness of the thin reaction layers (often smaller than the Kolmogorov length scale) and the largest length scale is typically more than three orders of magnitude [32, 31]. As a result, billions of grid points are generally required for the DNS of these flows [30, 38]. Although advanced numerical schemes have been designed for more accurate scalar transport [39, 40, 41] and more efficient time-integration of stiff chemical source terms [37, 20], DNS of reacting flows with complex chemistry under complex configurations are still limited by the current computing resources.

As a result of all these challenges, detailed chemical mechanisms have been included in the DNS of reacting flows, but only for relatively simple geometries (*e.g.* homogeneous reactors and statistically one-dimensional flames) [20, 23]. The number of species included in the DNS of two-dimensional and three-dimensional reacting flows has been very limited [32, 31, 30, 27, 42, 28]. Most of these simulations have only investigated the combustion of relatively simple fuels (*e.g.* methane

and hydrogen), and have taken into account only the major chemical pathways without considering aromatic species and soot formation (the part to the left of the dash line in Fig. 1.2). Typically, the chemical mechanism used for hydrogen combustion in these simulations contains 9 species [30, 27, 28] and the one used for methane combustion contains 19 species [32, 31, 30, 28]. These mechanisms have been obtained by reducing the number of intermediate species contained in detailed mechanisms using chemistry reduction techniques, such as Quasi-State-State (QSS) assumptions [43] and Partial-Equilibrium (PE) approximations [44]. Simulations using these reduced mechanisms are able to capture the major features of the reacting flows under investigation, for instance temperature and major species distributions [32, 30, 28]. However, reduced chemical mechanisms become insufficient when the combustion of large hydrocarbon fuels (practical fuels) or the formation of complex combustion products (soot) is considered. As mentioned earlier, describing accurately such complex chemical processes requires typically hundreds of species and thousands of reactions [2, 3, 4]. The efficient integration of detailed chemical kinetics into detailed simulations of reacting flows presents one of the biggest challenges in numerical combustion. One approach to overcome the difficulties discussed above is to use chemistry tabulation. The different categories of chemical kinetics integration strategies discussed are summarized in the following figure.

1.4 Chemistry tabulation

Instead of reducing the number of species considered in the chemical mechanisms, chemistry tabulation keeps the detailed mechanisms unchanged, but reduces the number of independent variables (to be solved in CFD simulations) to a tractable number. Therefore, chemistry tabulation is very attractive for both its computational efficiency and its ability to maintain a high chemical accuracy. The reduction of independent variables can be achieved using for instance the method of Computational Singular Perturbations (CSP) [34, 45] and the method of Intrinsic Low-Dimensional Manifold (ILDM) [35, 36]. These methods use the fact that many of the chemical time scales involving intermediates in the reaction chains are fast and not rate-limiting. By suppressing these fast reactions and placing the species involved therein in steady-state, the thermochemical state of

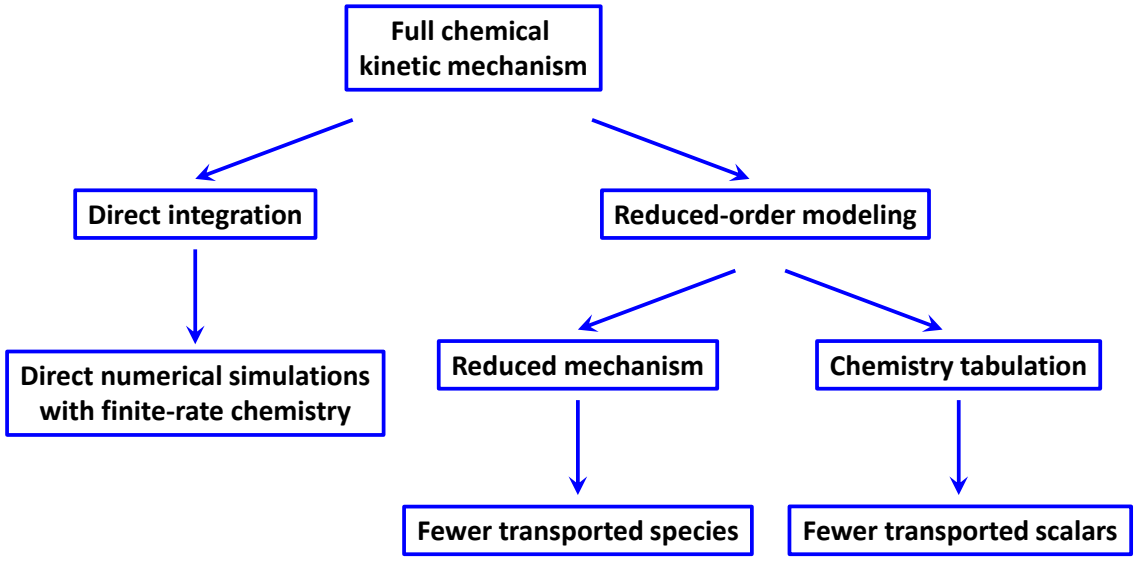

Figure 1.3: Different categories of chemical kinetics integration strategies.

the system depends on a much smaller number of variables. These variables are often combinations of species concentrations. Multi-dimensional libraries are then used to store the thermochemical states as a function of these variables. These methods are particularly suited for chemical kinetics calculations [46]. Unfortunately, these methods do not include any flow variables (*e.g.* flow strain rate, flame curvature, and scalar dissipation rate) in constructing the libraries of thermochemical states. As a result, they are limited when applied to non-premixed flames, where the local reacting flow is governed by the balance between chemistry and diffusion [16].

An interesting alternative to chemical-kinetics-based tabulation methods is the flame-structure-based tabulation methods. Such methods include the Flame Prolongation of ILDM (FPI) [47], and the Flamelet-Generated Manifold (FGM) [48]. These methods share remarkable similarities and both rely on the concept of the steady-state Laminar Diffusion Flamelet (LDF) [49, 50]

1.5 Steady-state laminar diffusion flamelets

The notion of mixture fraction was introduced by Bilger [51] as a measure of the local fuel/oxidizer ratio in non-premixed reacting flows. The steady-state LDF model based on the mixture fraction,

Z, as an independent variable, and using the scalar dissipation rate, $\chi = 2D|\nabla Z|^2$, for the mixing process, was introduced by Peters in 1983 [49] (see Eq. 3.1 in Section 3.2.1). Historically, Williams was the first to rewrite, under unity Lewis number assumption, the species transport equations by separating the diffusion normal to mixture fraction iso-contours and that in tangential directions [52]. Peters introduced additional simplifications to make use of the flamelet formulation in reacting flow simulations, namely, combustion processes take place in a thin layer close to the flame front, diffusion in the direction parallel to the local iso-surface of mixture fraction is negligible, and the local flame surfaces are essentially flat. Based on these three assumptions, multi-dimensional non-premixed flames can be modeled as an ensemble of piecewise one-dimensional flame structures, termed flamelets. The LDF model has been a popular modeling approach in simulating both laminar non-premixed flames [53, 54, 55] and turbulent non-premixed flames [56, 57, 58, 59, 60, 61, 22, 62].

The distinct advantage offered by the flamelet model, compared to the numerical simulation using finite-rate chemistry model, is that flow properties and chemical kinetics are essentially decoupled [6]. More specifically, steady-state flamelet equations are solved in advance to build a flamelet database. This database is then tabulated as a function of the mixture fraction, Z, and the scalar dissipation rate, χ, as shown in Fig. 1.4. In simulations, the values of Z and χ are computed locally, based on

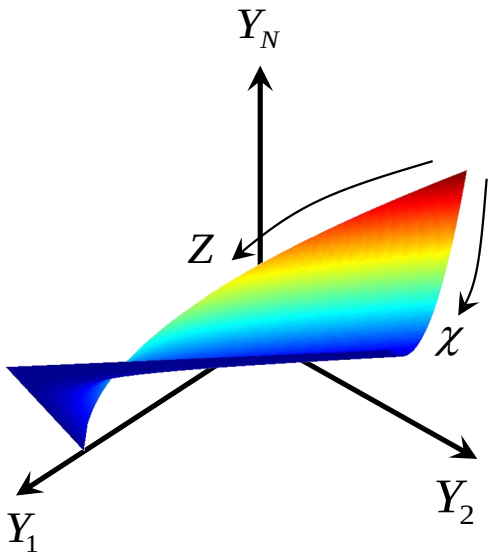

Figure 1.4: Illustration of flamelet database for chemistry tabulation generated using the solutions to steady-state flamelet equations.

which the species mass fraction, temperature, and other thermochemical properties are evaluated. As such, the computational cost associated with simulations using flamelet-based tabulated chemistry methods is significantly lower than using finite-rate chemisty, since only the scalar quantities Z and χ need to be calculated locally, without solving the transport equations of all species involved in the chemical mechanism.

1.6 Flamelet-based modeling of laminar non-premixed flames

While being a very powerful modeling framework, the LDF model relies on several key assumptions which may not be valid in all laminar non-premixed flames. Potential impacts of these assumptions require further analysis. Furthermore, these impacts may be present not only in laminar flames, but also in turbulent flames. Yet, they are more pronounced in laminar flames [63].

The first key assumption concerns the species Lewis numbers. In most of the previously referenced studies of turbulent reacting flows [56, 58, 59], unity Lewis number transport has been assumed on the basis that molecular diffusion is negligible compared to turbulent mixing. The influence of non-unity Lewis number transport on turbulence-chemistry interaction has been investigated theoretically, experimentally, and numerically by previous work [63, 64, 65, 66, 67]. The unity-Lewis number assumption is found valid for large-scale mixing in the limit of sufficiently large Reynolds number; and the transition from non-unity (under laminar conditions) to unity Lewis number (under turbulent conditions) was observed for conditional means of species mass fractions in piloted turbulent methane/air jet flames as the Reynolds number was increased [63, 66]. For laminar flames, large deviations have been found in co-flow non-premixed flames when comparing results obtained with unity and non-unity Lewis numbers (e.g. significantly different flame heights and flame widths) [54, 68, 69].

The second key assumption concerns curvature effects which have been neglected [54, 22, 68, 70, 71], since the combustion of interest is assumed to occur very near to the flame front. Such close proximity to the flame front (defined as the iso-surface of stoichiometric mixture fraction) allows for the flame to be modeled as flat; therefore, curvature effects could be neglected. However,

many species of interest, such as aromatic species, tend to be located farther away from the flame, where the flame can no longer be assumed to be flat, and flame curvature effects could potentially be substantial. The impact of curvature can be further enhanced when mixture fraction iso-surfaces are highly wrinkled by turbulent motions [42]. In other words, curvature effects might be non-negligible when the product of flame curvature by the distance to the flame front is large. Unfortunately, the effects of flame curvature on the flamelet modeling of both laminar and turbulent non-premixed flames still remain not well understood.

The third key assumption concerns the multi-dimensional diffusion effects, *i.e.* in the direction parallel to the local iso-surface of mixture fraction. These effects have been neglected to achieve the one-dimensionality of the local flame structure. As such, all physical quantities can be parametrized solely by the mixture fraction. However, in a recent study, these multi-dimensional effects were found to be critical in reproducing the complete flame behavior in laminar co-flow diffusion flames [69] and hence might have non-negligible impact on sensitive processes, such as soot formation.

The first one-dimensional laminar flamelet equations were proposed by Peters [49, 50] for flat flames, under unity Lewis number assumption. These equations were extended by Pitsch [70] to take into account non-unity Lewis number effects. Williams proposed a more general flamelet formulation even before Peters without making specific assumptions on the flame structure [52, 72]. However, a unity Lewis number was assumed to describe the species transport processes, and the terms corresponding to different physical processes were grouped together, making this formulation hardly used in practice. More recently, Kortschik *et al.* [73] attempted to derive flamelet equations accounting for curvature effects. However, restrictive assumptions were made implicitly in the derivation. As a result, the predicted curvature effects did not show full agreement with the qualitative experimental observations [74]. More precisely, curvature was predicted to still have effects on species with Lewis number close to unity, but those species were observed to be hardly affected in the experiments. Xu *et al.* has also attempted to derive flamelet equations including curvature effects [75]. However, their formulation is valid only under specific conditions [75]. In summary, no mathematical framework is yet able to describe the combined effects of multi-dimensional effects, non-unity Lewis number, and

flame curvature using a flamelet formulation for laminar and mildly turbulent non-premixed flames.

1.7 Flamelet-based modeling of turbulent non-premixed flames

Unlike for laminar non-premixed flames, the conventional steady-state LDF model has been found to represent well the local turbulent flame structure, as briefly reviewed at the beginning of Chapter 5. Chemistry tabulation based on the steady-state LDF model has been widely applied to Large-Eddy Simulations (LES) of turbulent reacting flows, in which large length scales are resolved and small scale mixing is modeled. LES using LDF-based chemistry tabulation has been applied to a variety of combustion problems of practical interest including the prediction of pollutant emission [7, 8], combustion instabilities [76, 77], and aircraft engine combustion [9, 10]. Although major flame characteristics and main species concentrations are generally well predicted in these simulations, the extension to include more complex chemical products in these simulations should be done with great care.

As aforementioned, one substantial simplification implicitly made by the chemistry tabulation based on steady-state LDF model is that the characteristic chemical time scale is much smaller than that of turbulence. In other words, chemistry is assumed to respond infinitely fast to perturbations from the turbulent flow field. Such assumption may be valid for the major chemical species (reactants and products) as well as radicals (H, OH, O, *etc.*). For instance, the steady-state LDF model has been shown to represent remarkably well statistically averaged flame properties [63]. However, due to the wide range of time scales involved in turbulent flows and the large time scales characterizing the chemical processes of certain species, transient effects could be substantial. One of such critical processes is the formation of soot particles.

Due to the detrimental effects of soot emission on human health and the environment, substantial research efforts are presently devoted to the numerical prediction of soot formation in turbulent reacting flows [32, 42, 78]. As mentioned earlier, soot is believed to nucleate from Polycyclic Aromatic Hydrocarbons (PAH), which involve complex and slow chemical kinetics [2, 3]. Previous studies have shown that the concentrations of PAH in turbulent diffusion flames deviate from those predicted by

the steady-state LDF model [16, 42]. These observed differences are believed to be a consequence of the rapidly changing turbulent flow field and the slow adjustment of PAH chemistry. Based on the above consideration, turbulence-chemistry interaction needs to be properly treated for PAH molecules.

A series of theoretical studies have been focusing on the chemical response of the flamelets solutions to oscillatory strain rates under various flow conditions [79, 80, 81, 82]. Chemical responses of different species under oscillatory flow rates and strain rates have been also investigated in non-premixed flames numerically [83, 84] and experimentally [85, 86]. The scalar dissipation rate was found to characterize well the unsteadiness of the flow [83]. However, in these studies, emphasis has been placed on major combustion products and a very limited number of intermediate species.

Recent studies have focused on the effects of unsteadiness on the formation of NO_x species [8, 87] and a relaxation model [8] was proposed for the prediction of their mass fractions in turbulent flames, based on a one-step global reaction. Unfortunately, this relaxation model was only validated *a posteriori*. The situation is similar for PAH (*i.e.* no *a priori* analysis). Including transient effects for PAH molecules has been attempted by Mueller and Pitsch [22] by using the same model as for NO_x [8], despite the fact that PAH species are characterized by an even more complex chemistry than NO_x species. In their work, all PAH molecules were represented by a single lumped PAH species, and the dependence of the chemical source term on the PAH mass fraction was assumed to be universal for all PAH. While this represents a very good first step, a more reliable model based on a more complete *a priori* analysis is required to take into account the interactions between chemistry and turbulent unsteadiness. Such model should reflect the multi-step nature of PAH chemistry and distinguish between major PAH species.

Transient effects for PAH molecules have been included first in the LES of a laboratory-scale flame and an aircraft combustor by Mueller and Pitsch [22, 88]. They proposed to solve a transport equation for the lumped PAH variable using the PAH relaxation model discussed above. Although chemistry-turbulence interactions for PAH have already been included in LES, their effects and importance have never been investigated and characterized precisely.

1.8 Objective and outline

In view of the issues discussed above, the objective of the current study is to identify the key issues in the flame-structure-based reduced-order modeling of laboratory-scale laminar and turbulent sooting flames, with specific attention placed on the prediction of PAH species. As aforementioned, these PAH species are of critical importance since their concentrations control directly the soot nucleation rates. More precisely, the objectives are three-fold:

1) investigate the effects of flame curvature and multi-dimensional diffusion, and the appropriateness of the LDF model in the representation of local flame structures in laminar non-premixed flames,

2) examine the effects of turbulent perturbation on PAH species, and the validity of different chemistry tabulation strategies in the numerical modeling of turbulent non-premixed flames,

3) propose and validate more accurate flamelet-based reduced-order models for the key processes mentioned above and investigate their importance and effects in laboratory-scale flame configurations.

The manuscript is organized as follows. In Chapter 2, a brief summary of the governing equations for reacting flows under zero Mach number approximation is provided. In Chapter 3, the importance of multi-dimensional convection and diffusion effects and the validity of the LDF model are assessed in the context of predicting numerically sooting tendencies. Calculations using the conventional steady-state LDF model are performed and this model is shown to be inadequate in reproducing the correct species distributions on the centerline of the flame under study, where the sooting tendencies are defined. In an effort to overcome these deficiencies, a new numerical framework based on modified flamelet equations is proposed. The numerical sooting tendencies for both non-aromatic and aromatic test species are then calculated using the proposed model and compared against experimental measurements. In Chapter 4, a general, mathematically consistent flamelet formulation is derived to investigate the effects of curvature of mixture fraction iso-surfaces on the transport of species in laminar diffusion flames. Budget analysis is performed on an axisymmet-

ric laminar coflow diffusion flame to highlight the importance of the curvature-induced convective term compared to other terms in the full flamelet equation. A new chemistry tabulation method is developed based on the proposed curved flamelet formulation. A comparison is made between full chemistry simulation results and those obtained using planar and curved flamelet-based chemistry tabulation methods. In Chapter 5, it is first highlighted that the various issues in the flamelet-based modeling of laminar non-premixed flames become negligible in turbulent non-premixed flames. Instead, non-equilibrium chemistry effects represent the key modeling challenge for these flames. The chemical responses of the local flame structure subjected to turbulent perturbations are examined. Based on these unsteady flamelet results, the validity of various existing flamelet-based chemistry tabulation methods is examined, and a new linear relaxation model is proposed for PAH species. The proposed relaxation model is validated through the unsteady flamelet formulation, and results are compared against full chemistry calculations. In Chapter 6, the effects of aromatic chemistry-turbulence interactions are investigated by applying the PAH realxation model, proposed in the previous chapter, to an ethylene/air piloted turbulent sooting jet flame. The effects of turbulent unsteadiness on soot yield and distribution are highlighted by comparing the LES results with a separate LES using tabulated chemistry for all species including the aromatic species. Results from both simulations are compared to experimental measurements. Major conclusions of the current work and recommendations for future research directions are provided in Chapter. 7.

Chapter 2

Governing equations and numerical solver

The evolution of the reacting flows under study is governed by the unsteady Navier-Stokes equations and the scalar transport equations. For the simulations undertaken in this work, we adopt the standard zero Mach number assumption that is well justified for many combustion systems and has been used in many previous studies [22, 89, 90, 29, 91], as the typical Mach number for both laminar and turbulent diffusion flames is well below 0.1.

2.1 Governing equations

Using the zero Mach number approximation, the continuity and momentum equations are written as

$$\frac{\partial \rho}{\partial t} + \nabla \cdot (\rho \mathbf{u}) = 0, \tag{2.1}$$

$$\frac{\partial \rho \mathbf{u}}{\partial t} + \nabla .(\rho \mathbf{u}\mathbf{u}) = -\nabla p + \nabla \cdot \tau, \tag{2.2}$$

where ρ is the density, p is the pressure, $\mathbf{u}$ is the velocity, and τ is the deviatoric stress tensor, defined as

$$\tau = \mu \left[\nabla \mathbf{u} + (\nabla \mathbf{u})^T \right] - \frac{2}{3}\mu (\nabla \cdot \mathbf{u})\mathbf{I}, \tag{2.3}$$

where $\mathbf{I}$ is the identity matrix and μ is the fluid viscosity.

In addition to the Navier-Stokes equations, the governing equation for the temperature, T, of

the mixture containing n species can be written as

$$\rho c_p \frac{\partial T}{\partial t} + \rho c_p \nabla \cdot (T\mathbf{u}) = \nabla \cdot (\rho c_p \alpha \nabla T) + \sum_i c_{p,i} \rho D_i \nabla Y_i \cdot \nabla T + \dot{\omega}_T - \dot{q}_{rad}, \tag{2.4}$$

where $\dot{\omega}_T$ includes heat source terms due to chemical reactions, α is the thermal diffusivity, D_i is the molecular diffusivity of species i, and $\dot{q}_{rad}$ encompasses all heat losses due to radiation.

Flame radiation is modeled using the RADCAL model [92]. This model relies on the assumption of optically thin medium, which is a reasonable assumption for the laboratory-scale laminar and turbulent flames considered [68, 92, 93, 94]. The radiating species considered in these flames are CO_2, H_2O, CH_4, and CO. This model uses the following expression for the rate of heat transfer per unit volume due to radiation [54, 68, 92]

$$\dot{q}_{rad} = -4\sigma \sum_i p_i a_{p_i} (T^4 - {T_\infty}^4), \tag{2.5}$$

where σ is the Stefan-Boltzmann constant, p_i is the partial pressure of species i, a_{p_i} is the Planck mean absorption coefficient of species i, and T and T_∞ are the local flame and background temperatures, respectively. The Planck mean absorption coefficients are obtained at different temperatures by running RADCAL [95], and fitted to polynomial expressions [92].

For two-feed non-premixed combustion systems (e.g. fuel and oxidizer), the flame structures are generally described by means of a passive scalar Z [16, 96, 97]. This variable is referred to as mixture fraction and ranges from 0 to 1, corresponding to pure oxidizer and pure fuel, respectively. The evolution of this variable is governed by the following transport equation

$$\frac{\partial \rho Z}{\partial t} + \nabla \cdot (\rho Z \mathbf{u}) = \nabla \cdot (\rho D \nabla Z), \tag{2.6}$$

where D is the mass diffusivity for Z. This diffusivity is set to the thermal diffusivity, α. Therefore, the Lewis number for Z

$$Le_Z = \frac{\alpha}{D} \tag{2.7}$$

is unity.

Assuming non-unity but constant Lewis number and neglecting Soret effects, the transport equation for the mass fraction of species i, Y_i, can be written as

$$\rho\frac{\partial Y_i}{\partial t} + \rho\mathbf{u}\cdot\nabla Y_i = \nabla\cdot\left(\rho\frac{\alpha}{Le_i}\nabla Y_i\right) + \nabla\cdot(\rho Y_i\mathbf{V_{c,i}}) + \dot{\omega}_i, \tag{2.8}$$

where $\dot{\omega}_i$ is the chemical source term of species i, and Le_i is the Lewis number of species i, defined as

$$Le_i = \frac{\alpha}{D_i}, \tag{2.9}$$

with D_i the mass diffusivity for species i. It was found previously that Soret effects have only minimal impact on the flame shape and temperature field [98]. The correction velocity $\mathbf{V_{c,i}}$ in Eq. 2.8 accounts for gradients in the mixture molecular weight as well as ensures zero net diffusion flux. It has the following expression

$$\mathbf{V_{c,i}} = \frac{\alpha}{Le_i}\frac{\nabla W}{W} - \alpha\left(\sum_j \frac{\nabla Y_j}{Le_j}\right) - \alpha\frac{\nabla W}{W}\left(\sum_j \frac{Y_j}{Le_j}\right), \tag{2.10}$$

where

$$W = \left(\sum_j \frac{Y_j}{W_j}\right)^{-1} \tag{2.11}$$

represents the mean molecular weight of the mixture.

The above set of equations is complemented by the equation of thermodynamic state

$$p = \rho\frac{1}{W}\widehat{R}T, \tag{2.12}$$

where $\widehat{R}$ is the universal gas constant.

2.2 Numerical solver

For full scale numerical simulations, the multi-dimensional Navier-Stokes equations and species transport equations are solved using the NGA code [90], using an iterative procedure. The NGA code, using staggered variables, allows for accurate, robust, and flexible simulations of both laminar and turbulent reactive flows in complex geometries and has been applied in a wide range of test problems, including laminar and turbulent flows, constant and variable density flows, as well as Large-Eddy Simulations (LES) and Direct Numerical Simulations (DNS). The numerical method used was developed originally for the simulation of zero Mach number flows with variable density, and have been shown to conserve discretely mass, momentum, and kinetic energy, with arbitrarily high order discretization [90]. This method is an extension of the work of Morinishi *et al.* [99]. In the simulations presented in this work, second order discretization of the viscous and convective terms of the Navier-Stokes equations is used. The semi-implicit Crank-Nicolson method is used for temporal discretization. Scalar quantities, such as the mixture fraction Z, species mass fractions Y_i, and temperature T, are transported along with the flow field using the BQUICK scheme [39]. The BQUICK scheme is a flux correction method to a well-tested numerical scheme for scalars, namely the quadratic-upwind biased interpolative convective scheme (QUICK) [100]. The BQUICK scheme ensures that the physical bounds of appropriate quantities are numerically preserved throughout the simulation without adding significant artificial diffusion. Overall, these numerical methods guarantee globally second-order accuracy in both space and time. A more detailed description of the simulation code is provided in Appendix. D.

Thermal properties for each species such as the specific heat capacity, c_{pi}, and specific enthalpy, h_i, are taken from the chemical models employed. Mixture-averaged viscosity, ν, and thermal conductivity, λ are calculated according to [101, 102], as proceeded in CHEMKIN and FlameMaster [103]. Physical properties of the flow, such as molecular diffusivities, $D_i = \frac{D}{Le_i}$, are calculated accordingly.

Chapter 3

Multi-dimensional effects in the prediction of sooting tendencies

As stricter legislation governing soot emission is being adopted, increasing attention is being paid to the characterization and quantification of soot yield. At the same time, alternative fuels such as bio-derived fuels and synthetic fuels are expected to replace progressively traditional fuels. There is a growing interest in predicting the sooting tendencies of present and future fuels based on their individual chemical compounds.

Traditionally, the sooting tendency of a given hydrocarbon species is characterized experimentally by the height of the hydrocarbon's jet flame at the smoke point [104]. The resulting smoke heights are converted to threshold sooting tendencies (TSI), which are linear functions of the inverse of the smoke point height in laminar diffusion flames. Unfortunately, while this procedure works well for small hydrocarbons, smoke heights are difficult to measure for heavily sooting species such as aromatics [93].

In an attempt to overcome these difficulties, McEnally and Pfefferle introduced a new metric for sooting tendencies, Yield Sooting Indices (YSI) [93, 105, 106]. YSI are linear functions of the maximum soot volume fraction measured on the centerline of an axisymmetric co-flow diffusion flame with the fuel stream doped with a test hydrocarbon. They argued that YSI are device-independent and only a function of the chemistry, not of the physical properties of the flow and burner used.

The most direct way to reproduce these YSI results is to perform Direct Numerical Simulations (DNS) with detailed finite-rate chemistry, by solving all the governing equations presented in the

previous chapter. These simulations have been demonstrated to be a reliable tool in reproducing axisymmetric laminar co-flow diffusion flames with various burner configurations and fuel compositions [89, 107, 108, 109]. However, the heavy computational cost associated with these simulations and the large number of hydrocarbon species under investigation make the numerical prediction of YSI using DNS impractical. The employment of reduced-order models, such as flamelet-base models, for the numerical predictions of YSI becomes a necessity. This chapter shows the importance of including multi-dimensional convection and diffusion effects in the numerical prediction of sooting tendencies when employing reduced-order models.

This work is based on a two-fold analysis. First, the importance of multi-dimensional convection and diffusion effects and the validity of the conventional flamelet model are assessed. Second, a simplified numerical framework to investigate sooting tendencies is proposed using the results from direct simulations with finite-rate chemistry. The intent of the present work is not to predict the *absolute* soot yield in flames. The emphasis is placed on the development of a computationally efficient numerical framework to predict *relative* sooting tendencies.

This chapter is organized as follows. Section 1 describes the configuration of the diffusion flame where YSI are measured experimentally and the numerical framework of direct simulations of this flame. In Section 2, the conventional flamelet model is briefly presented and shown to be incapable of predicting the correct species mass fraction profiles on the axis of the flame under study. In Section 3, a new numerical framework based on a modified flamelet equation is proposed and validated by comparison with the direct simulation results. Finally, in Section 4, numerically calculated sooting tendencies are estimated from the PAH dimer production rate, and compared to the experimentally measured YSI.

3.1 Direct numerical simulations with finite-rate chemistry

In this section, direct simulations with detailed finite-rate chemistry are conducted for an axisymmetric co-flow diffusion flame to provide reference data for comparison with the results obtained using the conventional flamelet model [49, 50].

3.1.1 Burner configuration and running conditions

The flame used in this section was studied experimentally by McEnally and Pfefferle [93] for YSI measurements. The burner consists of two concentric tubes, with fuel in the inner tube and air between the inner and outer tube. 0.4 cm of the fuel (and also air) pipe exit is simulated to allow for the fully-development of the velocity profile at the exit of the fuel pipe. Expanding the computational domain inwards the fuel pipe direction has been shown to be important to overcome a numerical error shown by Bennett *et al.* [110]. The burner configuration is depicted in Fig. 3.1, and the characteristic parameters of the burner and the inlet co-flow are listed in Table 3.1. A more detailed description of the burner configuration is given in [111]. The fuel stream velocity profile is taken to be parabolic (*i.e.* fully-developed laminar profile) based on its mean bulk velocity. On the other hand, the velocity profile in the oxidizer stream is not fully developed and is taken to be flat.

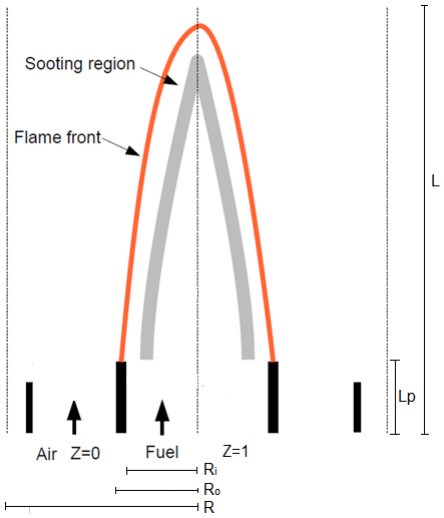

Figure 3.1: Schematic of the diffusion flame and burner configuration.

Pipe inner radius R_i	0.555 cm	Full domain radius R	5.1 cm
Pipe outer radius R_o	0.635 cm	Full domain length L	20 cm
Burner wall thickness $R_o - R_i$	0.08 cm	Pipe exit length L_p	0.4 cm
Fuel stream inlet velocity	14.39 cm/s	Oxidizer stream inlet velocity	7.03 mm/s
Fuel stream inlet temperature	425 K	Oxidizer stream inlet temperature	300 K
CH_4 mole fraction in fuel stream	0.55	O_2 mole fraction in oxidizer stream	0.21
N_2 mole fraction in Fuel	0.45	N_2 mole fraction in oxidizer stream	0.79
Dopant mole fraction in fuel stream	400ppm		

Table 3.1: Characteristic parameters for the doped co-flow diffusion flame of McEnally and Pfefferle.

In the simulation, temperatures were under-predicted when the fuel inlet temperature was taken to be $350K$ [93]. This is consistent with the fact that the burner, as well as the inlet fuel stream, are preheated by heat conduction from the flame and by absorption of heat radiated from the flame region. Unfortunately, the burner wall temperature is not specified in the experiment. Estimating it numerically is beyond the scope of the present work. Gradually increasing the fuel inlet temperature in the simulation is consistent with the intent of searching for the value of the burner exit temperature in the experiment. With a fuel inlet temperature of $425K$, the downstream temperature profiles showed better agreement with the experimental data. The fuel inlet velocity is also raised to keep the fuel inlet mass flow rate unchanged. A similar correction ($425K$ instead of $350K$) was applied in the simulation of a similar flame by Smooke *et al.* [89]. The temperature increase from $350K$ to $425K$ for fuel stream is physically reasonable, since the temperature on the centerline is measured to be $450K$ at the position closest to the burner exit (2mm from the exit plane), and an abrupt change in temperature is not expected in this small cold region.

3.1.2 Chemistry model

The detailed chemistry model employed in the current work was developed by Blanquart *et al.* [3, 33]. It contains 185 species and 1903 reactions (forward and backward reactions counted separately) and takes into account all major pathways of PAH formation. This chemical model has been extensively tested and validated in multiple configurations, including laminar premixed flames, laminar diffusion flames, and homogeneous reactors. The chemistry model is provided in the supplemental material of [23].

3.1.3 Numerical set-up

Due to the axisymmetry of the flame under consideration, the two-dimensional (2D) Navier-Stokes equations and scalar transport equations (Eqs. 2.2, 2.4, 2.6, 2.8) are solved on a 512×256 staggered mesh in cylindrical coordinate, with a total length of 20 cm and width of 5 cm, using the NGA code [90]. Non-unity but constant Lewis numbers are assumed for all species. The spatial

discretization of the computational domain is depicted in the following figure.

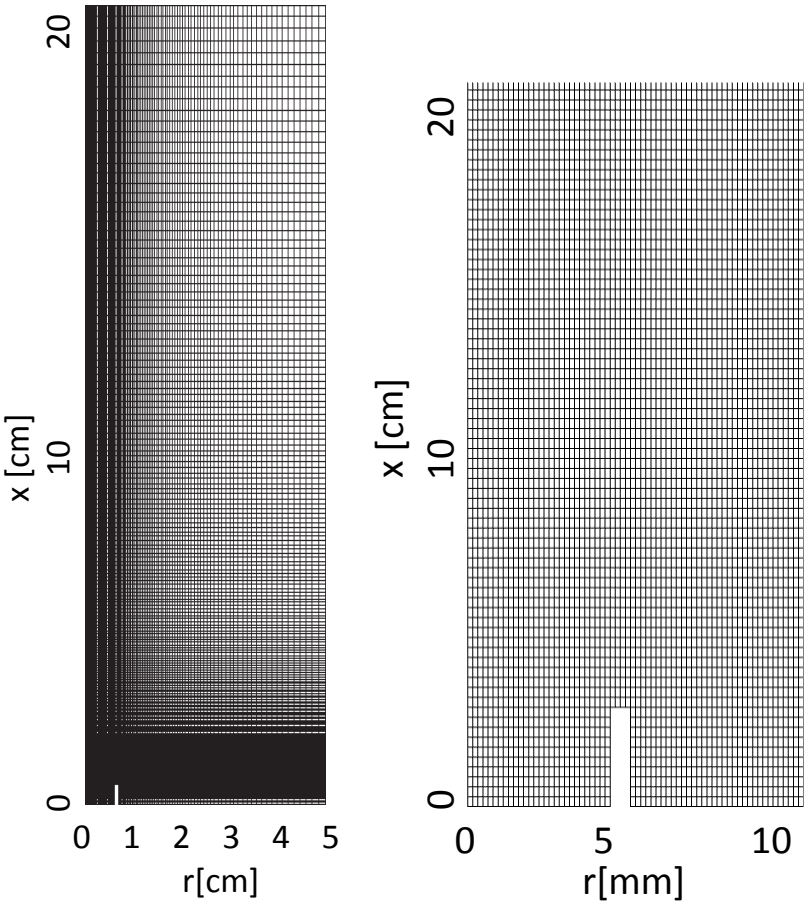

(a) Full domain. (b) Zoom in the burner region.

Figure 3.2: Axisymmetric structured mesh used for the flame simulations.

As can be seen in Fig. 3.2, the mesh is non-uniform and most refined near the region where the main chemical reactions and diffusion processes occur (around the burner exit and the flame centerline) and is stretched in both axial and radial directions away from the burner exit to reduce the computational cost. The numerical simulation is shown to give the same results when a 256×128 staggered mesh is used. This will be shown in the budget analysis detailed in Chapter. 4.3.3.

As for boundary conditions, no-slip boundary condition is imposed on the walls. The walls are also assumed to be adiabatic. At the inlet (bottom of the computational domain shown in Fig. 3.2), Dirichlet conditions are imposed for all velocity components and the scalar quantities (species mass fractions). Convective outlet boundary conditions are imposed at the outlet (top

of the computational domain shown in Fig. 3.2). The flames simulated in this thesis are co-flow diffusion flame (both laminar and turbulent). The co-flowing oxidizer streams in both the laminar flame simulated in the chapter and the turbulent flame simulated in Chapter. 6 act as a shield to protect the flame from ambient perturbations. Therefore, there is practically no flow entrainment at the sides of the computational domain (left and right boundaries of the computational domain). Accounting for this particular type of set-up, Neumann boundary conditions are imposed for scalar quantities and velocity components in the directions parallel (stream-wise and span-wise) to the sides of the computational domain. The velocity component in the cross-stream direction is set to zero on the sides, given the set-up (co-flowing oxidizer shield) of the simulated flames.

3.1.4 Results

The temperature, methane mass fraction, and acetylene mass fraction fields are depicted in Fig. 3.3, Methane and acetylene mass fractions play important roles in determining the local soot yield.

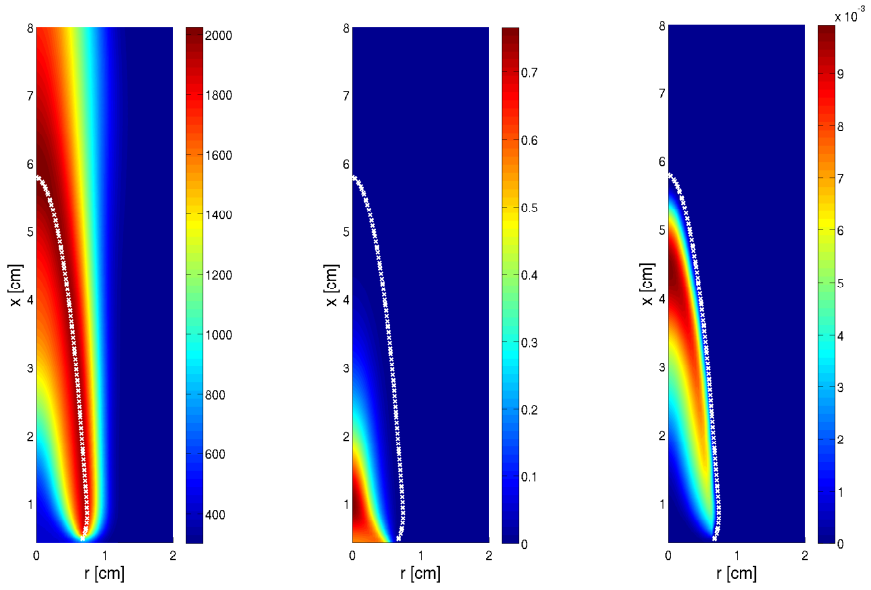

(a) Temperature. (b) Methane. (c) Acetylene.

Figure 3.3: Temperature, methane mass fraction, and acetylene mass fraction fields from the 2D direct simulation. Dashed lines indicate the location of the stoichiometric surface.

Methane mass fraction indicates the progression of the overall chemical reaction, and the acetylene

mass fraction indicates the location of PAH formation and the intensity of soot particle surface growth.

Figure 3.4 shows a comparison of the centerline temperature profile with the experimental data, and only minor differences may be observed.

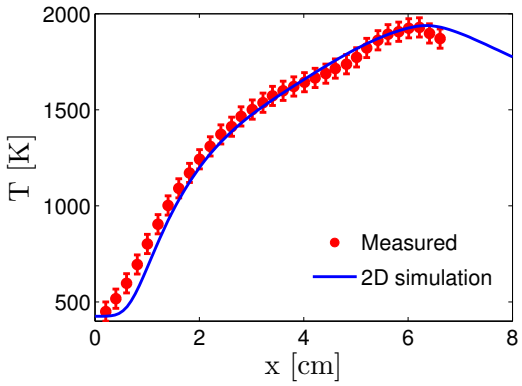

Figure 3.4: Centerline gas temperature.

First, the slope of the calculated temperature profile at the burner exit is practically zero, whereas the experimental data shows a relatively strong gradient right at the burner exit on the centerline. While a finite temperature gradient is expected at the burner wall due to heat conduction, it is unlikely that such gradient would be found at the centerline. This gradient might be related to measurement uncertainties, since it is hard to measure this small cold region inside a hot flame by using a probe with finite size (thermocouple). Second, in the highly sooting region ($z = 40 - 50$mm), the measured temperature is slightly lower than the calculated temperature. This may result from heat losses due to radiation of soot particles, which is not included in the current model. In any case, these differences remain very small and are well within the experimental uncertainties.

Unfortunately, no species measurements or other temperature measurements are provided as part of the original experimental work. Under these conditions, the quality of the numerical predictions may not be fully assessed. Nevertheless, it can be inferred that the main features of the flame on the centerline are well predicted thanks to the good agreement of the centerline temperature with experimental data. It is worth pointing out that the focus of the current study is not to carry out exact simulations on the flame considered, but to propose a methodology to predict sooting

tendencies using 2D simulation data.

3.2 Conventional laminar diffusion flamelet results

The simulation presented in the previous section is computationally expensive, since all species transport equations are solved simultaneously with the Navier-Stokes equations. Predicting YSIs using direct simulations is even more costly, since a different simulation needs to be carried out for the flame doped with each test hydrocarbon. Therefore, a computationally more efficient approach is required to compute numerically YSIs.

Based on these considerations, one natural approach to calculate numerically YSI is to use a flamelet-based model [49, 50], since the one-dimensionality of the flame structure predicted by the flamelet model can be applied to the (one-dimensional) flame centerline.

In this section, calculations using the conventional steady-state Laminar Diffusion Flamelet (LDF) model are performed on the flame centerline, using information extracted from the direct simulation presented in the previous section. The intent is to reproduce species mass fraction profiles. Consistent with the direct simulation, no soot model is included in the flamelet model.

3.2.1 Laminar diffusion flamelet equations

The LDF model was introduced originally by Peters and derived from the species transport equations (Eq. 2.8) combined with the mixture fraction transport equation (Eq. 2.6) [49, 50]. It assumes that in diffusion flames, combustion takes place essentially in a thin layer close to the flame front, defined as a flamelet. Based on a coordinate transformation, species mass fractions and temperature transport equations can be re-expressed into one-dimensional flamelet equations. The steady-state flamelet equations in the limit of unity Lewis number diffusion can be expressed as

$$-\frac{1}{2}\rho\chi\frac{\partial^2 Y_i}{\partial Z^2} = \dot{\omega}_i. \tag{3.1}$$

In the above equation, the scalar dissipation rate, χ, is defined as

$$\chi = 2D|\nabla Z|^2, \tag{3.2}$$

where D is the mass (thermal) diffusivity (Eq. 2.7). For non-unity Lewis transport, the flamelet equations become more complex and additional terms are present [112]

$$\frac{1}{4}\left(1-\frac{1}{Le_i}\right)\left(\frac{1}{\rho}\frac{\partial \rho\chi}{\partial Z}+\rho\chi\frac{c_p}{\lambda}\frac{\partial}{\partial Z}\left(\frac{\lambda}{c_p}\right)\right)\frac{\partial Y_i}{\partial Z}-\frac{1}{2Le_i}\rho\chi\frac{\partial^2 Y_i}{\partial Z^2}=\dot{\omega}_i. \tag{3.3}$$

In the above equations, the terms which accounts for gradients in the mixture molecular weight and ensures zero net diffusion flux are not shown for clarity. The reader is referred to [112] for the full version and a complete derivation of these equations for non-unity Lewis number diffusion, under flat and thin flame assumptions. The above equation is a second-order ordinary differential equation in mixture fraction space, since all variables in the above equations are only functions of mixture fraction [112]. Solving these flamelet equations is equivalent to solving a boundary value Problem.

Most existing simulations of diffusion flames with the flamelet model are based on a simplifying assumption of unity Lewis number [15, 42, 22]. While this assumption may be valid for turbulent flames [63, 113], it is questionable to apply it to laminar flames. In the simulations conducted in this work, a unity Lewis number was not assumed and a constant, non-unity Lewis number was calculated for each species. Therefore, differential diffusion effects are included. In the present work, these equations (Eq. 3.3) are solved using the FlameMaster code [103]. Details about the FlameMaster code is provided in Appendix. E.

3.2.2 Results

The flamelet equations (Eq. 3.3) presented in the previous section are solved with information obtained from the 2D simulation. Two quantities are extracted from the 2D simulation and used to solve the flamelet equations. First the scalar dissipation rate profile is obtained from the 2D

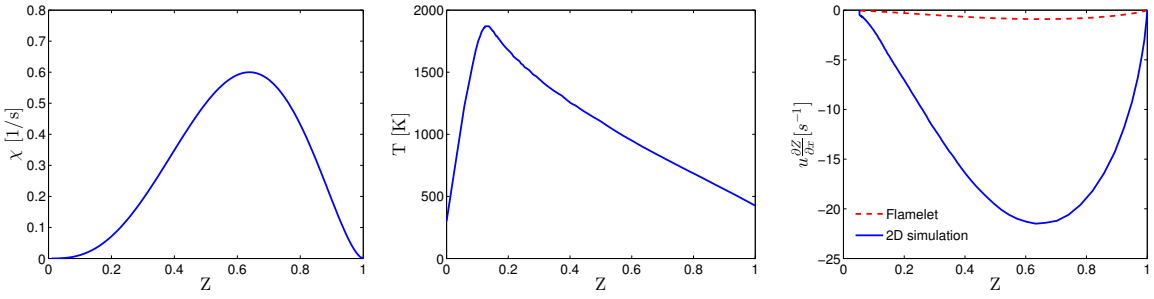

(a) Scalar dissipation rate. (b) Temperature. (c) Axial velocity $u\frac{\partial Z}{\partial x}$.

Figure 3.5: Scalar dissipation rate, temperature, and axial velocity profiles extracted from the 2D simulation along the centerline plotted in mixture fraction space.

simulation results on the centerline using the following expression

$$\chi = 2D \left| \frac{\partial Z}{\partial x} \right|^2, \tag{3.4}$$

since the derivative of Z in the radial direction vanishes thanks to axisymmetry. The extracted scalar dissipation profile is fitted and imposed in the flamelet calculations, as shown in Fig. 3.5(a). Second, the centerline temperature profile is also extracted and imposed (Fig. 3.5(b)), instead of solving the corresponding flamelet equation for temperature (Similar to Eq. 3.3). Although imposing the temperature profile is not strictly necessary, it is more consistent than solving it directly since unsteady radiation heat losses (Eq. 2.5) are not compatible with the steady-state flamelet equation [15].

The resulting mass fraction profiles for several representative species are depicted in Fig. 3.6. The locations of maximum species mass fraction are not well predicted by the flamelet model as they are on the richer side of the mixture compared to those predicted by the direct simulation. Furthermore, mass fraction profiles predicted by the flamelet model show an approximately linear decrease in mixture fraction space from the locations of maximum values on the rich side of the mixture, suggesting that diffusion is predominant compared to convection at large mixture fractions. On the contrary, results from the direct simulation indicate that species are strongly convected from the fuel inlet ($Z = 1$) towards the lean side before getting diffused.

The convective term $u\frac{\partial Y}{\partial x}$ in the species transport equation (Eq. 2.8) may be transformed into

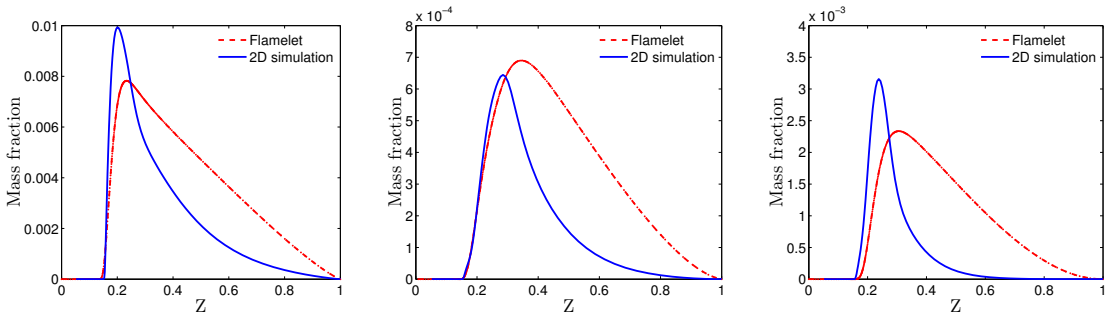

(a) C_2H_2. (b) P-C_3H_4. (c) C_6H_6.

Figure 3.6: Comparison of species mass fraction in mixture fraction space between the DNS and the conventional flamelet model.

a convective term in mixture fraction, $\left(u\frac{\partial Z}{\partial x}\right)\frac{\partial Y}{\partial Z}$, with convection velocity $u\frac{\partial Z}{\partial x}$. Using the balance between convection and diffusion in the mixture fraction transport equation, this term is computed as

$$u\frac{\partial Z}{\partial x} = \frac{1}{4}\left(\frac{1}{\rho}\frac{\partial \rho\chi}{\partial Z} + \rho\chi\frac{c_p}{\lambda}\frac{\partial}{\partial Z}\left(\frac{\lambda}{c_p}\right)\right), \tag{3.5}$$

in the conventional flamelet model [112] (Eq. 3.3). As will be shown in the next section, this expression underestimates significantly the actual convective effect (Fig. 3.5(c)). These discrepancies demonstrate that the flamelet model fails to capture the correct dominant physical processes for mixture fractions beyond the stoichiometric value. These rich conditions are of critical importance for the formation of Polycyclic Aromatic Hydrocarbons (PAH). Hence, a new numerical framework is required to reproduce the correct physics along the centerline, where thin flamelet hypothesis may not be valid.

3.3 Derivation of modified flamelet equations

Taking into account multi-dimensional convection and diffusion effects, a modified flamelet model is now proposed and shown to be able to reproduce species mass fractions reasonably accurately on the flame centerline. In this section, the modified flamelet equations are not derived for the purpose of chemistry tabulation. Instead, they are derived as continuous governing equations for species transport on the flame centerline, treating the centerline as a single one-dimensional flamelet. This

is due to the fact that YSI are defined as functions of the maximum soot volume fraction on the centerline. Consequently, it is sufficient to derive and solve diffusion flamelet equations that are only valid on the centerline. Further, modeling the flame centerline as a single flamelet is feasible since the value of the mixture fraction variable goes from one at the fuel burner surface, to practically zero at elevated flame heights above the burner exit plane. Modified flamelet equations are derived from the continuity equation (Eq. 2.1) and the species transport equations (Eq. 2.8).

3.3.1 Preliminary considerations

Under thin flame assumptions, the conventional flamelet model [112] assumes that all variables are only functions of the mixture fraction. It is further assumed that all derivatives along the flame front are negligible when compared to derivatives across the flame [49, 50]. This may not be valid for a co-flow diffusion flame *along the centerline*, where the characteristic length scale in the radial direction (across the flame) is not negligible compared to the axial length scale (along the flame). Based on the above concern, mapping all physical variables only in the one-dimensional mixture fraction space might not be sufficient to capture multi-dimensional convection and diffusion effects.

3.3.2 New mapping

A new mapping parameter ϕ, whose gradient lies in the local iso-surface of mixture fraction is introduced, with

$$\nabla Z\left(x,r\right)\cdot\nabla\phi\left(x,r\right)=0. \tag{3.6}$$

With this new variable, a coordinate change is performed between the cylindrical variables (r,x) and the phase space variables (Z,ϕ). Consequently, derivatives in physical space can be expressed as

$$\frac{\partial}{\partial x}=\frac{\partial Z}{\partial x}\frac{\partial}{\partial Z}+\frac{\partial\phi}{\partial x}\frac{\partial}{\partial\phi}, \tag{3.7}$$

$$\frac{\partial}{\partial r}=\frac{\partial Z}{\partial r}\frac{\partial}{\partial Z}+\frac{\partial\phi}{\partial r}\frac{\partial}{\partial\phi}. \tag{3.8}$$

According to axisymmetry, the boundary conditions on the centerline are

$$v|_{r=0} = 0, \frac{\partial Z}{\partial r}|_{r=0} = 0, \frac{\partial Y_i}{\partial r}|_{r=0} = 0, \tag{3.9}$$

where v is the velocity component in the radial direction. To ensure orthogonality between the gradient of Z and ϕ, the latter must satisfy

$$\frac{\partial \phi}{\partial x}|_{r=0} = 0 \tag{3.10}$$

on the centerline. In other words, ϕ is constant along the centerline. It will be assume to be zero without loss of generality. The equations listed above lead to the following modified flamelet equation

$$\left(1 - \frac{1}{Le_i}\right) u \frac{\partial Z}{\partial x} \frac{\partial Y_i}{\partial Z} = \frac{1}{2} \frac{\chi}{Le_i} \frac{\partial^2 Y_i}{\partial Z^2} + \frac{1}{2} \frac{\xi}{Le_i} \frac{\partial^2 Y_i}{\partial \phi^2} + \frac{\dot{\omega}_i}{\rho}, \tag{3.11}$$

where

$$\xi = 2D|\nabla \phi|^2, \tag{3.12}$$

and u is the velocity component in the axial direction along the centerline. The terms corresponding to molar diffusion, mass correction diffusion, and molar correction diffusion are included in the derivation, but not shown in the above equation for clarity.

In the above equation, the species mass fractions are functions of the two phase space variables Z and ϕ, $Y_i(Z, \phi)$. The dissipation rates of Z (*i.e.* χ) and ϕ (*i.e.* ξ) are evaluated from the 2D simulation results in physical space (along the centerline) and then mapped on to mixture fraction space. The same is done for $u\frac{\partial Z}{\partial x}$.

3.3.3 Effects of the different terms

The modified flamelet equation represents the balance between convection, diffusion, and chemistry in mixture fraction space, with a convective velocity given by (Fig. 3.5(c))

$$u_z = u\frac{\partial Z}{\partial x}. \tag{3.13}$$

This convective velocity is in phase space (mixture fraction space), not in physical space. Therefore, the unit of u_z is not m/s but $1/s$, since the mixture fraction variable does not have any dimension. It is interesting to note that the convective term in the mixture fraction space disappears if the Lewis number is unity. This underlines the importance of differential diffusion effects for this particular flame. It also shows that heavier species (such as PAH) will be more affected by non-unity Lewis number effects.

The mass diffusion term $\frac{1}{2}\frac{\chi}{Le_i}\frac{\partial^2 Y_i}{\partial Z^2}$ appears in both the conventional and modified flamelet equations, representing diffusion in the direction orthogonal to the local iso-surface of mixture fraction. The additional mass diffusion term $\frac{1}{2}\frac{\xi}{Le_i}\frac{\partial^2 Y_i}{\partial \phi^2}$ in Eq. 3.11 represents diffusion in the direction parallel to the local iso-surface of mixture fraction, which is neglected by the conventional flamelet model. This term is able to redistribute the species in a way that is depicted in Fig. 3.7.

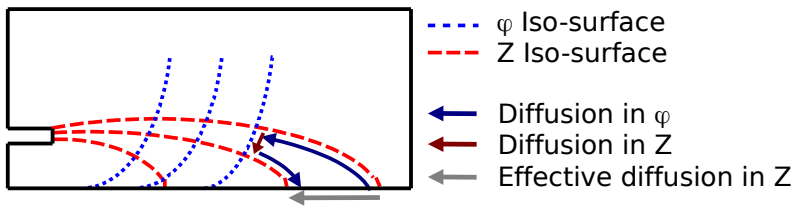

Figure 3.7: Schematic of the diffusion process. The dashed lines represent the mixture fraction iso-contours, and the dash-dot lines represent ϕ iso-contours.

3.3.4 Closure of the modified flamelet equations

Unfortunately, some of the terms in the new flamelet equations (Eq. 3.11) can not be expressed solely as a function of mixture fraction, as is the case of the conventional flamelet equations (Eqs. 3.1

and 3.2). In other words, the modified flamelet equations (Eq. 3.11) are not closed in mixture fraction space, as the parameter ϕ is independent of the mixture fraction (Eq. 3.6).

In the current work, in order not to obviate the distinct advantage offered by the flamelet model, both diffusion terms in Z and ϕ are combined into one single term by introducing a new parameter χ' as the aggregate scalar dissipation rate. Mathematically, this means

$$\frac{1}{2}\frac{\chi}{Le_i}\frac{\partial^2 Y_i}{\partial Z^2} + \frac{1}{2}\frac{\xi}{Le_i}\frac{\partial^2 Y_i}{\partial \phi^2} = \frac{1}{2}\frac{\chi'}{Le_i}\frac{\partial^2 Y_i}{\partial Z^2}. \tag{3.14}$$

Obviously, the above equation is not valid everywhere in the domain, and it is valid and considered only on the flame centerline. Physically, this treatment is equivalent to representing the diffusion path directed by the arrows outside the flame axis by the diffusion arrow on the flame axis, as shown in Fig. 3.7. This yields the resulting balance equation

$$\left[\left(1 - \frac{1}{Le_i}\right) u_z\right] \frac{\partial Y_i}{\partial Z} = \frac{1}{2}\frac{\chi'}{Le_i}\frac{\partial^2 Y_i}{\partial Z^2} + \frac{\dot{\omega}_i}{\rho}. \tag{3.15}$$

As mentioned previously, additional terms accounting for molar/mass diffusion and ensuring zero net diffusion fluxes are not shown in the above equation. The complete modified flamelet equations being solved are included in Appendix. A.

Written in this form (Eq. 3.15), the modified flamelet equations are in the form of Ordinary Differential Equations (ODE) in mixture fraction space, since the quantities u_z (Eq. 3.13) and χ' can be expressed as functions of mixture fraction.

As mentioned earlier, these two quantities are extracted on the flame centerline from the detailed simulation with finite-rate chemistry, and are tabulated as a function of mixture fraction

$$u_z = u_z(Z), \tag{3.16}$$

$$\chi' = \chi'(Z). \tag{3.17}$$

We are able to do so since there is a unique inversion between the axial coordinate, x, and mixture

fraction on the centerline, as mixture fraction is a strictly decreasing function of x. Furthermore, ϕ is identically zero along the centerline.

Equations 3.15 and 3.17 lead to the following system of second order ODEs in mixture fraction space

$$\left[\left(1-\frac{1}{Le_i}\right)u_z\left(Z\right)\right]\frac{\partial Y_i}{\partial Z}=\frac{1}{2}\frac{\chi'\left(Z\right)}{Le_i}\frac{\partial^2 Y_i}{\partial Z^2}+\frac{\dot{\omega}_i}{\rho}. \tag{3.18}$$

These ODEs can be solved as two-point boundary value problems of the unknown species mass fractions, $Y_i(Z,\chi)$.

3.3.5 Determination of the aggregate scalar dissipation rate

The aggregate scalar dissipation rate, as defined in Eq. 3.14, is actually not universal as for conventional flamelet equations, but it is defined species-wise. In other words, there exits one χ' for each species. Figure 3.8 shows the aggregate scalar dissipation profiles for several representative species in mixture fraction space. These profiles are evaluated as

$$\chi_i'=-2Le_i\left(\left[\left(1-\frac{1}{Le_i}\right)u_z\right]\frac{\partial Y_i}{\partial Z}+\frac{\dot{\omega}_i}{\rho}\right)/\left(\frac{\partial^2 Y_i}{\partial Z^2}\right) \tag{3.19}$$

for species i, which is equivalent to Eq. 3.15.

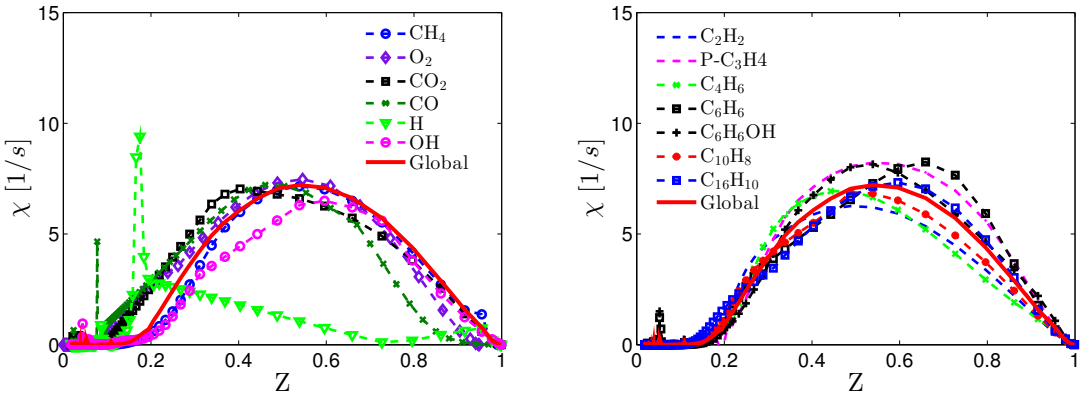

(a) Main species and radicals.

(b) Soot precursors.

Figure 3.8: Aggregate scalar dissipation rates for species of interest and the global fitted one.

As seen in Fig. 3.8, with the exception of a few species, these curves appear to collapse onto a

single profile. A least squares method is used point-wise in mixture fraction space to obtain a global χ' (red solid line). More precisely, at each location, Z_j, in mixture fraction space, the value of χ' is determined as the one that minimize the following quantity

$$\sum_i \left(\chi'(Z_j) - \chi'_i(Z_j)\right)^2 . \tag{3.20}$$

The obtained global scalar dissipation rate, χ', is used as an input to solve the modified flamelet equations (Eq. 3.15).

For most of the species, the deviation between the species specific dissipation rate, χ'_i, and the global dissipation rate, χ', is within 20%. The largest deviation is observed for hydrogen radical. This is not surprising since the residence time of H is extremely small compared to the characteristic transport time scale. Hence, the yield of H is controlled predominantly by a balance between chemical production and consumption (and not diffusion). Consequently, the large deviation observed would not affect the modified flamelet results. Finally, it is important to note that the global, χ', aggregate dissipation rate has a different shape and is about an order of magnitude larger than the original dissipation rate, χ, given by Eq. 3.2 (Fig. 3.5 (a)).

It is important to note the definition of the aggregate scalar dissipation (Eq. 3.19) is derived from the balance equation (Eq. 3.15), but not from the complete modified flamelet equations shown in Appendix. A. However, only a negligible amount of error is introduced by this definition since the magnitudes of all other terms in the complete flamelet equation that are not shown in Eq. 3.15 are negligible compared to that of the terms included. This point will be illustrated later in the budget analysis (Figs. 4.12 and 4.13) in Chapter 4, where these terms are grouped together and referred to as correction terms; and the magnitude of these correction terms is shown to be significantly smaller than that of the dominating terms, namely those being included in Eq. 3.15.

3.3.6 Simulation procedure

In practice, one additional quantity, namely the flame temperature, needs to be extracted from

the detailed simulation with finite-rate chemistry and tabulated as a function of mixture fraction, to close the modified flamelet equations (Eq. 3.18). The overall procedure for the extraction and tabulation of these quantities is described below.

- First, centerline temperature is extracted, and tabulated as a function of mixture fraction (Fiq. 3.5(b)), and imposed.
- Second, the quantity $u_z = u\frac{\partial Z}{\partial x}$ along the centerline is extracted from the detailed simulation (Fiq. 3.5(c)).
- Third, the global aggregate scalar dissipation rate profile, χ' (red solid line in Fig. 3.8), is tabulated as a function of the mixture fraction.
- Finally, the flamelet equations (Eq. 3.15) are solved with the imposed χ', u_z, and temperature profiles.

3.3.7 Validation

The modified flamelet model is applied to the flame mentioned in Chapter. 3.1, using the global fitted curve for χ'. Resulting species mass fraction profiles are compared against the direct simulation results on the centerline of the flame, in mixture fraction space for a few of the species (Fig. 3.9). Solutions of the modified flamelet equations show reasonably good agreement with the direct simulation results, and remarkable improvements with respect to the results from the conventional flamelets (Fig. 3.6). The multi-dimensional effects are taken into account and mapped onto the one-dimensional mixture fraction space where modified flamelet equations (Eq. A.1) are solved.

It is interesting to note that only the global aggregate scalar dissipation rate is required to reproduce the correct mass fraction profiles for species of a wide range of molecular weight and Lewis numbers. The strong convection effects on the rich side of the mixture are well captured. The discrepancies are primarily for the reason that the global aggregate scalar dissipation rate cannot represent exactly the specific ones for each species. To further improve the mass fraction prediction

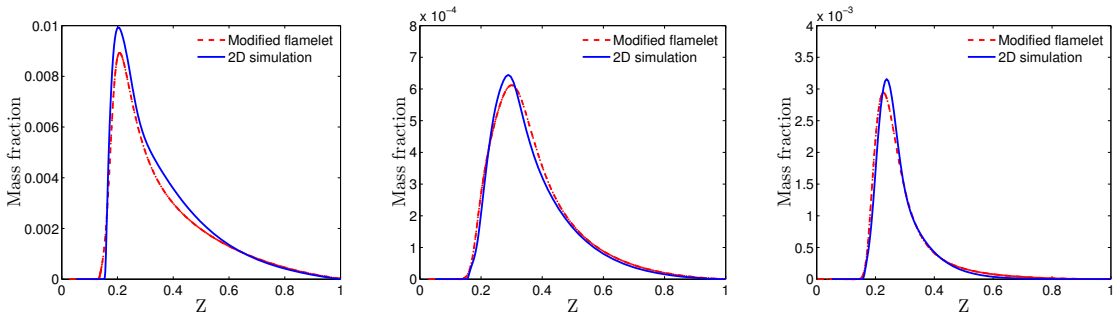

(a) C_2H_2 (b) P-C_3H_4 (c) C_6H_6

Figure 3.9: Comparison of species mass fractions from modified flamelet calculations with results from the 2D simulation.

of different species on the centerline, the species specific aggregate scalar dissipation rates, χ_i', could be extracted from the 2D direct simulation results using Eq. 3.19. However, the proposed method using the global aggregate scalar dissipation rate, χ', is advantageous, since once χ' is obtained, it can be used for modified flamelet calculations with any other chemical mechanisms that contain species not included in the current one.

3.4 Sooting tendency analysis

After validating the new numerical framework, the current flamelet model is applied to reproduce the YSI measurements of McEnally and Pfefferle [93, 105, 106]. YSI are estimated from the PAH dimer production rate given by the flamelet calculations.

3.4.1 Doped flame versus undoped flame

In the experiments, the YSI of various hydrocarbons were determined by measuring the maximum soot volume fraction along the axis of the flame with the fuel stream doped with 400 ppm of a test species [93]. McEnally and Pfefferle found that the addition of small amount of dopant species did not change the temperature profile noticeably; only the soot yields were affected [93].

To mimic the experimental approach in the direct numerical simulations, the boundary conditions for the fuel inlet ($Z = 1$) are changed accordingly, to include the dopant species ($X_{dopant} = 400ppm$). The modified flamelet equations (Eq. A.1) are solved using the same temperature, velocity, and

dissipation rate profiles as for the undoped flame (Figs. 3.5 and 3.8).

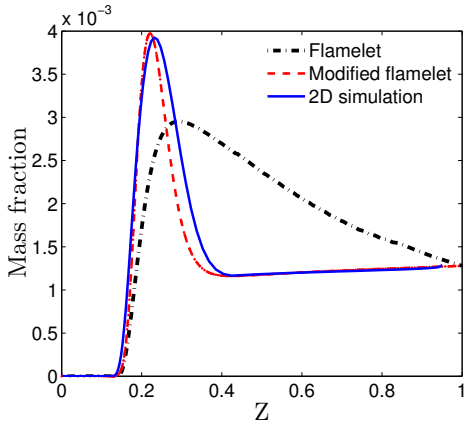

Figure 3.10: Dopant (C_6H_6) mass fraction profiles on the centerline of flames with dopant calculated using conventional and modified flamelet models.

The modified flamelet model results show reasonably good agreement with direct simulation results for the dopant species, C_6H_6, as shown in (Fig. 3.10). The added dopant is convected to the flame front, where it will contribute to the soot yield, whereas the conventional flamelet predicts the dopant to be strongly diffused before reaching the flame front, and would contribute only marginally to the soot yield.

3.4.2 Sooting yield versus PAH dimer production rate

To ensure that the current work is not biased by the soot model that one may choose, maximum soot volume fraction is estimated to be essentially proportional to the PAH dimer production rate based on the following considerations.

Without loss of generality, the soot volume fraction, f_v, is governed by the transport equation (Eq. 3.21),

$$\frac{\partial \rho f_v}{\partial t} + \nabla \cdot (\rho f_v \mathbf{u}) = \dot{\omega}_{f_v}, \tag{3.21}$$

where the source term, $\dot{\omega}_{f_v}$, in this equation includes all contributions from nucleation, condensation, coagulation, surface growth, and oxidation. Soot particles are formed through the process of nucleation. Their inception is commonly assumed to occur when heavy PAH molecules collide with each other, and is characterized in this work by the PAH dimer production rate calculated according

to [114, 115, 116]. In other words, the soot nucleation rate is a linear function of the PAH dimer production rate. Soot particles further grow through condensation, coagulation, and by surface mass addition following a C_2H_2-based addition mechanism. Condensation describes the process of PAH molecules colliding with and sticking to soot particles. In fact, the fate of large PAH molecules is only twofold: collide with each other to form soot (nucleation), or collide with a soot particle (condensation). In other words, given a certain PAH mass production rate, the total mass production of soot is determined. Therefore, the condensation process changes the number density function of soot, but does not affect the soot volume fraction directly. Soot surface growth rate is controlled by the amount of C_2H_2, the temperature, and the total soot surface area, which is proportional to the total soot volume fraction. Oxidation of soot particles is commonly assumed to occur by reaction with OH radicals. The oxidation source term is consequently a function of the total soot surface area, the temperature, and OH radicals concentration.

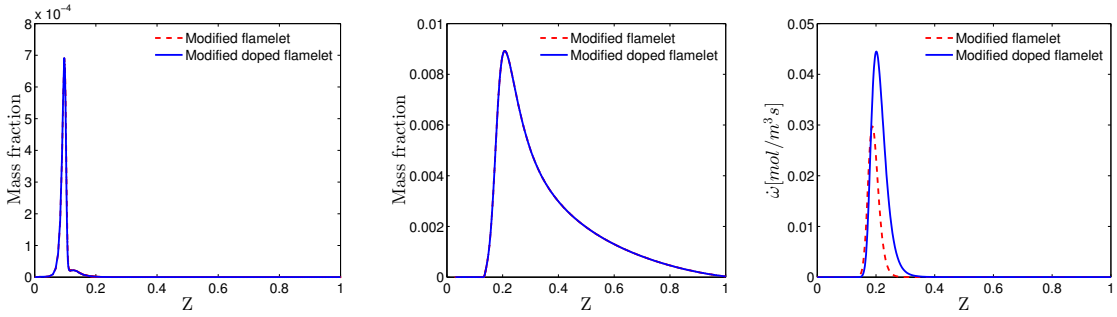

(a) OH. (b) C_2H_2. (c) $\dot{\omega}_{Nucl}$.

Figure 3.11: Comparison between the flame with and without dopant (C_6H_6) for OH radical, C_2H_2, and PAH dimer production rate.

Figure 3.11 compares the C_2H_2 mass fraction, OH mass fraction, and the nucleation source term, $\dot{\omega}_{nucl}$, profiles in mixture fraction space from the flamelet solutions with and without adding a dopant (C_6H_6). It is shown that OH and C_2H_2 mass fraction profiles on the centerline are not changed when a dopant is added (consistently with experimental observation). This observation indicates that the contributions to soot source term due to surface growth and oxidation are unchanged when a dopant is added. On the other hand, the PAH dimer production rate (nucleation source term) is increased by the presence of a dopant species. As a consequence, one can estimate the increment of

the maximum soot volume fraction on the centerline from the increment of PAH dimer production rate when the flame is doped.

3.4.3 Numerical YSI

The amount of soot particles produced by the gas-phase chemistry can be calculated by integrating the transport equation of soot mass fraction in mixture fraction space

$$Y_{sootmax} = max\left(\int_0^z \frac{\dot{\omega}_{Nucl}}{\rho u_z} dZ\right). \tag{3.22}$$

The above equation does not include any oxidation terms, as the intent is to evaluate the maximum soot yield the chemistry alone could produce. This equation is equivalent to the following flamelet equation

$$\rho u_z \frac{\partial Y_{soot}}{\partial Z} = \dot{\omega}_{soot} \tag{3.23}$$

which can be obtained by taking the limit of Eq. 3.15 when Le_{soot} tends to infinity.

Following the same methodology as in the experimental work, a numerical Yield Sooting Index, YSI_{num}, can be defined as

$$YSI_{num} = A \cdot Y_{sootmax} + B, \tag{3.24}$$

where A and B are constant parameters chosen so that YSI_{num}-Benzene = 30 and YSI_{num}-1-Ethylnaphthalene = 151. Practically, the reference values for numerical YSI could be set arbitrarily by any other species. However, given the complexity of the chemical kinetics for aromatic species, the two reference values are set for species that are believed to be well predicted by the current chemistry mechanism.

Numerical YSI for different species are reported in Table 3.2, and compared to the corresponding experimental values [93, 105, 106]. The species are selected based on their presence in the kinetic mechanism used in the present work, and were studied experimentally. The calculated YSI are plotted in Fig. 3.12 as a function of the experimentally measured YSI for both non-aromatic and

Name	Formula	YSI_{exp}	YSI_{num}
[Combust. Flame 148 (2007) p210]			
Benzene	C_6H_6	30	30*
Methylbenzene	C_7H_8	43.5	52.9
Ethynylbenzene	C_8H_6	52.6	54.3
Ethenylbenzene	C_8H_8	44.1	53.7
Ethylbenzene	C_8H_{10}	53.6	65
Indene	C_9H_8	100.3	89.9
[Proc. Comb. Inst. 32 (2009) p673]			
2-Heptanone	$C_7H_{14}O$	17	7.8
1-Methylnaphthalene	$C_{11}H_{10}$	135	114.5
1-Ethylnaphthalene	$C_{12}H_{12}$	151	151*
2-Ethylnaphthalene	$C_{12}H_{12}$	145	172
[Env. Sci. Technol. 45 (2011) p2498]			
Linear 2-octanone	$C_8H_{16}O$	18.3	15
Trimethylpentane	C_8H_{18}	22.6	20.4

Table 3.2: Experimental and numerical sooting tendencies of different species. * Computational YSI scaled to have the same values as the experimental YSI.

aromatic species.

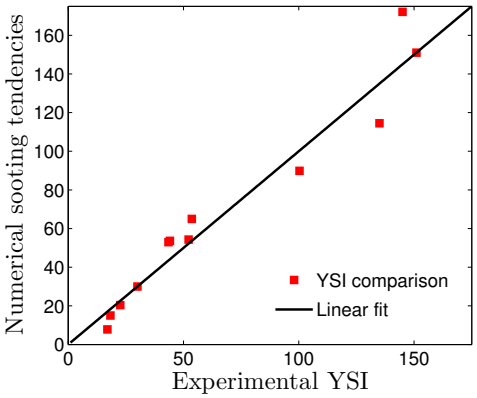

Figure 3.12: Linear relation between the measured YSI in the literature and the numerically computed YSI.

3.4.4 Discussion

The computed YSI show very good agreement with the experimentally measured YSI for a wide range of test species. This highlights not only the validity of the proposed flamelet-based modeling approach, but also the quality of the chemical model employed. Nevertheless, some discrepancies are observed for certain large aromatic species ($C_{12}H_{10}$ and $C_{12}H_{12}$), which are not surprising given

the limited knowledge on their formation pathways. This numerical framework can be used in the future to identify deficiencies in the chemical model and ultimately improve the overall soot modeling approach.

The current model is computationally efficient since only one flamelet calculation with a dopant species is needed to compute the YSI of that species. More generally, the approach proposed by this work suggests that only one direct simulation per flame is necessary to compute numerically YSIs defined on that particular flame with the corresponding burner configuration and fuel composition. Such direct simulation could be done using a reduced chemical mechanism even without aromatic chemistry since only the convective velocity, temperature, and aggregate scalar dissipation rate profiles need to be extracted along the flame axis. Based on these data, YSI of the test species can be deduced by solving the modified flamelet equations once per dopant. Alternatively, it is possible to perform direct simulations of doped flames for each dopant species as for the benzene-doped flame in the previous subsection. However, the large amount of computational time (around 20 days) that a doped flame takes to reach its steady-state makes the proposed flamelet-based modeling approach for YSI prediction more preferable.

Despite the various advantages offered by the proposed modified flamelet formulation, there are still several issues that need to be addressed. First, the convective velocity u_z (Eq. 3.13) used for modified flamelet calculations is extracted from the 2D direct simulation, since the difference between the convective velocities predicted by the conventional flamelet model and the 2D direct simulation (Fig. 3.5(c)) has not been understood physically. Second, tangential diffusion has been shown to be more important than diffusion in mixture fraction. However, the physical mechanism behind such strong multi-dimensional diffusion effects has not been well understood. Finally, the proposed modified flamelet model is only valid on the flame centerline. To overcome all these limitations, a more general mathematical framework is required to describe correctly the flame structure of laminar diffusion flames.

Chapter 4

Modeling curvature effects in diffusion flames using a laminar flamelet model

This chapter intents to address the issues pointed out at the end of the previous chapter. The intent of this chapter is to go beyond the modified flamelet equations derived on the flame centerline, and to propose a generalized flamelet equation valid everywhere in non-premixed reacting mixtures to predict local flame structures for chemistry tabulation. The objectives of this work are three-fold:

1) derive a consistent mathematical formulation of the one-dimensional *curved flamelet* with differential diffusion;

2) model the scalar dissipation rate and curvature dependences on mixture fraction for proper integration in the curved flamelet equations;

3) apply this derived model and investigate the effects of flame curvature and non-unity Lewis numbers in a multi-dimensional configuration.

The current work focuses on laminar flames, but the same results would be applicable to low Reynolds number turbulent flames in which differential diffusion effects are potentially important.

The chapter is organized as follows. A new flamelet formulation including curvature effects is derived in Section 1 using a general coordinate transformation. In Section 2, two basic configurations that represent curved flamelets in turbulent combustion are studied to investigate the functional dependence of scalar dissipation rate and curvature on mixture fraction. The proposed flamelet

equations are solved at various curvature values, and the results are compared to those of a planar flamelet under the same conditions. In Section 3, the importance of curvature is highlighted, and its effects are investigated based on the full chemistry simulation results for a laminar co-flow diffusion flame. Finally, a summary of curvature effects under various configurations is provided in Section 4.

4.1 Derivation of the flamelet equations with curvature

In this section, the full flamelet equations are re-derived using a general coordinate transformation to better identify the curvature and tangential terms.

4.1.1 Conventional laminar diffusiton flamelet model

The conventional Laminar Diffusion Flamelet (LDF) equations were derived originally by Peters [49, 50] starting from the species transport equations combined with the mixture fraction transport equation (Eqs. 2.6 and 2.8). The following coordinate transformation was used

$$x_1 \rightarrow Z, x_2 = Z_2, x_3 = Z_3, t = \tau, \tag{4.1}$$

leading to the conversion of the Cartesian coordinates (x_1, x_2, x_3) into a flame-attached frame of reference (Z, Z_2, Z_3), where Z indicates the mixture fraction as introduced in Eq. 2.6.

In the original work by Peters [50], Z_2 and Z_3 are chosen to be the same as distance functions in the x_2 and x_3 directions of the original Cartesian coordinate system. By construction, these two directions (Z_2 and Z_3) are not perpendicular to the gradient of mixture fraction (they do not need to be). Therefore, they do not lie within the surface of constant mixture fraction, as shown in the schematic representation in Peters' original work (Fig. 1 in [50]). In the limit of a thin, one-dimensional flat flame, this coordinate system is appropriate and convenient to derive the LDF equations. However, for either a thick flame or a curved flame, a coordinate system with Z_2 and Z_3 perpendicular to Z would be more appropriate to distinguish effects due to tangential

diffusion/convection and those due to flame curvature.

4.1.2 Generalized flamelet coordinate transformation

To derive the curved flamelet equations, a more general coordinate transformation is considered:

$$(x_1, x_2, x_3, t) \rightarrow (Z(x_1, x_2, x_3, t), Z_2(x_1, x_2, x_3, t), Z_3(x_1, x_2, x_3, t), \tau)\,. \tag{4.2}$$

This coordinate transformation is depicted in Fig. 4.1 for a two-dimensional configuration. The

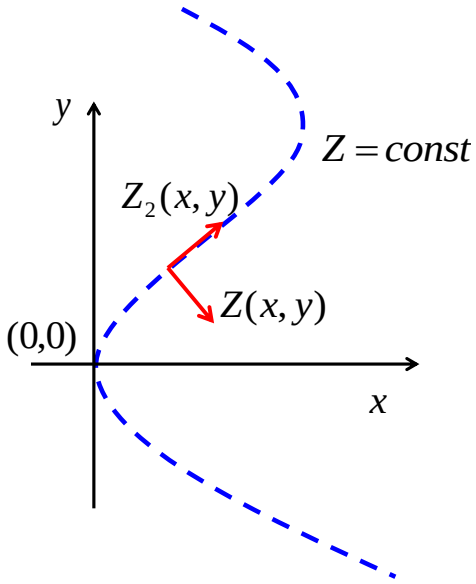

Figure 4.1: Schematic of the coordinate transformation.

coordinates Z_2 and Z_3 are chosen such that

$$\nabla Z \cdot \nabla Z_2 = 0, \text{ and } \nabla Z \cdot \nabla Z_3 = 0 \tag{4.3}$$

at *every* grid point in the domain, where the operator ∇ is the gradient operator in physical space. This ensures that Z_2 and Z_3 lie *within* the iso-surface of mixture fraction Z. In other words, Z_2 and Z_3 are curvilinear coordinates. It is important to note that Z_2 and Z_3 do not have to be distance functions. For instance, for spherical flames, defining $Z_2 = \theta$ and $Z_3 = \phi$ could be an appropriate

choice. Furthermore, ∇Z_2 and ∇Z_3 are not necessarily orthogonal to each other. The proposed coordinate transformation leads to the following transformation rules

$$\begin{aligned}
\frac{\partial}{\partial t} &= \frac{\partial Z}{\partial t}\frac{\partial}{\partial Z} + \frac{\partial Z_2}{\partial t}\frac{\partial}{\partial Z_2} + \frac{\partial Z_3}{\partial t}\frac{\partial}{\partial Z_3} + \frac{\partial Z}{\partial \tau}, \\
\frac{\partial}{\partial x_1} &= \frac{\partial Z}{\partial x_1}\frac{\partial}{\partial Z} + \frac{\partial Z_2}{\partial x_1}\frac{\partial}{\partial Z_2} + \frac{\partial Z_3}{\partial x_1}\frac{\partial}{\partial Z_3}, \\
\frac{\partial}{\partial x_2} &= \frac{\partial Z}{\partial x_2}\frac{\partial}{\partial Z} + \frac{\partial Z_2}{\partial x_2}\frac{\partial}{\partial Z_2} + \frac{\partial Z_3}{\partial x_2}\frac{\partial}{\partial Z_3}, \\
\frac{\partial}{\partial x_3} &= \frac{\partial Z}{\partial x_3}\frac{\partial}{\partial Z} + \frac{\partial Z_2}{\partial x_3}\frac{\partial}{\partial Z_2} + \frac{\partial Z_3}{\partial x_3}\frac{\partial}{\partial Z_3}.
\end{aligned} \tag{4.4}$$

Using the above relations, the gradient of a scalar s can be expressed as

$$\nabla s = \frac{\partial s}{\partial Z}\nabla Z + \frac{\partial s}{\partial Z_2}\nabla Z_2 + \frac{\partial s}{\partial Z_3}\nabla Z_3. \tag{4.5}$$

Additionally, the divergence of a vector $\mathbf{v}$ can be expressed as

$$\nabla \cdot \mathbf{v} = \frac{\partial \mathbf{v}}{\partial Z}\cdot\nabla Z + \frac{\partial \mathbf{v}}{\partial Z_2}\cdot\nabla Z_2 + \frac{\partial \mathbf{v}}{\partial Z_3}\cdot\nabla Z_3. \tag{4.6}$$

Finally, the Laplacian of a scalar s can be expressed as

$$\begin{aligned}
\nabla\cdot(\nabla s) \quad = \quad & \frac{\partial^2 s}{\partial Z^2}|\nabla Z|^2 + \frac{\partial^2 s}{\partial Z_2^2}|\nabla Z_2|^2 + \frac{\partial^2 s}{\partial Z_3^2}|\nabla Z_3|^2 + 2\frac{\partial^2 s}{\partial Z_2 \partial Z_3}(\nabla Z_2 \cdot \nabla Z_3) \\
& + \frac{\partial s}{\partial Z}\nabla^2 Z + \frac{\partial s}{\partial Z_2}\nabla^2 Z_2 + \frac{\partial s}{\partial Z_3}\nabla^2 Z_3
\end{aligned} \tag{4.7}$$

4.1.3 Flamelet equations with curvature effects

Starting from the species transport equations (Eq. 2.8) and using the differential operators (Eqs. 4.5, 4.6 and 4.7), as well as the transport equation of mixture fraction (Eq. 2.6), the full flamelet equations

can be derived as

$$
\begin{aligned}
& \rho\frac{\partial Y_i}{\partial \tau} + \underbrace{\rho\sum_{k=2}^{3}\left[\frac{\partial Y_i}{\partial Z_k}\left(\frac{\partial Z_k}{\partial t} + \mathbf{u}\cdot\nabla Z_k\right)\right]}_{\text{Lagrangian transport } L_t} \\
& + \underbrace{\left(1-\frac{1}{Le_i}\right)\nabla\cdot(\rho D\nabla Z)\frac{\partial Y_i}{\partial Z}}_{\text{Convection in mixture fraction } C_Z} \\
= \; & + \underbrace{\frac{\rho\chi}{2Le_i}\frac{\partial^2 Y_i}{\partial Z^2}}_{\text{Normal diffusion } D_Z} + \dot{\omega}_i \\
& + \underbrace{\sum_{k=2}^{3}\frac{\rho\chi_k}{2Le_i}\frac{\partial^2 Y_i}{\partial Z_k^2} + \frac{2\rho D}{Le_i}(\nabla Z_2\cdot\nabla Z_3)\frac{\partial^2 Y_i}{\partial Z_2\partial Z_3}}_{\text{Tangential diffusion } D_t} \\
& + \underbrace{\frac{1}{Le_i}\nabla\cdot(\rho D\nabla Z_2)\frac{\partial Y_i}{\partial Z_2} + \frac{1}{Le_i}\nabla\cdot(\rho D\nabla Z_3)\frac{\partial Y_i}{\partial Z_3}}_{\text{Tangential convection } C_t} \\
& + \underbrace{\nabla\cdot(\rho Y_i\mathbf{V_{c,i}})}_{\text{Correction terms } R},
\end{aligned}
\tag{4.8}
$$

where

$$
\begin{aligned}
\chi &= 2D|\nabla Z|^2, \\
\chi_k &= 2D|\nabla Z_k|^2, \text{ for } k = 2, 3.
\end{aligned}
\tag{4.9}
$$

In the above equation, some quantities, such as $\nabla\cdot(\rho D\nabla Z)$, are defined in physical space, but can be mapped into phase space, (Z, Z_2, Z_3).

The second term on the left hand side (LHS) is the Lagrangian transport of the flamelet in the Z_2 and Z_3 directions. The third term on the LHS represents convection in mixture fraction. The first term on the right hand side (RHS) is the normal diffusion term in mixture fraction. The third and fourth terms on the RHS represent diffusion terms within the iso-surfaces of mixture fraction. They will be referred to as *tangential diffusion*. The fifth and sixth terms represent convection of Y_i along Z iso-surfaces. They will be referred to as *tangential convection*. The last term on the RHS is the unprocessed correction terms from the species transport equations (Eq. 2.8). As will be shown

later, this term is often negligible. The detailed derivation leading to the above equation is included in Appendix. B.1.

4.1.4 Previous flamelet formulations with curvature effects

The above equation in mixture fraction space (Eq. 4.8) is mathematically equivalent to the original species transport equation (Eq. 2.8) as no assumptions have been made in its derivation. Under unity Lewis number assumption, this equation is proved almost identical to the very first flamelet equations initially proposed by Williams in 1975 [72] (revised later by the same author [52] to include one additional term, which was missing in [72]). A detailed comparison with Williams' formulation is shown in Appendix. B.2. More recently, there have been several attempts in the derivation of general flamelet equations including curvature effects [73, 75]. However, restrictive assumptions (*e.g* thin flame) were made implicitly in the derivations in [73] and the flamelet equations proposed in [75] were only valid under specific conditions. The mathematical inconsistencies in these previously derived curved flamelet formulations are discussed in Appendix. C.

The current form of the equations distinguishes itself from the other formulations mentioned above for three reasons. First, no explicit simplifying assumption is made in the derivation, which makes the current formulation free of mathematical inconsistencies. Second, the effects of different processes can be explicitly identified. Finally, the current form is equivalent to the species transport equations in physical space (Eq. 2.8), which makes it more general than previously derived equations.

4.1.5 Convection in mixture fraction coordinate system

Compared to the case when unity Lewis number is assumed, one additional term appears. This is a convective term in mixture fraction space, with convective velocity $\left(1-\frac{1}{Le_i}\right)\nabla\cdot(\rho D\nabla Z)$ for species i. A reduced form of this term has been considered by Pitsch and Peters [112] in the case of flat planar flamelets. The normalized velocity in mixture fraction space can be split exactly into

two parts and expressed as

$$\nabla \cdot (\rho D \nabla Z) = \mathbf{n} \cdot \nabla(\rho D |\nabla Z|) + \rho D \, |\nabla Z| \, \nabla \cdot \mathbf{n}. \tag{4.10}$$

This splitting technique has been used previously for the modeling of both premixed [16] and non-premixed flames [32, 117]. The normal vector to the iso-surface of mixture fraction in the above equation is defined as

$$\mathbf{n} = \frac{\nabla Z}{|\nabla Z|}. \tag{4.11}$$

The first term on the right hand side of Eq. 4.10 leads to the convective term already included in the conventional flamelet formulation derived for flat flames by Pitsch and Peters [112]. This term can be further expressed as

$$\begin{aligned} \mathbf{n} \cdot \nabla(\rho D |\nabla Z|) &= |\nabla Z| \frac{\partial}{\partial Z}(\rho D |\nabla Z|) \\ &= \left(\frac{\chi}{2D}\right)^{1/2} \frac{\partial}{\partial Z}\left[(\rho D)^{1/2}\left(\frac{\rho\chi}{2}\right)\right] \\ &= \frac{1}{4}\left(\frac{\partial \rho\chi}{\partial Z} + \frac{\chi}{D}\frac{\partial \rho D}{\partial Z}\right) \end{aligned} \tag{4.12}$$

The second term on the right hand side of Eq. 4.10 leads to

$$\rho D \, |\nabla Z| \, \nabla \cdot \mathbf{n} = \rho \kappa \sqrt{\frac{\chi D}{2}}, \tag{4.13}$$

with the curvature of the local iso-surface of mixture fraction, κ, defined as

$$\kappa = \nabla \cdot \mathbf{n}. \tag{4.14}$$

This second term embodies the effects of curvature on the flamelet structure and is proportional to the local curvature of the mixture fraction iso-contours. The curvature of mixture fraction iso-surface as defined in Eq. 4.14 corresponds to the mathematical definition of the *mean* curvature of a surface.

The Convection term in mixture fraction C_Z (Eq. 4.8) can be therefore split into two terms

$$\underbrace{\left(1-\frac{1}{Le_i}\right)\nabla\cdot(\rho D\nabla Z)}_{\text{Convection in mixture fraction } C_Z} = \underbrace{\frac{1}{4}\left(1-\frac{1}{Le_i}\right)\left(\frac{\partial\rho\chi}{\partial Z}+\frac{\chi}{D}\frac{\partial\rho D}{\partial Z}\right)}_{\text{Normal convection } C_1} + \underbrace{\left(1-\frac{1}{Le_i}\right)\rho\kappa\sqrt{\frac{\chi D}{2}}}_{\text{Curvature } C_K}. \tag{4.15}$$

Without loss of generality, the above expression can be used to replace the C_Z term in Eq. 4.8.

4.1.6 One-dimensional curved flamelets

In this subsection, assumptions are considered to simplify the exact, three-dimensional, flamelet equations presented in Eq. 4.8. Assuming that the flame is described locally by an essentially one-dimensional structure, the derivatives with respect to Z_2 and Z_3 may be neglected. This leads to the final form of the one-dimensional flamelet equations

$$\rho\frac{\partial Y_i}{\partial\tau}+\left(1-\frac{1}{Le_i}\right)\left[\frac{1}{4}\left(\frac{\partial\rho\chi}{\partial Z}+\frac{\chi}{D}\frac{\partial\rho D}{\partial Z}\right)+\rho\kappa\sqrt{\frac{\chi D}{2}}\right]\frac{\partial Y_i}{\partial Z}=\frac{\rho\chi}{2Le_i}\frac{\partial^2 Y_i}{\partial Z^2}+\dot{\omega}_i. \tag{4.16}$$

It is important to note that the *one-dimensionality* of the above flamelet equations refers to the new coordinate system (Z, Z_2, Z_3) and not to the original Cartesian one (x_1, x_2, x_3). The correction terms ensuring zero net diffusion flux are not shown in the above equations for clarity. The complete one-dimensional flamelet equations including correction terms are provided in Appendix. B.3.

Although the convective term already included in the conventional flamelet formulation (Eq. 4.12) may change its direction for different Z values, the sign of the curvature-induced convective term is fully determined by that of curvature. When the local mixture fraction iso-contour is convex (the center of curvature lies on the rich side of the mixture), the positive curvature induces a convective velocity towards large mixture fraction for species with $Le > 1$ but towards small mixture fraction for species with $Le < 1$. Opposite conclusions can be drawn for negative curvature values (concave local mixture fraction iso-contour, the center of curvature lies on the lean side of the mixture).

The above equation states that curvature has no effects on the transport of species with unity

Lewis number in mixture fraction space. It is the only difference with the flamelet equations proposed by Kortschik *et al.* [73], derived using the coordinate transformation proposed by Peters [49, 50] (Eq. 4.1).

4.1.7 Magnitude of curvature term

The importance of the curvature-induced convective term can be assessed by comparing its magnitude to that of the original convection term. The ratio, ϕ, of the magnitudes of the two convective terms can be expressed as

$$\phi = \frac{\rho\,|\kappa|\,\sqrt{\frac{\chi D}{2}}}{\left|\frac{1}{4}\left(\frac{\partial \rho\chi}{\partial Z} + \frac{\chi}{D}\frac{\partial \rho D}{\partial Z}\right)\right|} = \frac{2\sqrt{2}\,|\kappa|\,\sqrt{D}}{\left|\sqrt{\chi}\left[\frac{1}{D}\frac{\partial D}{\partial Z} + \frac{1}{\chi}\frac{\partial \chi}{\partial Z} + \frac{2}{\rho}\frac{\partial \rho}{\partial Z}\right]\right|}. \tag{4.17}$$

Based on the approximation that the molecular diffusivity of the mixture fraction D varies with the temperature typically as $T^{\frac{3}{2}}$ [118] and the density ρ is inversely proportional to the temperature, the following estimate could be made:

$$\frac{2}{\rho}\frac{\partial \rho}{\partial Z} \sim -\frac{2}{T}\frac{\partial T}{\partial Z}, \frac{1}{D}\frac{\partial D}{\partial Z} \sim \frac{3}{2T}\frac{\partial T}{\partial Z}. \tag{4.18}$$

The temperature profile may be approximated using the Burke-Schumann solution on the rich side

$$T\left(Z\right) = T_{st} + \left(T_u - T_{st}\right)\frac{Z - Z_{st}}{1 - Z_{st}}, \tag{4.19}$$

and where T_{st} is the stoichiometric temperature, Z_{st} is the stoichiometric mixture fraction, and T_u is the unburnt temperature. Similarly, the temperature profile may be approximated on the lean side as

$$T\left(Z\right) = T_{st} - \left(T_u - T_{st}\right)\frac{Z - Z_{st}}{Z_{st}}. \tag{4.20}$$

With this approximation, $\frac{1}{T}\frac{\partial T}{\partial Z}$ is estimated to be of order unity (or less) if the stoichiometric

mixture fraction value is relatively small. Therefore,

$$\frac{1}{D}\frac{\partial D}{\partial Z} + \frac{2}{\rho}\frac{\partial \rho}{\partial Z} \sim O(1). \tag{4.21}$$

Alternatively, the left hand side of Eq. 4.21 can be estimated to be zero if the Chapman approximation

$$\rho^2 D = C, \tag{4.22}$$

where C is a constant, is assumed.

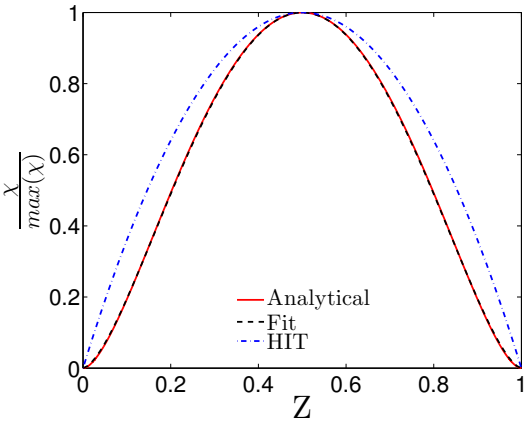

Figure 4.2: Functional dependence of scalar dissipation rate on mixture fraction. Red solid line: Eq. 4.23. Black dash line: Eq. 4.24. Blue dash-dotted line: Eq. 4.25.

The dissipation rate can be estimated as $\chi \sim Z^{\alpha}$ [16, 49], with $\alpha > 1$, for small mixture fractions around the stoichiometric value. For instance, the theoretical functional dependence of scalar dissipation rate on mixture fraction, derived analytically for counterflow diffusion flames and reacting mixing layers [16, 49] predicts

$$\chi(Z) \propto \exp\left[-2\mathrm{erfc}^{-1}\left(2\mathrm{Z}\right)\right]^2. \tag{4.23}$$

Using this expression, the exponent α can be estimated to be $\alpha \simeq 2$ when a Taylor expansion of the above expression is considered around $Z = 0$. In addition, the theoretical profile (Eq. 4.23) can be

well fitted for all mixture fraction values (except in the vicinity of $Z = 0$ and $Z = 1$) using

$$\chi(Z) \propto Z^{1.6}(1-Z)^{1.6}, \tag{4.24}$$

as shown in Fig. 4.2. This leads to the scaling $\alpha \simeq 1.6$ for small mixture fraction values. Finally, the dependence of the mean scalar dissipation rate on mixture fraction has been found to be well represented by

$$\chi(Z) \propto Z(1-Z), \tag{4.25}$$

in homogeneous isotropic turbulence (HIT) [119, 120] (Fig. 4.2). This leads to $\alpha \simeq 1$ for small mixture fraction values. Overall, the scaling $\chi \simeq Z^{\alpha}$ with $1 \leq \alpha \leq 2$ provides a reasonable approximation for the scalar dissipation rate at small mixture fractions. Therefore,

$$\left| \frac{1}{\chi} \frac{\partial \chi}{\partial Z} \right| \sim \frac{\alpha}{Z}, \tag{4.26}$$

is estimated to be one order of magnitude larger than $\frac{1}{T}\frac{\partial T}{\partial Z}$ close to the flame front. Based on the above analysis, the ratio, ϕ, can be simply estimated as

$$\phi \sim \frac{2|\kappa|Z}{\alpha\,|\nabla Z|}. \tag{4.27}$$

Using the definition of the flame thickness for a diffusion flame

$$l_F = \frac{(\Delta Z)_F}{|\nabla Z|_{st}}, \tag{4.28}$$

where $(\Delta Z)_F \simeq 2Z_{st}$ [16], ϕ is simplified to be the ratio between the local radius of the mean curvature and the diffusion flame thickness

$$\phi \sim \frac{|\kappa| l_F}{\alpha}. \tag{4.29}$$

The above magnitude comparison suggests that the curvature-induced convection is important when the radius of curvature is comparable to or smaller than the flame diffusion thickness. On the other hand, the flamelet can be regarded as flat if the local radius of curvature of mixture fraction is much larger than the flame diffusion thickness, consistent with the flat flame assumption [112].

It is important to note that large hydrocarbon molecules such as PAH are formed on the rich side away from the flame front. As will be shown later (Fig. 4.15), for planar flamelets, this occurs around $Z = 0.4$, while for curved flamelets, this occurs around $Z = 0.2$. It is worth pointing out that these values are specific to the test case considered in the current work and may not be universal. At these locations, the coefficient α is much smaller than its value at the flame front since the local variation of scalar dissipation rate with respect to mixture fraction is much weaker. Therefore, even with small curvature values, the ratio ϕ can be large at the location where PAH molecules are formed, which makes retaining the curvature term necessary.

4.2 Curved flamelet modeling

For the proper integration of the flamelet equations, the scalar dissipation rate and curvature dependences on mixture fraction, $\chi(Z)$ and $\kappa(Z)$, need to be modeled [112], since the tabulated chemistry approach requires the *a priori* knowledge of χ and κ in the flamelet formulation described by Eq. 4.16 to establish the flamelet database before the flow simulation.

This section considers two basic configurations that represent typical mixing fields in moderately turbulent flows with curved local mixture fraction iso-surfaces. Both of these configurations are intrinsically one-dimensional. As such, the flamelet equations (Eq. 4.16) are mathematically exact (with the correction terms in Appendix. B.3). The functional dependence of scalar dissipation rate and curvature values on mixture fraction is investigated in these cases under various assumptions.

4.2.1 Tubular counterflow diffusion flames

Inspired by the use of planar stretched laminar flamelets in modeling non-premixed flames [16], tubular stretched laminar flamelets could be a useful tool in investigating the combined effects

of stretch and curvature. The tubular counterflow configuration is advantageous since it can be treated as an essentially one-dimensional flamelet structure, under the assumption of a sufficiently long tubular burner. This configuration mimics highly stained regions between two large vortices in a turbulent flow. Experimentally, the opposed tubular burner was first proposed by Ishizuka [121]. The schematic of such a configuration is depicted in Fig. 4.3(a). Curvatures of the mixture fraction iso-surfaces ranges from $1/R_2$ to $1/R_1$, where R_1 is the radius of the inner tube and R_2 is that of the outer tube.

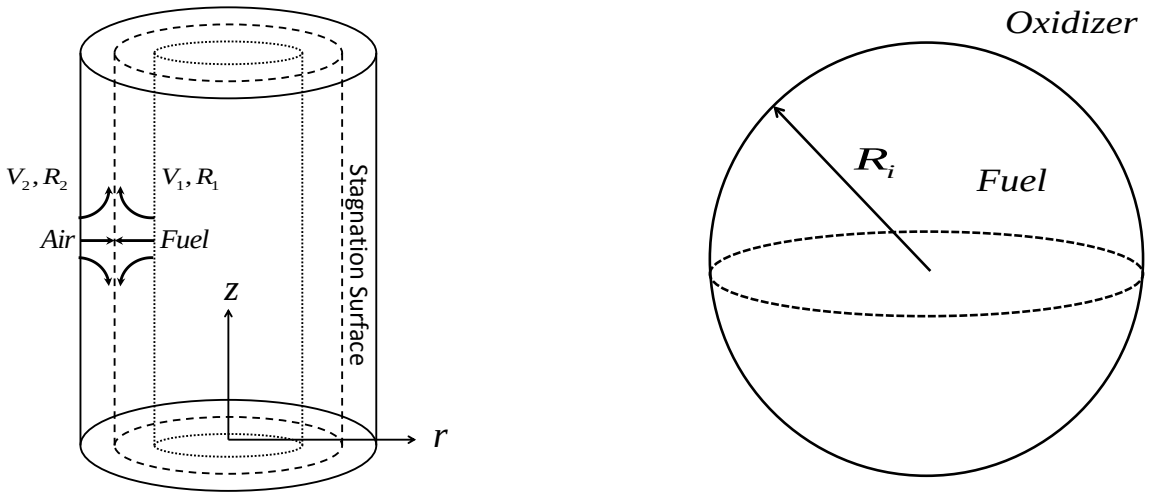

(a) Opposed tubular counterflow burner.

(b) Unsteady spherical diffusion flames.

Figure 4.3: Two basic configurations representing local 1D flamelet structures in turbulent reacting flows.

For the case of equal velocities ($V_1 = -V_2 = V$), analytical solutions for the radial velocity $U_r(r)$ and the stretch rate at the stagnation surface a_s have been proposed for the cold flow problem [122] by assuming constant density in the momentum equation:

$$U_r(r) = \frac{VR_1}{r} \cos\left[\frac{\pi R_2}{2(R_2 - R_1)}\left(\frac{r^2}{R_1 R_2} - \frac{R_1}{R_2}\right)\right], \tag{4.30}$$

$$a_s = \frac{\pi V}{(R_2 - R_1)}. \tag{4.31}$$

The same assumption of constant density was made already in the original derivation for the scalar dissipation rate dependence of the mixture fraction (Eq. 4.23), $\chi(Z)$, for planar counterflow diffusion

flames [16].

Case	Inner radius $R_1\,(m)$	Outer radius $R_2\,(m)$	Injection velocity $V\,(m/s)$	Stretch $a_s\,(1/s)$
1	0.003	0.015	0.5	130.8
2	0.003	0.015	0.3	78.5
3	0.003	0.03	0.5	58.1
4	0.006	0.015	0.5	174.4
5	0.006	0.03	1	130.8

Table 4.1: Different sets of boundary conditions used in tubular flow calculations.

Under these conditions, the transport equation for mixture fraction is reduced to

$$U_r \frac{\partial Z}{\partial r} = \frac{\rho D}{r} \frac{\partial}{\partial r} \left(r \frac{\partial Z}{\partial r} \right). \tag{4.32}$$

This equation does not admit any simple analytical solution and hence is solved numerically for various inner and outer tube radii and injection velocities, which are listed in Table 4.1. The resulting mixture fraction, scalar dissipation rate, and curvature profiles are shown in Fig. 4.4. The mixture fraction varies from its minimum to its maximum over a very small radial displacement r. As a result, the regions where pure fuel or pure oxidizer are found ($Z = 1$ or $Z = 0$) spread over wide ranges of radial displacement. Therefore, large gradients in curvature are observed at both $Z = 1$ and $Z = 0$ in Fig. 4.4(c).

The scalar dissipation profiles appear to collapse onto a single curve in mixture fraction space when normalized by their respective maximum values. The normalized curves can be once again represented very well by the analytical expression derived for the planar counterflow flame (Eq. 4.23).

The raw curvature profiles are normalized by the maximum of mixture fraction gradient, since it provides a lower limit of the estimated ratio ϕ (Eq. 4.27). The normalized curvature profiles show that the variation in curvature is relatively small compared to the mean curvature value in all test cases. The only exception is found at $Z = 0$ and $Z = 1$. This is expected since the

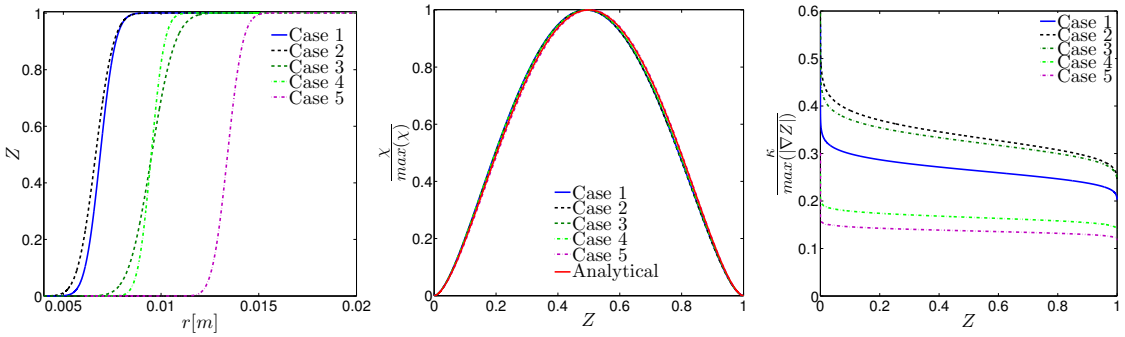

(a) Mixture fraction. (b) Normalized scalar dissipation rate. (c) Normalized curvature.

Figure 4.4: Mixture fraction, scalar dissipation rate, and curvature profiles for steady-state counter-flow tubular flames.

tubular flow is relatively highly strained. Interestingly, the curvature value does not vary much from stoichiometry to the locations where large hydrocarbons are formed ($Z \simeq 0.4$). Therefore, curvature can be treated to be constant for all Z to the first approximation. In this configuration, a negative curvature corresponds to the case where fuel flows outwardly from the inner tube and oxidizer flows inwardly from the outer tube, and a positive curvature corresponds to the case where fuel flows inwardly from the outer tube and oxidizer flows outwardly from the inner tube. Zero curvature corresponds to the limiting case when both inner and outer tube radii are extremely high, so curvature effects are negligible.

4.2.2 Unsteady spherical inter-diffusion layer

The second configuration investigated in this work is the unsteady laminar spherical diffusion flame. This case describes the situation in which a finite amount of fuel is placed initially in a sphere of radius R_i surrounded by air or a sphere of air surrounded by fuel. The two fluids are allowed to abruptly inter-diffuse and generate a growing mixing layer. Once again, this configuration is inherently one-dimensional. A schematic is shown in Fig. 4.3(b). This configuration is representative of events found in turbulent flames, such as a pocket of fuel trapped by the surrounding air or an evaporating droplet of fuel surrounded by the oxidizer. In this configuration, a negative curvature corresponds to the case where fuel is placed inside the sphere, and a positive curvature corresponds to the case

where oxidizer is placed in the sphere with fuel surrounding it.

The transport equation for mixture fraction is reduced to, for the special case of constant (with r) diffusivities,

$$\rho \frac{\partial Z}{\partial t} = \frac{\rho D}{r^2} \frac{\partial}{\partial r} \left(r^2 \frac{\partial Z}{\partial r} \right). \tag{4.33}$$

The above transport equation for mixture fraction is solved numerically in spherical coordinates for various initial separation radii.

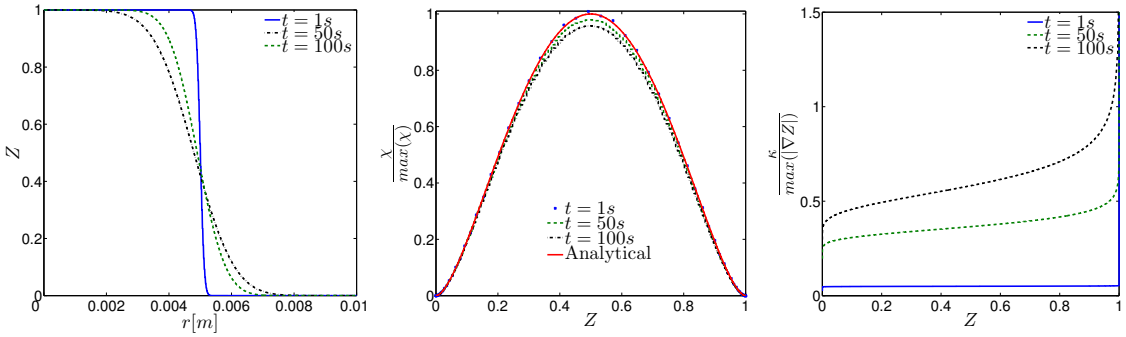

(a) Mixture fraction. (b) Normalized scalar dissipation rate. (c) Normalized curvature.

Figure 4.5: Mixture fraction, scalar dissipation rate, and curvature profiles for a spherical laminar unsteady mixing layer.

The resulting mixture fraction, normalized scalar dissipation rate (by its maximum), and normalized curvature profiles (by the maximum gradient of mixture fraction) are shown in Fig. 4.5 for initial separation radius $R_i = 0.005m$. The shape of these normalized scalar dissipation rate profiles is independent of R_i. Once again, the normalized profiles collapse very well onto the curve given by Eq. 4.23, indicating that the functional dependence of χ on Z is the same as the previous case over time. For curvature, the variation in Z becomes larger with time. However, the assumption of constant curvature is still valid for early stages of mixing and remains reasonable at later times (variations less than 20% at $t = 100s$).

4.2.3 Summary

Based on the steady-state counterflow tubular diffusion flame or the spherical laminar temporally evolving mixing layer, this *a priori* analysis shows that

- Equation 4.23 provides a reasonably reliable approximation for the scalar dissipation rate even for curved flamelets,
- the curvature can be assumed to be constant to the first approximation.

Since these configurations are quite different mechanisms of mixing, the functional dependence $\chi(Z)$ and $\kappa(Z)$ could be used legibly for more general flows.

4.2.4 Flamelet solutions with curvature effects

One-dimensional flamelet calculations are performed in this section to investigate the effects of curvature on the mass fraction profiles of species with different Lewis numbers. The complete curved flamelet equations provided in Appendix. B.3 (and in Eq. 4.16 without the correction terms) are solved.

The representative flamelet uses a methane/nitrogen mixture as fuel, injected at $425K$, and air as oxidizer, injected at $300K$. The corresponding stoichiometric mixture fraction value is $Z_{st} = 0.124$. The flamelet is calculated at 1 atm. These parameters are chosen to match the configuration of the full chemistry simulation of the co-flow diffusion flame in the next section. The full chemistry mechanism developed by Blanquart and coworkers [3, 33] is used, just as for the simulations shown later in Section 3. The scalar dissipation rate profile is imposed as Eq. 4.23, with the stoichiometric value $\chi_{st} = 1s^{-1}$. This value is representative of values found in the full chemistry simulation. The curvature is set to be $\kappa = \pm 200m^{-1}$ and kept constant. The magnitude of the assigned curvature values is relatively moderate since the ratio between the flame thickness and the radius of curvature is estimated to be

$$|\kappa| \cdot l_F \simeq 3, \tag{4.34}$$

with the flame thickness being calculated with Eq. 4.28. Resulting mass fraction profiles for H_2 ($Le = 0.28$), C_2H_2 (Le = 1.2), and C_6H_6 ($Le = 2.3$) are compared against those of a planar flamelet ($\kappa = 0$) under the same conditions in Fig. 4.6.

Figure 4.6 confirms the influence of curvature on the flamelet solutions, consistent with Eq. 4.16.

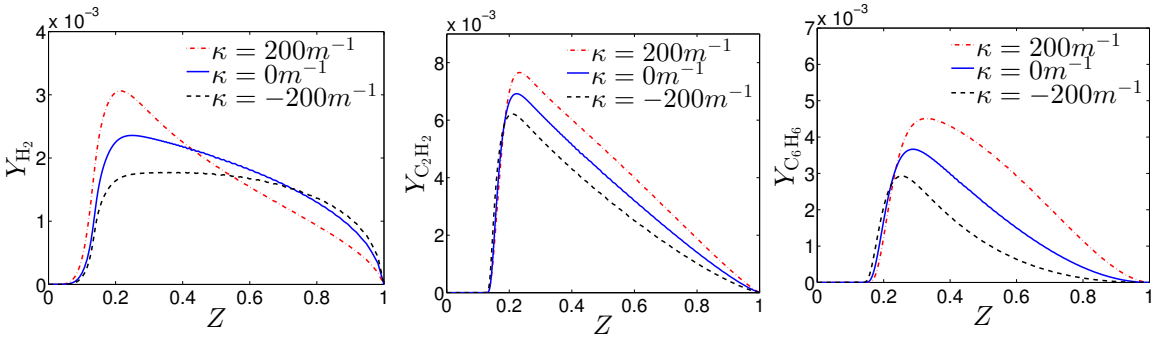

(a) H_2. (b) C_2H_2. (c) C_6H_6.

Figure 4.6: Comparison of H_2, C_2H_2, and C_6H_6 mass fractions between curved and flat flamelets. For comparison, the maximum gradient of mixture fraction is calculated to be $103m^{-1}$, leading to a lower limit of the estimated ratio of $\phi = 1.94$ (Eq. 4.27) for the curved flamelets with $\kappa = \pm 200[m^{-1}]$.

More precisely, differential diffusion effects are enhanced by the presence of a negative curvature value. Species with $Le > 1$ are convected towards lower mixture fractions, and species with $Le < 1$ are convected towards larger mixture fractions. Conversely, differential diffusion effects are reduced by the presence of positive curvature value. This results in a change by a factor of two between $\kappa = 200m^{-1}$ and $\kappa = -200m^{-1}$ for the yield of benzene on the rich side. Curvature has only a minor impact on the mass fraction profile of species with Lewis number close to unity. Since the transport of these species is hardly affected by curvature, the observed differences in Fig. 4.6 are primarily because the chemical source terms of these species are affected by other species.

A more visual illustration of the sensitivity of species concentrations to curvature effects κ and scalar dissipation rates χ is shown for benzene (C_6H_6) in Fig. 4.7. The solution of curved flamelet solutions with a series of χ and κ values are shown at a fixed mixture fraction $Z = 0.3$, where C_6H_6 concentration reaches its maximum for $\kappa = 0m^{-1}$.

In order to investigate the influence of assuming a constant curvature, additional flamelet calculations were performed using curvature profiles as linear functions of mixture fraction

$$\kappa(Z) = \kappa(Z_{st}) + \kappa'(Z_{st}) \cdot (Z - Z_{st}) \tag{4.35}$$

The linear profile $\kappa(Z)$ is determined by the value and slope of the curvature at stoichiometry,

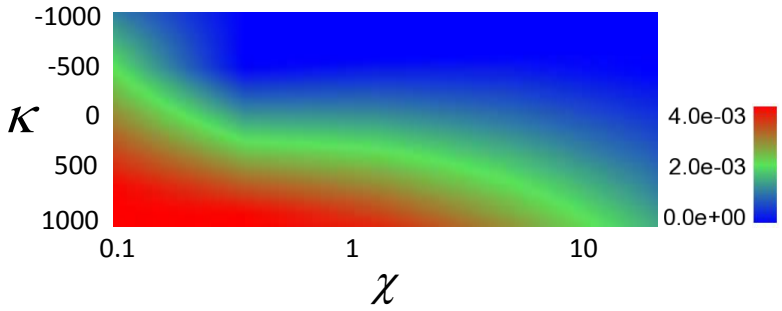

Figure 4.7: Sensitivity of C_6H_6 concentration to curvature effects and scalar dissipation rates at mixture fraction $Z = 0.3$.

$\kappa(Z_{st})$ and $\kappa'(Z_{st})$, respectively. The stoichiometric value $\kappa(Z_{st})$ is assigned, and the slope $\kappa'(Z_{st})$ is determined by

$$\kappa'(Z_{st}) = \left(\frac{\chi_{st}}{2D_{st}}\right)^{-\frac{1}{2}} \tag{4.36}$$

The resulting flamelet solutions turned out to be very similar to those obtained with constant assigned curvature, as illustrated for H_2 in Fig. 4.8.

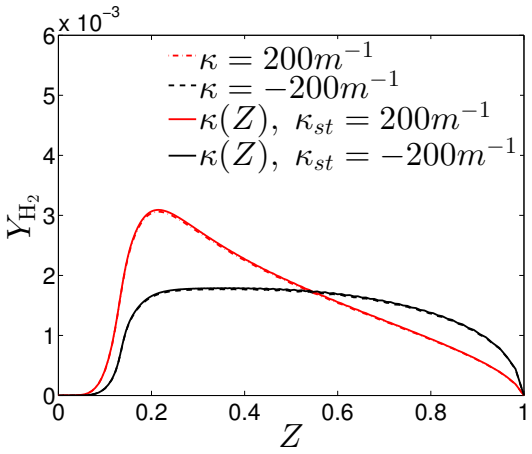

Figure 4.8: Comparison between the flamelet solutions for the mass fraction of H_2 obtained using constant and mixture-fraction-dependent (Eq. 4.35) curvatures.

4.3 Curvature effects in multi-dimensional configurations

In this section, the effects of curvature are investigated in multi-dimensional contexts, and highlighted on the same axisymmetric laminar co-flow diffusion flame [93] studied in the previous chapter.

4.3.1 Tangential diffusion

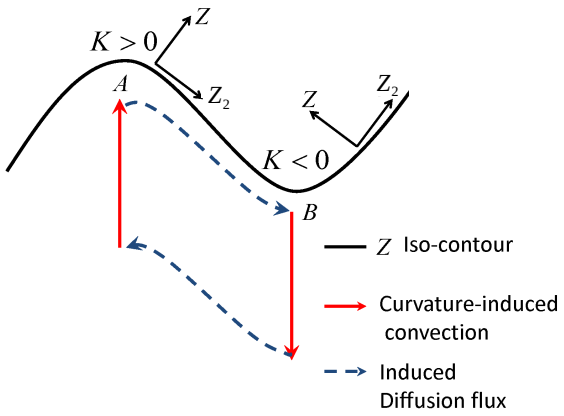

Figure 4.9: Schematic of the curvature-induced tangential diffusion process for a species with Lewis number less than unity.

For general multi-dimensional non-premixed reacting flows, the local scalar dissipation rate χ and mean curvature κ cannot be parametrized only as a function of the mixture fraction Z. Instead, χ and κ are generally dependent also on the curvilinear coordinate, Z_2 and Z_3, along Z iso-contours, leading to $\chi = \chi(Z, Z_2, Z_3)$ and $\kappa = \kappa(Z, Z_2, Z_3)$. In other words, the flame stretch and curvature are not uniform along a Z iso-contour. These non-uniformities might introduce tangential diffusion, *i.e.* diffusion in the direction tangent to the flame front, in both flat and curved flames.

A two-dimensional example of a curved flame with varying curvature along a mixture fraction iso-contour is depicted in Fig. 4.9. In this figure, it is assumed that a region with positive curvature (point A) is found close to a region with negative curvature (point B) on a Z iso-contour. As described previously, the convection induced by the positive curvature will increase the mass fraction of species with $Le < 1$ in the region close to point A. On the contrary, the convection induced by the negative curvature will decrease the mass fraction of those species in the region close to point B. This process generates a gradient in the species mass fraction along a Z iso-contour, thereby, inducing a tangential diffusion flux along the same Z iso-contour. Similarly, a tangential diffusion flux in the opposite direction is induced for species with $Le > 1$. Under these conditions, it is conceivable that the flamelet assumptions might be violated because diffusion does not occur purely in the Z direction. Stated differently, the dependence of the curvature κ on the curvilinear coordinate Z_2

may render the problem at least two-dimensional, and the one-dimensional flamelet equations, even including the curvature-induced convective term (Eq. 4.16), may not be sufficient.

These effects have already been highlighted by previous authors [69]. In the limit of unity Lewis number (when curvature effects go away), Verhoeven and coworkers found that one-dimensional flamelets reproduce very accurately the results obtained with full chemistry simulation. These results suggest that the variation of scalar dissipation rate in the curvilinear direction is not strong enough to create noticeable tangential diffusion. On the other hand, when the Lewis number are not unity, they found deviations from full calculation results when planar flamelets are used. These differences were attributed to curvature effects and tangential diffusion.

In the following subsections, the importance of the curvature-induced convection term and the induced tangential diffusion is illustrated in the case of an axisymmetric laminar co-flow diffusion flame.

4.3.2 Curvature-induced convection

Results from the detailed simulations of the axisymmetric co-flow diffusion flame with finite-rate chemistry performed in the previous chapter are used here. The reader is referred to Chapter 3 for complete flame and simulation details. The flame shape has been shown in Fig. 3.3.

Previous work has shown that large deviations are observed on the flame centerline for species mass fraction when full chemistry simulation results are compared against results obtained using conventional flamelet-based chemistry tabulation methods [69]. It has been concluded that the observed deviations are primarily driven by the exclusion of curvature effects in the conventional flamelet formulation. In addition, more recent work [23] (Chapter 3) has shown that the convective velocity along the flame centerline is substantially under-predicted by the conventional planar flamelet model. As mentioned earlier, this is a direct consequence of the flame curvature through Eq. 4.10. To illustrate this, the ratio of the two convection terms (Eq. 4.12 and 4.13), extracted from the full chemistry simulation, is plotted throughout the computational domain along with the mixture fraction field in Fig. 4.10. It can be observed that the curvature-induced convection

term (Eq. 4.13) is indeed predominant close to the centerline, whereas the original convection term (Eq. 4.12) contributes much more than the curvature term further away from the flame axis. The region close to the burner exit is not shown since the ratio ϕ (Eq. 4.17) is mathematically ill-defined in this region.

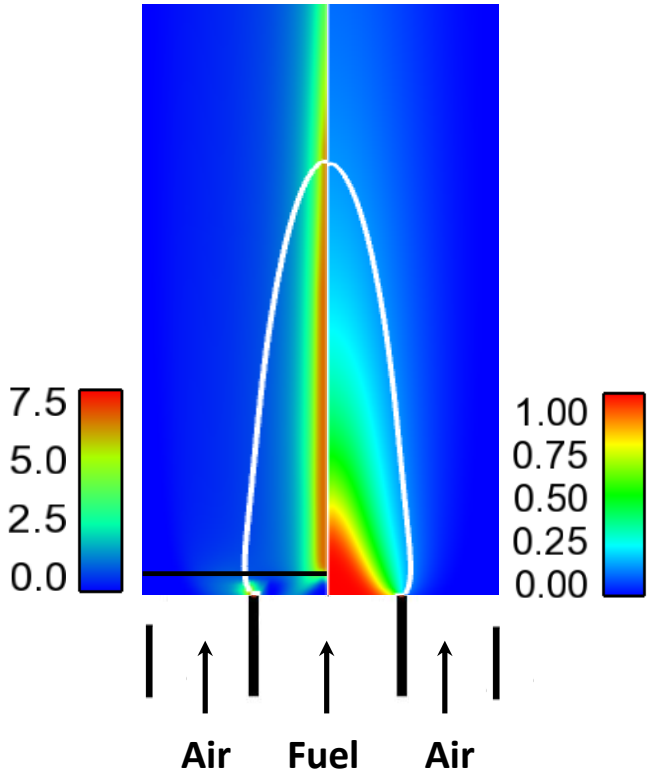

Figure 4.10: Ratio of the curvature-induced convective term over the normal convection term (Eq. 4.29) extracted from the numerical results (on the left) and the mixture fraction contour plot (on the right). The white line denotes the location of the flame front.

.

Figure 4.11 shows a more quantitative comparison of the different terms, namely the conventional flamelet prediction (Eq. 4.12), the curvature-induced (Eq. 4.13), and the total convection terms (sum of both in Eq. 4.10). This is done for two different locations: along the flame centerline and along a radius at the burner exit as indicated by the black solid line in Fig. 4.10. As shown, the main contribution to the actual convective velocity extracted along the flame centerline comes from the curvature induced term. On the other hand, along a radius above the burner exit, the original convective term dominates everywhere with the exception of close to the flame axis. It is not surprising since the centerline exhibits the strongest curvature throughout the flame. Based on the

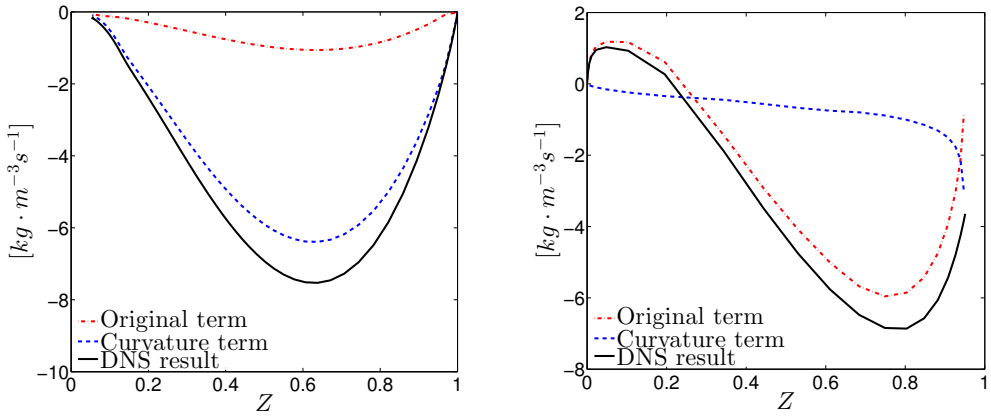

(a) Along flame centerline.

(b) Along flame radius at burner exit (solid black line in Fig. 4.10).

Figure 4.11: Comparison of different convective velocities in mixture fraction space. The "original term" being plotted corresponds to the expression in Eq. 4.12, the "curvature term" being plotted corresponds to the expression in Eq. 4.13, and the "DNS results" being plotted corresponds to the sum of the two previous terms, as expressed by Eq. 4.10.

above considerations, it is expected that the conventional, planar flamelet model should work fine at the edges of the flame (at the burner exit), but not on the centerline at the flame tip. In the remaining of the work, particular attention will be paid to the centerline of the flame studied as the curvature effects are the strongest there.

4.3.3 Budget analysis

To justify the assumption of one-dimensionality for the flamelets (Eq. 4.16) and further investigate the role of curvature in the species transport processes, separate contributions within the flamelet equations (Eq. 4.8) are examined for various species in two regions: along the flame centerline and on a flame radius (indicated by the black solid line in Fig. 4.10) right after the burner exit. These two regions are selected as polar opposites: a low strain region with high curvature parallel to the flow field (flame centerline), and a high strain region with low curvature normal to the flow field (a radius close to the injection).

The complete three-dimensional flamelet equations (Eq. 4.8) can be simplified in this context. First, the time-dependent terms vanish since the flame considered is in steady-state. Second, due to

axisymmetry, the tangential derivatives $\frac{\partial Y_i}{\partial Z_k}$ (along the centerline) vanish. Therefore, the Lagrangian transport term L_t and the tangential convection term C_t are both zero.

For these reasons, the following equation holds:

$$\begin{aligned} \nabla \cdot \left(\rho \frac{D}{Le_i} \nabla Y_i \right) &= \frac{\rho\chi}{2Le_i} \frac{\partial^2 Y_i}{\partial Z^2} + \frac{1}{Le_i} \left(\rho\kappa \sqrt{\frac{\chi D}{2}} + \mathbf{n} \cdot \nabla(\rho D |\nabla Z|) \right) \frac{\partial Y_i}{\partial Z} + D_t \\ &= D_Z + \frac{C_1 + C_K}{Le_i - 1} + D_t. \end{aligned} \tag{4.37}$$

The above equation is used to evaluate D_t. All other terms (D_Z, C_1, and C_K) including the correction term R are calculated using their exact definition as indicated in Eq. 4.8 and Eq. 4.15. The term D_t analytically represents the deviation of the local flame structure from the one-dimensional curved flamelet model. The various terms in Eq. 4.8 are plotted for OH, C_2H_2, and C_6H_6.

For OH, the chemical production term ($\dot{\omega}_i^+$) corresponds to the sum of all productive chemical source terms, and the chemical consumption ($\dot{\omega}_i^-$) gathers all the consuming chemical source terms [16, 123, 124, 125]. It is shown that transport effects such as convection and diffusion are negligible compared to the chemical terms. This is not surprising since the chemical time of OH radical is extremely small compared to the characteristic transport time scale. Therefore, the yield of OH is controlled predominantly by a balance between chemical production and consumption (and not transport processes).

On the contrary, the behavior of C_2H_2 is governed by the balance between various transport processes and chemistry. The corresponding Lewis number for C_2H_2 is $Le_{C_2H_2} = 1.2$. Since this Lewis number is close to unity, the curvature does not strongly affect this species despite the large curvature exhibited on the flame centerline. Similarly, tangential diffusion is shown to be small compared to normal diffusion in mixture fraction space.

Finally, for C_6H_6, the curvature term is much more substantial due to the large Lewis number of this species ($Le_{C_6H_6} = 2.3$). The budget analysis suggests that the behavior of the C_6H_6 mass fraction is governed by a balance between curvature-induced convection, tangential diffusion, and chemistry. The original convection term and the conventional diffusion term (in Z) are shown

to be less important compared to other terms. The current analysis confirms the importance of tangential diffusion on the flame centerline, as previously found by Verhoeven *et al.* [69] and Xuan and Blanquart [23].

Following this budget analysis, we can draw a general picture of the evolution of benzene. Benzene species are produced chemically on the rich side of the flame ($Z \sim 0.35$). They are convected towards the flame front by the strong effects of curvature and ultimately get oxidized ($Z \sim 0.2$). Simultaneously, they are diffused away from the centerline by tangential diffusion ($D_t < 0$ for $Z < 0.4$). Benzene species reappear on the rich side of the flame ($Z > 0.5$) as they are transported to the centerline from off-axis locations due to tangential diffusion ($D_t > 0$ for $Z > 0.5$). Finally, these species are convected towards leaner mixtures under the strong effects of curvature. The combined effects of tangential diffusion and curvature-induced convection is to enhance the transport of species from its production zone ($Z \sim 0.35$) to leaner and richer mixture fractions. This is the main reason why Xuan and Blanquart were able to recast the tangential and normal diffusion terms into a single effective diffusion term [23].

To contrast the effects of flame curvature, the same budget analysis was carried out on a flame radius (indicated by the black solid line in Fig. 4.10) right after the burner exit. This one-dimensional line is selected since its direction is approximately indicated by the gradients of mixture fraction iso-surfaces. Contrary to the centerline, the Lagrangian transport terms L_t and the tangential convection terms C_t are not zero along this line. The Lagrangian terms are calculated using the following expression

$$L_t = \rho \mathbf{u} \cdot \nabla Y_i - \rho \frac{\partial Y_i}{\partial Z} \mathbf{u} \cdot \nabla Z \tag{4.38}$$

For simplicity, the tangential convection terms C_t and tangential diffusion terms D_t are regrouped in a quantity Q and calculated using

$$\nabla \cdot \left(\rho \frac{D}{Le_i} \nabla Y_i \right) = D_Z + \frac{C_1 + C_K}{Le - 1} + Q. \tag{4.39}$$

The results are shown in Fig. 4.13. Since curvature effects are not pronounced on this radial cut

($\kappa \cdot l_F$ small except close to the centerline), curvature-induced convection and tangential diffusion terms are not important. This time, the behavior of most species including C_2H_2 and C_6H_6 is governed by the balance between normal diffusion and chemistry. The yield of OH is once again shown to be controlled by the balance between chemical production and consumption.

The budget analysis is also performed based on the simulation results obtained on a coarser mesh, for the purpose of grid convergence testing. The coarser mesh contains 256×128 grid points, as mentioned in Chapter. 3.1.3. Results are shown in Fig. 4.14 both on the flame centerline and on the selected flame radius, for acetylene as an example. Only the dominant terms in the species budget are shown. There is virtually no difference between the results obtained using the fine and coarse meshes along the flame centerline. Only minor differences are observed between the two simulations along the flame radius. Based on this analysis, the computational grid used for the simulation of this laminar flame (512×256) is sufficient, and allows for more grid points to better resolve the various terms in the species budget.

4.3.4 Comparison between full chemistry results and tabulated chemistry predictions

To further assess the performance of the proposed curved flamelet formulation, a comparison is made between the results from full chemistry simulation (Section 3) and the application of two flamelet-based chemistry tabulation methods. The first method uses conventional planar steady-state flamelets [112]. Therefore, curvature effects are not considered. The flamelet library is constructed *a priori* using flamelet solutions with a series of prescribed scalar dissipation rate values. As such, the species mass fractions are represented as

$$Y_i = Y_i(Z, \chi). \tag{4.40}$$

The second tabulation method is based on the proposed curved steady-state flamelet equations (Eq. 4.16). The flamelet library is established using flamelet solutions with the same prescribed

scalar dissipation rate values and several prescribed curvature values. In this way, the tabulated species mass fractions are represented as

$$Y_i = Y_i(Z, \chi, \kappa). \tag{4.41}$$

Figure 4.15 shows a comparison of species mass fraction profiles obtained from the full chemistry simulation and the two tabulated chemistry methods. As expected, OH is not significantly affected by curvature effects, and the tabulated chemistry results are in excellent agreement with the full chemistry simulation results. Strong convection induced by curvature is observed on the rich side for C_2H_2 and C_6H_6 and is not captured by the chemistry tabulation using planar flamelets. However, tabulation based on curved flamelets is able to predict these effects, and yields significantly improved agreement with full chemistry simulation results. Furthermore, the maximum locations for these species are better predicted by the chemistry tabulation using curved flamelets. Relatively minor differences are observed at large mixture fraction values ($Z > 0.2$) between full chemistry simulation and the chemistry tabulation with curved flamelets. These discrepancies are primarily due to the non-negligible tangential diffusion effects, which are excluded in the current one-dimensional curved flamelet formulation. It is interesting to note that, despite the non-negligible magnitude of tangential diffusion (see Fig. 4.12), one-dimensional flamelets still do a satisfactory job at reproducing the results obtained with full chemistry.

There are two reasons that can potentially explain why the chemistry tabulation using one-dimensional curved flamelets (with tangential terms omitted) gives remarkable results compared to the full chemistry simulation. The first reason is that the species mass fractions are nearly zero, where tangential diffusion is the highest. Second, tangential diffusion and convection terms are only non-negligible for species with Lewis number significantly different than unity, which represent mostly minor combustion products with maximum mass fraction values less than 500 ppm. For these reasons, it should not be much of a surprise that modeling tangential diffusion is not necessary to achieve good agreement with the current full chemistry simulation results.

4.4 Discussion

Based on the curved flamelet equations proposed (Eq. 4.16) and the budget analysis of the species transport equation on a laminar co-flow diffusion flame, curvature effects can be generally described in the following cases.

First, if unity Lewis number is assumed for every species, curvature does not have any effect on the flamelet, irrespective of the magnitude of the flame curvature. This is because the curvature-induced convection term is proportional to $1 - \frac{1}{Le_i}$.

Second, for one-dimensional flat flames, the conventional flamelet formulation [112] is perfectly valid. It is typically the case for planar counterflow diffusion flames where the diameter of the burners is considerably larger than the separation distance.

Third, the curved flamelet formulation is valid for perfectly one-dimensional flames with uniform curvature. Such flames include spherical flames or infinitely long tubular flames, for which all parameters are strictly functions of the radial coordinate r, as investigated in Section 2. By symmetry, tangential diffusion cancels for these flow configurations. Since mixture fraction, Z, is a monotonic function of r, all variables can be parametrized strictly as functions of Z. Consequently, the proposed curved flamelet formulation is perfectly consistent for these configurations.

Fourth, for multi-dimensional non-premixed reacting flows, the variation of curvature along a mixture fraction iso-surface may enhance tangential diffusion fluxes, as described in Section 3. Nevertheless, from a flamelet point of view, the flames considered can still be modeled as a collection of piecewise one-dimensional flamelet structures. The non-uniform curvature would enhance diffusion between these flamelets, which might require further modeling efforts. However, even though a non-negligible amount of tangential diffusion is shown through the budget analysis, the largest deviation between the full chemistry simulation results and the planar flamelet-based chemistry tabulation results was found to be the missing curvature effects, which is captured well by curved flamelets.

Finally, the chemistry tabulation based on the curved flamelets is shown to be almost as accurate as the direct simulation results. The computational time of the numerical simulation using this tabulation method takes around 6 hours to reach its final steady-state, which is slightly more expensive

than using the tabulation based on the planar flamelets. Starting with the same initial conditions, the direct simulation on the same flame takes around 20 days before reaching steady-state. Therefore, a factor of almost two orders of magnitude is gained in terms of computational efficiency, while maintaining almost the same level of accuracy, when using chemistry tabulation based on the curved flamelets, compared to direct simulations.

The analysis presented in this work focused on laminar flames. Extending the conclusions to turbulent flames should be done with great care. As will be reviewed in the next chapter, the *effective* Lewis number of the different species has been found to be close to unity [63] in turbulent flames. Under these conditions, the curvature-induced convection becomes negligible because its magnitude is proportional to $1 - \frac{1}{Le}$.

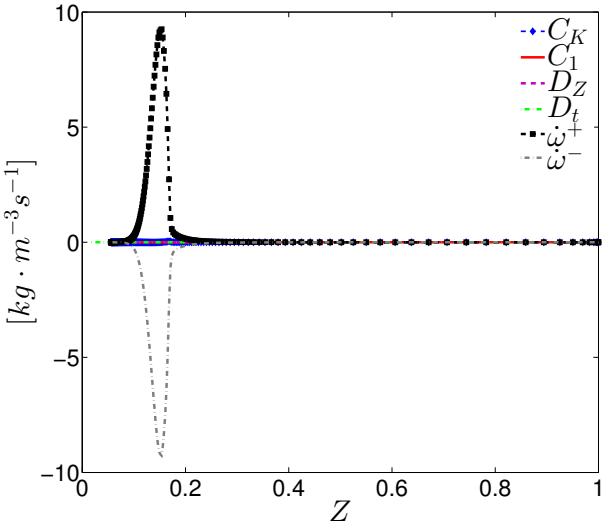

(a) OH.

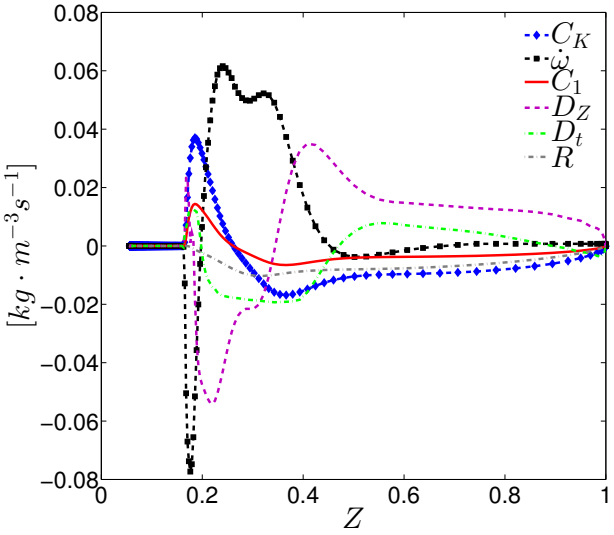

(b) C_2H_2.

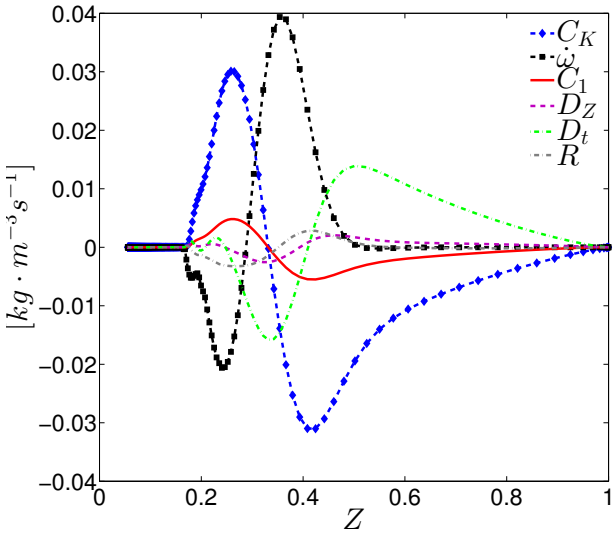

(c) C_6H_6.

Figure 4.12: Budget analysis on the flame centerline for three characteristic species.

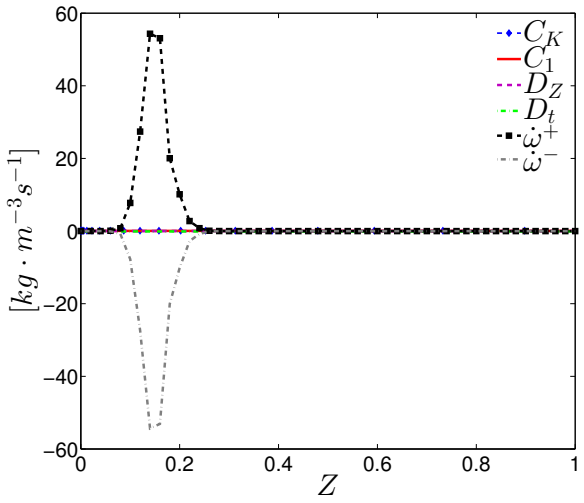

(a) OH.

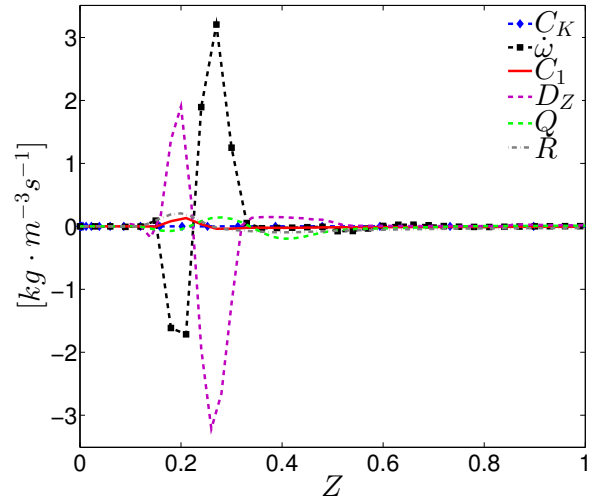

(b) C_2H_2.

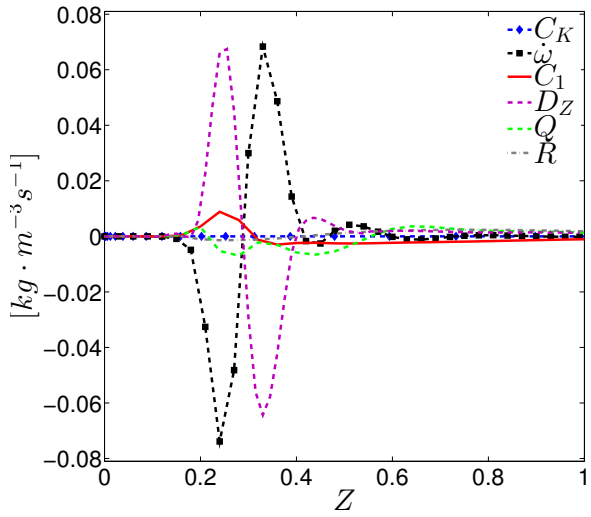

(c) C_6H_6.

Figure 4.13: Budget analysis on a flame radius for three characteristic species. The radial cut corresponds to the black line in Fig. 4.10.

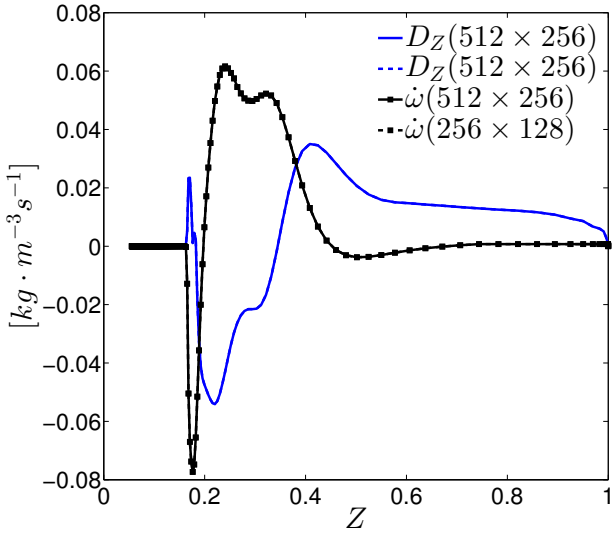

(a) Along the flame centerline.

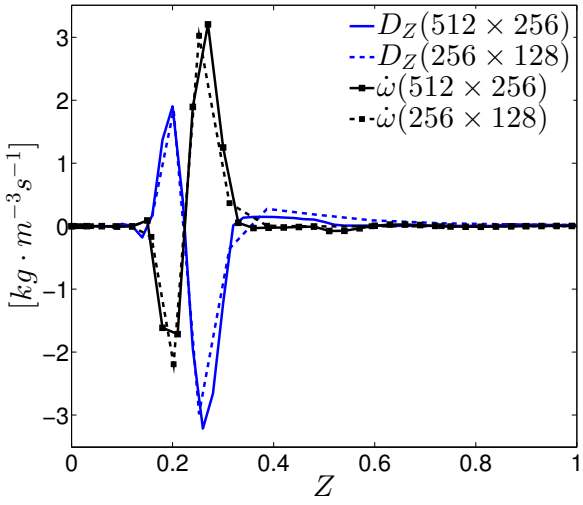

(b) Along the flame radius.

Figure 4.14: Comparison between budget analyses based on simulation results obtained using two different grid resolutions.

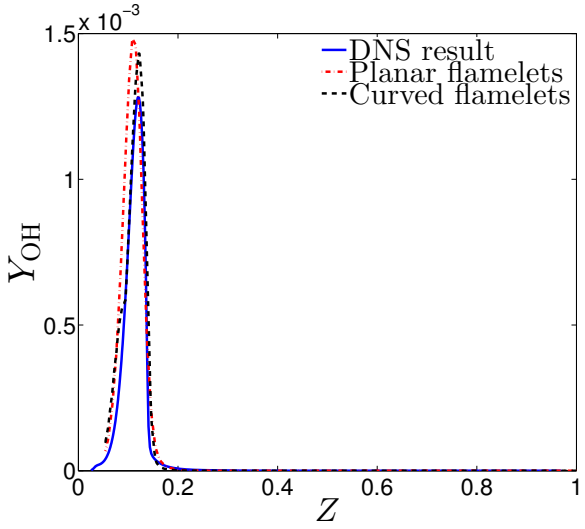

(a) OH.

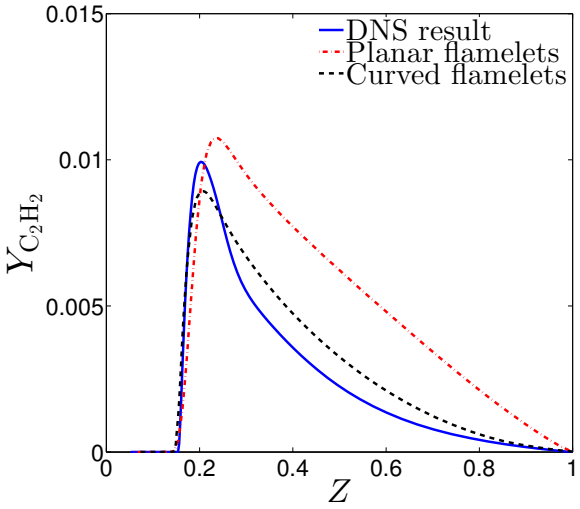

(b) C_2H_2.

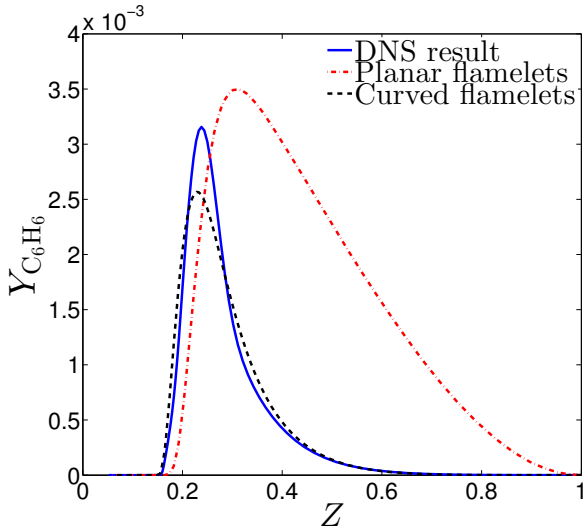

(c) C_6H_6.

Figure 4.15: Mass fraction profiles of several representative species on the flame centerline.

Chapter 5

A flamelet-based chemistry tabulation method for polycyclic aromatic hydrocarbons in turbulent non-premixed flames

This chapter focuses on the modeling of chemistry-turbulence interactions in unsteady, turbulent reacting flows. The objective of the present work is to develop a relaxation model for Polycyclic Aromatic Hydrocarbons (PAH) based on a three-tiered analysis. First, the chemical responses of the unsteady flamelet equations subjected to turbulent perturbations are investigated. Second, the validity of different flamelet-based chemistry tabulation methods is examined for a wide range of species. Third, a new relaxation model for PAH species is developed based on their unsteady responses to turbulent perturbations. The intent of this work is to use unsteady laminar flamelets subject to changes in the scalar dissipation rate as a proxy to gain insight into the responses of PAH to turbulent fluctuations. The unsteady flamelet model is preferred in this work, since it captures the balance between chemistry and diffusion, which has been found to be the dominant process locally in non-premixed flames [16, 49, 50]. On the other hand, reduced-order models that do not take into account diffusion effects, such as Computational Singular Perturbation (CSP) and Intrinsic Low-Dimensional Manifolds (ILDM) would not be the most appropriate for the study of chemistry-turbulence interactions.

This chapter is organized as follows. In Section 1, previous findings on the effective Lewis number

in turbulent non-premixed flame s are briefly reviewed. Section 2 describes the numerical framework of unsteady flamelet calculations and several existing flamelet-based chemistry tabulation methods. In Section 3, the modeling of turbulent effects through scalar dissipation rates is discussed. In Section 4, unsteady calculations are performed to investigate the flamelet responses to modeled turbulent effects. In Section 5, a relaxation model is proposed for PAH species and validated against calculations using full chemistry.

5.1 Turbulent effective Lewis numbers

The effective Lewis number has been used in Reynolds-Averaged Navier-Stokes Simulations (RANS), to provide information about the ensemble/statistical average of the transported quantities (species mass fractions and temperature). The turbulent diffusivity, D_t, is assumed to be identical for all species and temperature. This result is a direct consequence of assuming turbulence mixes all scalars the same way. A similar assumption is made in transported Probability Density Function (PDF) methods [126, 127].

As such, the total diffusivity of species i becomes $D_t + D_i$, where D_i is the molecular diffusivity of species i. The total diffusivity of temperature is $D_t + \alpha$, where α is the thermal diffusivity as introduced in Chapter 2. The effective Lewis number, $\widehat{Le_i}$, of species i in turbulent non-premixed flames is then defined as [16, 128]

$$\widehat{Le_i} = \frac{D_t + \alpha}{D_t + D_i}. \tag{5.1}$$

The effective Lewis number can also be expressed in terms of the species Lewis numbers, Le_i, in laminar flows

$$\widehat{Le_i} = \frac{1 + \frac{D_t}{\alpha}}{\frac{1}{Le_i} + \frac{D_t}{\alpha}}. \tag{5.2}$$

Using a $k - \epsilon$ model for the turbulent viscosity μ_t [129], the turbulent diffusivity can be written as

$$D_t = \frac{\mu_t}{Pr_t} = \frac{C_\mu k^2}{Pr_t \epsilon} \tag{5.3}$$

where ϵ is the turbulent dissipation rate, k is the turbulent kinetic energy, $C_\mu$is the $k-\epsilon$ model coefficient, and Pr_t is the turbulent Prandtl number. Using the same definition for the integral length scale as in [27]

$$l = \frac{u'}{\epsilon}, \tag{5.4}$$

the turbulent kinetic energy [127]

$$k = \frac{3}{2}u'^2, \tag{5.5}$$

and the definition of the mixture Prandtl number Pr, the ratio of the turbulent diffusivity to the thermal diffusivity can be written as

$$\frac{D_t}{\alpha} = \frac{9C_\mu}{4}\frac{Pr}{Pr_t}Re_t, \tag{5.6}$$

where u' is the root-mean-square velocity fluctuation, $Re_t = u'l/\nu$, and ν is the mixture kinematic viscosity. Accordingly, the turbulent effective Lewis number of species i becomes

$$\widehat{Le_i} = \frac{1 + A \cdot Re_t}{\frac{1}{Le_i} + A \cdot Re_t}, \tag{5.7}$$

with the coefficient

$$A = \frac{9C_\mu}{4}\frac{Pr}{Pr_t}. \tag{5.8}$$

More details about the expression for turbulent effective Lewis number can be found in [128].

According to the above analysis, the effective Lewis number of species i recovers its value in laminar flows (Eq. 2.9) when the turbulent diffusivity, D_t, vanishes. In turbulent flows, turbulent transport is expected to have increasing importance relative to molecular diffusion (increasing D_t) as the Reynolds number increases, such that the effects of differential diffusion of non-unity Lewis number species on their mass fraction distributions become less significant as the Reynolds number increases [16, 63]. In the modeling of turbulent flames it is common to evoke the assumption that the Lewis numbers of all species are unity [8, 15, 56, 58, 59, 22, 113, 130, 131].

As *a posteriori* justifications of this assumption, flamelet calculations by Oevermann [132] and Pitsch [70] have shown that assuming unity Lewis number for all species gives the best results for the temperature and all the major species when compared with the hydrogen-air flame of Pfuderer [133]. Additionally, Large-Eddy Simulations (LES) using flamelets with unity Lewis number performed by Pitsch have shown good agreement with experimental measurements [113].

As *a priori* justifications of the unity Lewis number assumption in turbulent reacting flows, Ferreira [134] has compared OH concentration measurements from Barlow and Carter [135] with two different solutions of the flamelet equations. The two solutions are obtained using the mean scalar dissipation rate extracted from the experiments [135], with unity Lewis number and non-unity Lewis numbers, respectively. Only the use of the flamelet equations with unity Lewis number shows a good agreement (See Fig. 3.17 in [16]).

More recently, the competition between differential diffusion and turbulent transport has been systematically studied in a series of piloted methane/air jet flames [63, 136]. The complete series (flame A to flame F) includes laminar, transitional, and turbulent flames spanning a range in Reynolds number from 1,100 to 44,800. The evolution in the relative importance of molecular diffusion and turbulent transport in this series of piloted flames is illustrated in Fig. 5.1 (Fig. 1 in [63]). Conditional mean values of experimentally measured mass fractions are compared against results of steady opposed-flow laminar flame (flamelet) calculations. This comparison indicates that

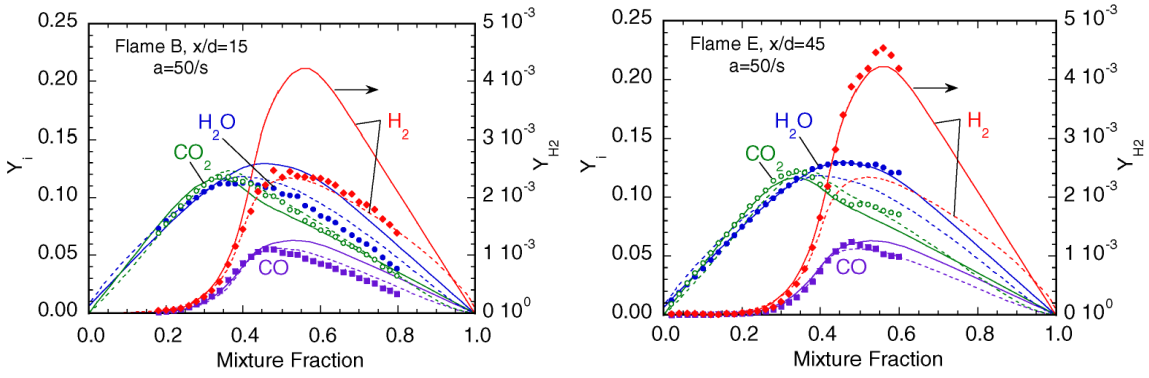

(a) Flame B ($Re \simeq$8200) at $x/d = 15$.

(b) Flame E ($Re \simeq$33,600) at $x/d = 45$.

Figure 5.1: Measured conditional means of species mass fractions (symbols) compared with laminar opposed-flow flame (flamelet) calculations including full molecular transport (dashed lines) or equal diffusivities (solid lines). These figures are taken from Barlow *et al.* [58].

there is an evolution in this flame series from a scalar structure that is strongly affected by molecular diffusive transport to one where turbulent transport appears to be dominant, as the Reynolds number increases. Such dominance justifies the assumption of unity Lewis number transport for a Jet Reynolds number around and greater than 20,000 [63, 66].

Based on the above discussion and the results from the previous chapters, curvature and multi-dimensional diffusion effects are negligible in turbulent non-premixed flames. These effects have been demonstrated, in Chapter 3 and 4, to be substantial only when species transport is described by non-unity Lewis numbers, as it is the case in laminar flames. This makes the application of the conventional flamelet model with unity Lewis number (Eq. 3.1) appropriate in turbulent flames when the Reynolds number is sufficiently large (>20,000).

The major challenge in the flamelet-based modeling of these flames lies in the proper treatment of the strong interactions between gas-phase chemistry and turbulent fluid motion.

5.2 Unsteady Lagrangian flamelet modeling

The general theoretical framework of unsteady flamelet and several flamelet-based chemistry tabulation methods are described in this section.

5.2.1 Unsteady flamelet equations

Unity-Lewis number transport is assumed for all species in the rest of this chapter, since the intent is to examine chemistry-turbulence interaction under highly turbulent flow conditions, where turbulent mixing is the dominant phenomenon [63]. Most of the existing simulations of non-premixed flames (with various combustion models) are based on this simplifying assumption of unity Lewis number [42, 56, 58, 59].

The unsteady flamelet equations are derived in mixture fraction space from the continuity, temperature, and species transport equations using a coordinate transformation (Section 4.1) [49, 50].

The unsteady flamelet equations in the limit of unity Lewis number diffusion can be expressed as

$$\frac{\partial Y_i}{\partial \tau} = \frac{1}{2}\chi\frac{\partial^2 Y_i}{\partial Z^2} + \frac{\dot{\omega}_i}{\rho}, \tag{5.9}$$

where τ is a *Lagrangian* time associated with the motion of the flame [113, 137]. In the equations above, the scalar dissipation rate, χ, representing the inverse of a characteristic diffusion time scale, is defined in Eq. 3.2. Equation 5.9 represents the balance between transient effects, diffusion, and chemistry, and complements the Navier-Stokes equations (i.e. they should be solved simultaneously with the continuity and momentum equations).

5.2.2 Scalar dissipation rate

The scalar dissipation rate, χ, defined by Eq. 3.2, is a substantial quantity in the closure of unsteady laminar diffusion flamelet models. It is essentially a measure of departure of the flamelet structure from thermal equilibrium [138]. It is also the only parameter in the flamelet equations that depends on physical coordinates. Therefore, the influence of the flow field (hence turbulence) is exerted onto the flamelets thoroughly through this parameter. By solving the transport equation of mixture fraction (Eq. 2.6) in physical space, the scalar dissipation rate can be calculated (using Eq. 3.2) at each location of the flow field and each instant in time.

In the current work, the analytical approximation of the functional dependence of the scalar dissipation rate on the mixture fraction proposed by Peters [16] is used. This approximation predicts that

$$\chi(Z,\tau) = \chi_{st}(\tau)\frac{\exp\left[-2\mathrm{erfc}^{-1}\left(2\mathrm{Z}\right)\right]^2}{\exp\left[-2\mathrm{erfc}^{-1}\left(2\mathrm{Z_{st}}\right)\right]^2}, \tag{5.10}$$

where Z_{st} is the stoichiometric mixture fraction, and χ_{st} is the scalar dissipation rate at Z_{st}. Equation 5.10 was derived analytically for counterflow diffusion flames and reacting mixing layers [16, 49], and provides a satisfactory approximation for the dependence of the mean scalar dissipation rate on mixture fraction in homogeneous isotropic turbulent flows [119, 120].

This model suggests that the functional dependence of scalar dissipation rate on mixture fraction is invariant over time, and the magnitude of the scalar dissipation rate profile can be fully determined by its value at stoichiometry, χ_{st} (which may change over time).

5.2.3 Chemistry tabulation methods

The numerical integration of the unsteady flamelet equations in a turbulent flow simulation is possible [113] but computationally expensive. Regularly, instead of such Lagrangian approach, chemical kinetics included in the flamelet formulation is integrated into the flow field simulations through tabulation (Eulerian approach) [6, 8, 15, 22]. Flamelet solutions for a wide range of stoichiometric scalar dissipation rate values are computed *a priori* to generate a flamelet library. Several chemistry tabulation methods exist and are presented below. The validity of these chemistry tabulation methods will be examined species-wise in the following, based on the unsteady flamelet responses to turbulent perturbations.

5.2.3.1 Method I: Chemistry tabulation based on steady-state flamelets

The most widely used approach is the tabulation based on steady-state flamelet solutions [138, 139, 140], under the approximation of negligible transient effects (Eq. 3.1). Steady-state flamelet equations are solved in advance, using a presumed scalar dissipation rate profile (Eq. 5.10) with different values at stoichiometry, χ_{st}. A flamelet library is established based on these results. Species mass fraction, temperature, and other thermochemical quantities resulting from the steady-state solutions are mapped onto (Z, χ_{st}) space, as

$$Y_i = Y_i\left(Z, \chi_{st}\right). \tag{5.11}$$

5.2.3.2 Method II: Chemical source term tabulation

In order to take into account rapid changes in scalar dissipation rate, and slow processes such as the formation of PAH molecules and soot particles, the unsteady term in Eq. 5.9 must be retained.

This would allow a finite-time relaxation towards the steady-state solution. Transient effects can be included for species with slow chemistry, by solving the following transport equation for species i in physical space along with the Navier-Stokes equations [8, 22].

$$\frac{\partial \rho Y_i}{\partial t} + \nabla \cdot (\rho Y_i \mathbf{u}) = \nabla \cdot (\rho D \nabla Y_i) + \dot{\omega}_i \tag{5.12}$$

The chemical source terms for species i can be tabulated using the values calculated from the steady-state flamelet solutions as

$$\dot{\omega}_i = \dot{\omega}_i(Z, \chi_{st}). \tag{5.13}$$

This model assumes that the chemical production and consumption rates of species i are entirely controlled by other species which in turn follow exactly the steady-state flamelet solutions.

5.2.3.3 Method III: Flamelet-based relaxation model for PAH molecules

As pointed out by previous studies [2, 3, 8], the chemical reactions leading to the formation of certain species such as NO_x and PAH are characterized by very large time scales. Consequently, tabulating the chemical source term based on steady-state values may be inadequate for these species. The chemical source term of species i is often dependent on its own mass fraction. Following this observation and assuming that all other species are in steady-state, we get

$$\dot{\omega}_i = \dot{\omega}_i(Z, \chi_{st}, Y_i). \tag{5.14}$$

The transport equation for species i is then solved in physical space along with the Navier-Stokes equations. The challenge now resides in determining the dependence of the chemical source term on the mass fraction. It is important to note that this dependence may not be extracted from steady-state flamelet solutions unless certain assumptions are made.

This model has been used previously for the prediction of NO_x [8, 87] and PAH [22]. The dependence of the chemical source term $\dot{\omega}_i$ of species i on its mass fraction Y_i was assumed to be

linear.

5.3 Turbulent effects modeling

Turbulence modeling through changes in the scalar dissipation rate as well as the numerical configuration and procedure used in the present work are discussed in the following.

5.3.1 Discrete variation in scalar dissipation rate

A number of studies have been directed at understanding the resulting behavior of unsteady laminar diffusion flamelets subjected to unsteady strain rate [82, 83], where sinusoidally varying scalar dissipation rate profiles were used. However, due to the highly non-linear nature of the transport processes and chemical reactions, a frequency-based analysis might not be the most appropriate one.

As discussed in Section 5.2, turbulent effects are exerted onto the flamelet equations uniquely through the scalar dissipation rate, χ. Therefore, it is intuitive to model the effects of turbulent mixing through stochastic variations of this parameter. Previously, Stochastic Differential Equations (SDE) have been used to model the rapid variations of the scalar dissipation rate in turbulent flows [119, 141]. Discretely, it is logical to consider abrupt variations (step changes) in χ as a means to investigate the effects of turbulent perturbations. What remains to be determined now is the magnitude of these step changes.

Previous work [49, 119, 141, 142] suggests that the Probability Density Function (PDF) of the scalar dissipation rate can be reasonably well approximated by a log-normal distribution

$$P(\chi, t) = \frac{1}{\chi\sigma\sqrt{2\pi}} \exp\left(-\frac{(\ln\chi - \mu)^2}{2\sigma^2}\right), \tag{5.15}$$

where μ and σ are the mean and the standard deviation of the log-normal distribution. In other words, the scalar dissipation rate fluctuates around the mean value according to a multiplicative factor whose average amplitude is given by

$$\phi = \frac{\sqrt{\langle \chi''^2 \rangle}}{\langle \chi \rangle} = \left[\exp\left(\sigma^2\right) - 1\right]^{\frac{1}{2}}. \tag{5.16}$$

The standard deviation, σ, is assumed to depend only on the Reynolds number. σ has been estimated from various DNS data of non-premixed turbulent reacting flow simulations, and is found to range from 0.8 to 1.4 [119, 120, 143, 144]. Using an average value of σ, the multiplicative factor ϕ is about 2. This means the scalar dissipation rate may vary from half to twice its mean value.

Since the functional dependence of the scalar dissipation rate on mixture fraction is assumed to be fully determined by Eq. 5.10, the entire profile of scalar dissipation rate fluctuates around the profile proportionally over time with the multiplicative factor ϕ.

5.3.2 Perturbation and relaxation procedure

Based on the above considerations, the relaxation procedure used in the current analysis is shown on a representative S-shaped curve for the mass fraction of C_6H_6 from the flamelet solutions obtained under the configuration described in the next subsection.

- We start from a steady-state solution of the flamelet equations at a given χ_{st}. This starting point is denoted as point A on the burning branch of the S-shaped curve corresponding to the steady-state flamelet solutions in Fig. 5.2.
- Then, the scalar dissipation rate at stoichiometry is abruptly changed to a different value, χ'_{st}, denoted as point B, to model the effects of turbulent unsteadiness.
- Finally, the unsteady flamelet equations (Eq. 5.9) are solved until the solution reaches a new steady-state (point C).

The points A' and B' correspond to the relaxation process from a dfferent initial starting point.

5.3.3 Flamelet configuration and parameters

The operating conditions for the flamelet calculations are chosen to reproduce the conditions found in the laboratory scale turbulent sooting flames investigated at Sandia National Laboratories [94]. The

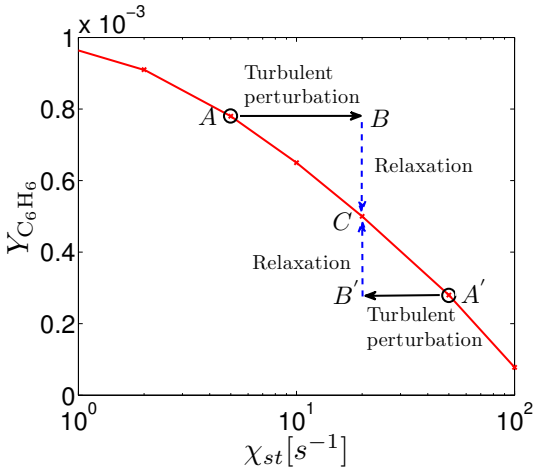

Figure 5.2: The burning branch of the S-shaped curve for the flame configuration considered. The solid line corresponds to the maximum C_6H_6 mass fraction in the solutions of the steady-state flamelet equations. The solid arrows indicate the abrupt change in scalar dissipation rate to model turbulent effects, and the dashed arrows indicate relaxation of the perturbed flamelets towards the final steady-state. Points A and A' correspond to two different initial steady-states; points B and B' correspond to two states after perturbation, and point C corresponds to the final steady-state.

fuel and oxidizer used for the flamelets considered in this work are ethylene and air respectively, both at $300K$. The corresponding stoichiometric mixture fraction value, Z_{st}, is 0.064. The background pressure is set to be at 1 atm. The burning branch of the S-shaped curve is shown for a representative aromatic species, C_6H_6, in Fig. 5.2. The stoichiometric scalar dissipation rate, χ_{st}, at the extinction point is found to be $165s^{-1}$. Local extinction/re-ignition processes are not considered by the current work, since the focus is on the chemical response of a flamelet to turbulent unsteadiness in the fully burning regime.

The response of the species chemical source terms to turbulent perturbations is examined using the unsteady solutions of perturbed flamelets over time. Steady-state flamelets with various initial χ_{st} values are perturbed to various final χ'_{st} values. In the following, results are shown for steady-state flamelets with initial χ_{st} values of $100s^{-1}$, $50s^{-1}$, $10s^{-1}$, and $5s^{-1}$, perturbed to have a new χ'_{st} of $20s^{-1}$. Those values are selected to be reasonably high to represent relatively large departures from thermal equilibrium, typically found in highly turbulent flows. Most of the initial values are selected such that the ratios between the initial and final stoichiometric scalar dissipation rates do not exceed one standard deviation as estimated by Eq. 5.16. The other selected initial scalar

dissipation rates are substantially different from the final value to represent worst case scenarios. It is important to note that such large deviations between the initial and final stoichiometric scalar dissipation rates are not likely to be found in realistic turbulent flows.

The steady and unsteady flamelet equations are solved using the FlameMaster code [103]. The detailed chemistry model employed in the present flamelet calculations was initially developed by Blanquart *et al.* [3, 33]. It contains 168 species and 1878 reactions (forward and backward reactions counted separately) and takes into account all major pathways of PAH formation. Slight modifications have been made to the chemical mechanism since its first publication. The chemistry model is provided in the Supplemental material of [25].

5.4 Relaxation behaviors

The relaxation behaviors for different types of species are described in the following. Numerical results are shown for the relaxation of perturbed flamelets.

5.4.1 Overview of steady-state flamelets

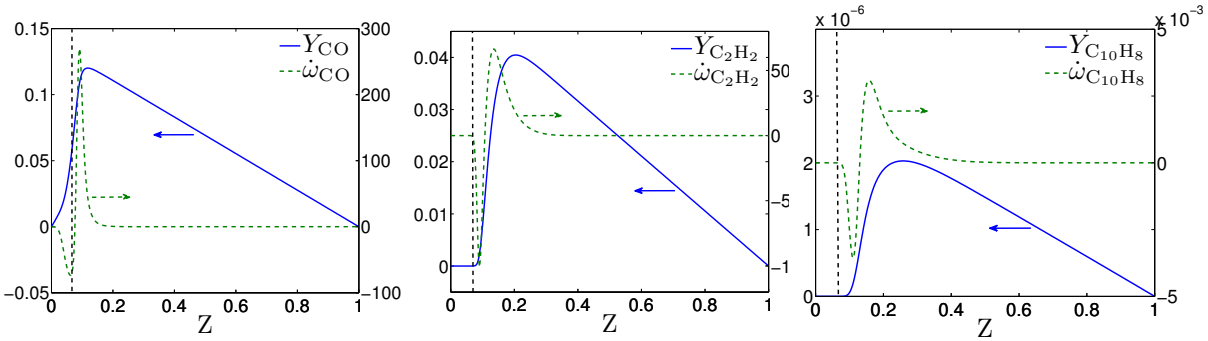

(a) CO. (b) C_2H_2. (c) $C_{10}H_8$.

Figure 5.3: Mass fraction and chemical source term profiles in mixture fraction space for three representative species in the steady-state flamelet with $\chi_{st} = 20s^{-1}$. The chemical source terms are plotted in $kg \cdot m^{-3}s^{-1}$. The vertical dashed line represents the location of the stoichiometric mixture fraction, $Z_{st} = 0.064$.

Before analyzing the unsteady response of the chemical source terms to variations in scalar dissipation rates, it is insightful to consider the steady-state solutions first. The mass fraction and

chemical source term profiles for three representative species (CO, C_2H_2, and $C_{10}H_8$) are shown in Fig. 5.3 for a steady-state flamelet at $\chi_{st} = 20s^{-1}$. Carbon monoxide, CO, is selected since it is one of the most important by-products. Acetylene, C_2H_2, is one of the most important PAH precursors and is characterized by a relatively fast chemistry. Finally, naphthalene, $C_{10}H_8$, is a representative PAH molecule with relatively slow chemistry.

For mixture fraction values below $Z_{st} = 0.064$, C_2H_2 and $C_{10}H_8$ are non-existing as they are oxidized before arriving at the flame front (strong negative source term at $Z \simeq 0.1$). The same oxidation is the major contribution to the chemical source term for CO. It is positive at $Z \simeq 0.1$ because of the oxidation of all hydrocarbons (HC) into CO; and it is negative at $Z = Z_{st}$ because of the conversion of CO to CO_2. For mixture fraction values beyond $Z > 0.4$, diffusion is the predominant process, since all three chemical source terms vanish. As a result, the mass fraction profiles are practically linearly dependent on Z. For all HC species, the chemical source terms leading to the formation of these species are important for the range of Z from the stoichiometric value to $Z \simeq 0.4$. Therefore, to investigate the effects of unsteady scalar dissipation rate on the formation of important intermediate species and PAH, the mixture fraction range of interest is $0.064 < Z < 0.4$.

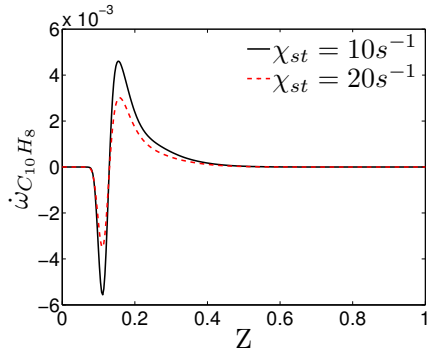

Figure 5.4: Chemical source term distribution of $C_{10}H_8$ in two steady-state flamelets. The chemical source terms are plotted in $kg \cdot m^{-3}s^{-1}$.

By comparing the distributions of the chemical source term of $C_{10}H_8$ for two different χ_{st} values (Fig. 5.4), it can be seen that the shape of the curves is preserved while the amplitude is changed. This was observed for most of the HC species over a wide range of χ_{st} values. Therefore, it is reasonable to assume that the evolution of the chemical source terms over all mixture fraction

values is well represented by the evolution at any single mixture fraction value. In the present work, the mixture fraction value at the peak of the chemical source term $Z_i = Z_{i,max}$ is selected, since we are interested in the chemistry-controlled relaxation. This choice is consistent with the intent of the current work being to investigate the interaction between turbulence and the formation of species governed by relatively slow chemistry. Choosing Z_i on the rich side ($Z > 0.4$) would give a diffusion-controlled relaxation characterized by a unique diffusion time scale ($\simeq \chi^{-1}$) since unity Lewis number transport is assumed for all species. The $Z_{i,max}$ values for the different species investigated are listed in Table. 5.1.

5.4.2 Initial evolution

In the following, we first investigate the very-early-time responses to the step changes in χ. The flamelet was at steady-state with initial scalar dissipation rate χ before the perturbation is applied. In other words, the mass fraction of species i was governed by the steady-state flamelet equation

$$-\frac{\chi}{2}\frac{\partial^2 {Y_i}^0}{\partial Z^2} = \frac{\dot{\omega}_i^0}{\rho}, \tag{5.17}$$

where ${Y_i}^0$ and $\dot{\omega}_i^0$ are the mass fraction and the chemical source term of species i at the initial steady-state. After perturbation, the scalar dissipation rate is changed to χ', with the relative change $\delta\chi = \chi' - \chi$. For a small amount of time ($\delta\tau$) after the perturbation, both species mass fraction and chemical source term have not had time to change and the evolution of the mass fraction of species i is governed by

$$\frac{\delta Y_i}{\delta\tau} = \frac{\delta\chi}{2}\frac{\partial^2 {Y_i}^0}{\partial Z^2} + \frac{\chi}{2}\frac{\partial^2 {Y_i}^0}{\partial Z^2} + \frac{\dot{\omega}_i^0}{\rho}, \tag{5.18}$$

where $\delta Y_i = Y_i - {Y_i}^0$ denotes the change in species mass fraction relative to its initial value. Using Eq. 5.17, the initial change in Y_i can be estimated to be

$$\delta Y_i = \delta\tau\frac{\delta\chi}{2}\frac{\partial^2 {Y_i}^0}{\partial Z^2} = -\delta\tau\frac{\delta\chi}{\chi}\frac{\dot{\omega}_i^0}{\rho}. \tag{5.19}$$

This expression could be used to predict the very early evolution of *any* species mass fractions. Interestingly, whether the species yield increases or decreases initially is governed by the signs of $\delta\chi$ and $\dot{\omega}_i^0$. More precisely, if the scalar dissipation rate is increased (by the step change), the mass fraction of species i would decrease if its source term were positive, since the locally enhanced diffusion removes more strongly the species. Similarly, the mass fraction of species i would increase if the source term were negative. In the above equations, $\delta\tau$ is a small time interval after the perturbation is applied. While it is beyond the scope of the current study to evaluate precisely this quantity *a priori*, it can be observed from the perturbed flamelet simulations (shown later in Fig. 5.5) that $\delta\tau$ is of the order of milliseconds.

To illustrate this, the time-evolution of the mass fraction Y_i at their corresponding Z_i for H, OH, CO, CO_2, and C_2H_2 are shown in Fig. 5.5, for a steady-state flamelet perturbed from its initial $\chi_{st} = 10s^{-1}$ to a final $\chi_{st} = 20s^{-1}$.

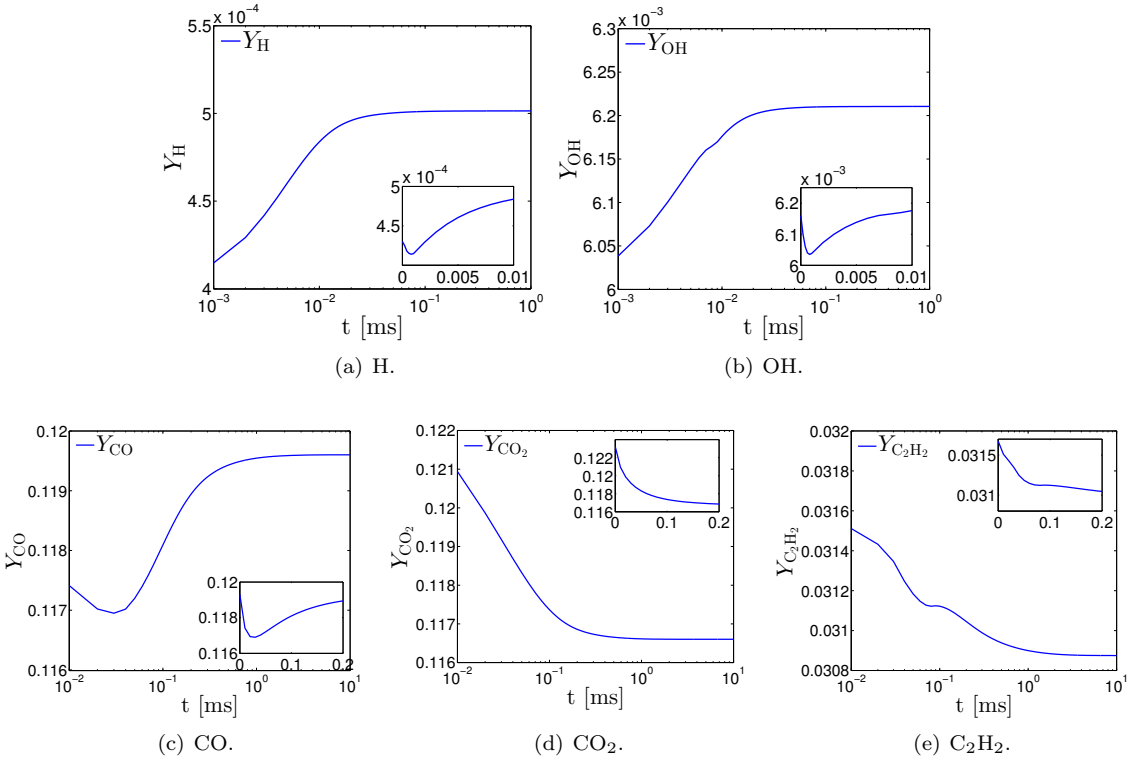

(a) H. (b) OH.

(c) CO. (d) CO_2. (e) C_2H_2.

Figure 5.5: Time-evolution of the mass fraction for several representative species for a flamelet perturbed from an initial $\chi_{st} = 10s^{-1}$ to a final $\chi_{st} = 20s^{-1}$. The chemical source terms are plotted in $kg \cdot m^{-3}s^{-1}$. The early evolutions are highlighted in the insets on a linear scale.

The initial changes are indeed observed for all species, and follow the analytical prediction given by Eq. 5.19 (each mass fraction decreases since its chemical source term is positive at $Z_{i,max}$). These initial changes take place very quickly, after which, both the species yield and its source term relax towards their new steady-state values. This relaxation is detailed in the following subsections.

5.4.3 Relaxation time scales

Before analyzing the results of the relaxation to the new steady-state, it is insightful to estimate *a priori* expected relaxation time scales (evaluated directly from the steady-state flamelet solutions). In the reaction zone, the rate of change of species mass fraction is primarily due to the chemical source term. Chemical time scales characterizing the relaxation of each species can be estimated as

$$\tau_i = \frac{\rho Y_{i,max}}{|\dot{\omega}_{i,max}|}, \tag{5.20}$$

where $Y_{i,max}$ and $\dot{\omega}_{i,max}$ represent the mass fraction and chemical source term of species i at the location $Z_{i,max}$ of maximum source term in the flamelet solution. Three time scales can be defined by choosing this chemical source term to be either the chemical production rate $\dot{\omega}_i^+$, chemical consumption rate $\dot{\omega}_i^-$, or the overall reaction rate for species i, $\dot{\omega}_i = \dot{\omega}_i^+ + \dot{\omega}_i^-$ [83]. Results for several species of interest are provided in Table 5.1 for the steady-state flamelet with $\chi_{st} = 20s^{-1}$. It is worth pointing out that these characteristic time scales were found to be almost invariant for steady-state flamelets over a wide range of stoichiometric scalar dissipation rates. After the initial changes described by Eq. 5.19, the mass fractions of the different species are expected to relax towards their new steady-state values over these characteristic time scales.

5.4.4 Relaxation of radicals and small species

As shown in Fig. 5.5, the mass fractions of radicals such as OH and H relax to their new steady-state values extremely fast (on the order of $10 - 20\mu s$). As expected, this relaxation occurs over time scales comparable to those listed in Table. 5.1. On the other hand, CO and CO_2 relax more slowly

	Radicals			Small species		
	OH	H	O	CO	CO_2	C_2H_2
Production	6.4	4.3	10.4	60.1	94.2	77.3
Consumption	11.9	3.8	7.3	152	67.3	40.1
Overall	13.8	32.7	24.5	67.1	82.5	83.3
$Z_{i,max}$	0.06	0.07	0.06	0.11	0.063	0.135
	Aromatic species			Aromatic radicals		
	C_6H_6	$C_{10}H_8$	$C_{14}H_{10}$	C_6H_5	$C_{10}H_7$	$C_{14}H_9$
Production	166	222	328	3.2	2.9	3.4
Consumption	287	397	537	2.8	2.7	3.3
Overall	411	506	840	32.4	38.6	35.2
$Z_{i,max}$	0.19	0.155	0.146	0.19	0.155	0.146

Table 5.1: Characteristic time scales and locations of maximum source term (in mixture fraction space) for several representative species for the steady-state flamelet solution with $\chi_{st} = 20s^{-1}$. Units are microseconds.

compared to OH and H (on the order of $100 - 200\mu s$). Nevertheless, the relaxation of CO and CO_2 still occurs fast and over their corresponding time scales given in Table. 5.1. For C_2H_2, its mass fraction also relaxes to the new steady-state within around $100\mu s$. Once again, this result is consistent with the estimates for the relaxation time scales shown in Table. 5.1.

Therefore, given these small relaxation time scales, a relaxation model may not be necessary, and the mass fractions can be pre-tabulated using steady-state flamelet solutions. In other words, Method I can be used legibly for species such as CO,CO_2, and C_2H_2.

5.4.5 Relaxation of aromatic species

The relaxation towards the new steady-state is more complex for aromatic species. The differences in time scale, as shown in Table. 5.1, suggest that aromatic species have different relaxation behaviors from small species. In the following, the time evolutions of the mass fraction and chemical source term are shown for several selected species as illustration, based on which the relaxation behaviors are described and explained without loss of generality.

The time evolutions of the mass fraction and chemical source terms for C_6H_6, $C_{10}H_8$, and $C_{14}H_{10}$ are shown in Fig. 5.6 from the same calculation of the same perturbed flamelet. Using $C_{10}H_8$ as an example, the general picture of the evolution of a PAH species may be drawn.

From a reaction flux analysis, the main production reactions for $C_{10}H_8$ have been identified to

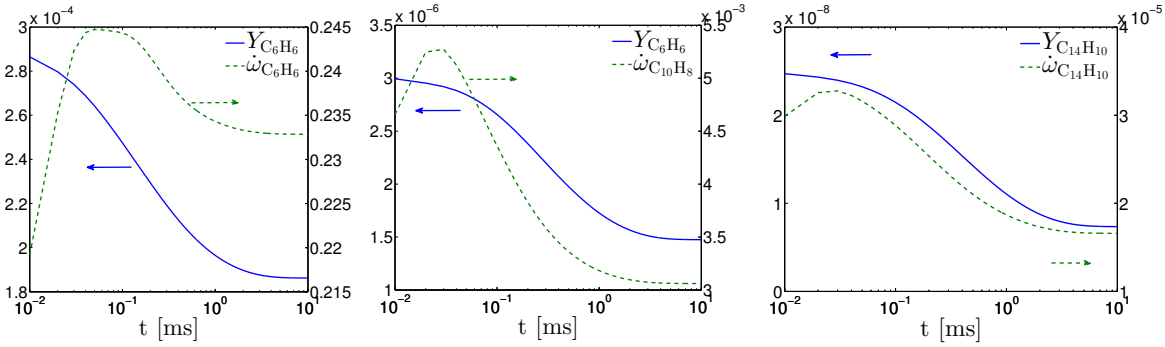

(a) C_6H_6. (b) $C_{10}H_8$. (c) $C_{14}H_{10}$.

Figure 5.6: Time-evolution of the mass fraction and the chemical source term for several representative aromatic species. The chemical source terms are plotted in $kg \cdot m^{-3}s^{-1}$.

be

$$C_8H_5 + C_2H_4 \rightleftharpoons C_{10}H_8 + H, \tag{5.21}$$

and

$$C_8H_5 + C_2H_2 \rightleftharpoons C_{10}H_7, \tag{5.22}$$

followed by the fast recombination

$$C_{10}H_7 + H \rightleftharpoons C_{10}H_8. \tag{5.23}$$

The main consumption reaction is

$$C_{10}H_8 + H \rightleftharpoons C_{10}H_7 + H_2. \tag{5.24}$$

Therefore, the chemical production rate (positive) for $C_{10}H_8$ is primarily controlled by

$$\dot{\omega}^+_{C_{10}H_8} \propto Y_{C_8H_5}, \tag{5.25}$$

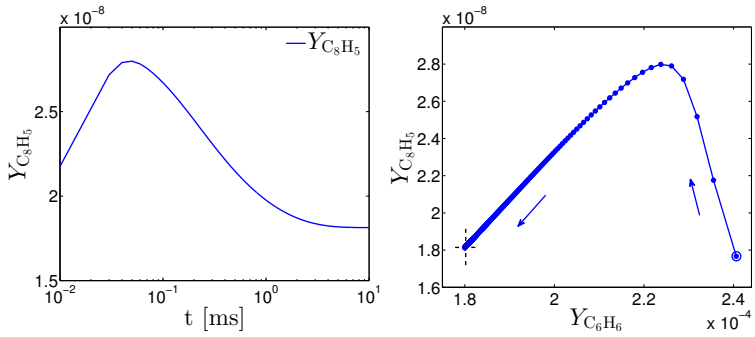

(a) Time evolution. (b) C_8H_5 *vs.* C_6H_6.

Figure 5.7: Time-evolution of C_8H_5 and dependence of its mass fraction on the mass fraction of C_6H_6 during the relaxation of a flamelet perturbed from an initial $\chi_{st} = 10s^{-1}$ to a final $\chi_{st} = 20s^{-1}$. In (b), the initial steady-state is circled. The final steady-state is indicated by the dashed horizontal and vertical lines. The arrows indicate the paths that unsteady solutions follow as time increases.

and the chemical consumption rate (negative) is controlled by

$$\dot{\omega}^{-}_{C_{10}H_8} \propto Y_{C_{10}H_8}. \tag{5.26}$$

The evolution of this aromatic species can be generally depicted as follows. As the scalar dissipation rate increases, the chemical source term first increases. There are two ways to increase the intensity of the chemical source term: first, by reducing the magnitude of the consumption rate; and second, by increasing the production rate. As mentioned before (Section 5.4.2), due to a positive chemical source term at $Z_{C_{10}H_8,\max} = 0.155$, $Y_{C_{10}H_8}$ decreases initially (as seen in Fig. 5.6(b)) which tends to reduce the magnitude of the consumption rate (Eq. 5.26). Simultaneously, at the location where the source term of $C_{10}H_8$ is maximum ($Z_{C_{10}H_8,\max}$), the source terms for radicals leading to its formation (namely C_8H_5) are negative. According to Eq. 5.19, more C_8H_5 are created initially (Fig. 5.7(a)) which increases the production rate of $C_{10}H_8$. The combined effects of a reduced consumption rate and increased production rate lead to an increase of the overall rate. This behavior is observed for the first $30\mu s$, namely a decrease in the species mass fraction and an increase in its overall chemical source term. The same behavior is observed for all aromatic species.

After $30\mu s$, the evolution of $C_{10}H_8$ changes to a different regime. Radicals such as C_8H_5 do not increase any more and in fact start to decrease (Fig. 5.7(a)). This behavior is the result of

the chemical time scales listed in Table. 5.1. The production and consumption time scales are extremely small ($\simeq 3\mu s$). Very rapidly ($\simeq 30\mu s$), these radicals are in quasi-steady-state with their corresponding stable molecules. This temporal delay is due to the necessary time for the small radicals H, O, and OH (Fig. 5.5) to relax towards their new steady-state. As a result after $30\mu s$, the aromatic radicals are in quasi-steady-states and they start to follow the evolution of their corresponding stable molecules (for instance, the stable molecule corresponding to C_8H_5 is C_6H_6). This is illustrated in Fig. 5.7(b) with a linear dependence of $Y_{C_8H_5}$ on $Y_{C_6H_6}$

$$Y_{C_8H_5} \propto Y_{C_6H_6}. \tag{5.27}$$

Since the mass fractions of the stable molecules (C_6H_6) keep decreasing (Fig. 5.6), the mass fractions of the related radicals (C_8H_5) decrease as well, resulting in a reduced production rate (for $C_{10}H_8$). In other words,

$$\dot{\omega}^{+}_{C_{10}H_8} \propto Y_{C_6H_6}, \tag{5.28}$$

by combining Eq. 5.25 and Eq. 5.27. On the other hand, the consumption rate of $C_{10}H_8$ is still linearly proportional to its mass fraction (Eq. 5.26), and keeps decreasing. The combined effects of the production and consumption rates lead to a decrease of the overall reaction rate.

It is clear that the mass fractions of these species cannot be pre-tabulated using steady-state flamelet solutions, since substantial and non-trivial transient effects are observed. In fact, none of the models presented in Section 5.2.3 can be used for PAH species such as $C_{10}H_8$.

5.5 PAH relaxation model

A new linear relaxation model is proposed based on previous discussions. One-dimensional flamelet calculations are performed using the proposed model and compared to models previously developed and employed in numerical simulations of turbulent non-premixed flames [8, 22].

5.5.1 Previous one-step relaxation model

A linear relaxation model was proposed previously for NO_x species [8, 87], and recently used in the simulation of turbulent non-premixed flames for PAH [22]. This model was developed by considering a one-step reversible reaction of type

$$R_1 + R_2 \leftrightharpoons S + P, \tag{5.29}$$

where R_1 and R_2 are two representative reactants, P is a product species, and S is the species of interest. Assuming that all other species are in steady-state, the chemical production rate of species S is a constant ($\dot{\omega}_S^+ = const$), and the chemical consumption rate is linearly dependent on the mass fraction of S ($\dot{\omega}_S^- \propto Y_S$). Therefore, $\dot{\omega}_{S+}$ and $\frac{\dot{\omega}_{S-}}{Y_S}$ can be tabulated *a priori* into a flamelet library using only steady-state flamelet solutions. In other words,

$$\dot{\omega}_S = \left(\frac{\dot{\omega}_S^-}{Y_S}\right)(Z, \chi'_{st}) \cdot Y_S + \dot{\omega}_S^+(Z, \chi'_{st}). \tag{5.30}$$

Although this model is suitable for NO_x [8], it is not adequate for PAH as shown in the previous section. Large PAH are formed from smaller aromatic species, which themselves exhibit substantial transient effects. Therefore, assuming these species to be in steady-state is not appropriate. As a result, the chemical production of a PAH species can not be assumed to be constant at a given mixture fraction and scalar dissipation rate (Z, χ).

5.5.2 Proposed multi-step model

Based on the above considerations, a new linear relaxation model is proposed for PAH based on the following series of one-step reactions

$$\begin{aligned} A_{n-1} + R_1 &\rightarrow A_n + P_1, \\ A_n + R_2 &\rightarrow P_2 + P_3. \end{aligned} \tag{5.31}$$

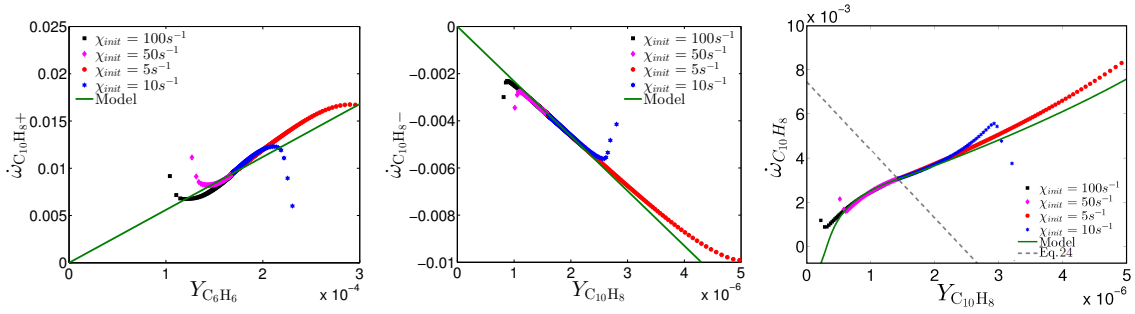

(a) Production rate. (b) Consumption rate. (c) Overall reaction rate.

Figure 5.8: Modeled chemical production, consumption rates, and overall reaction rates compared to unsteady calculations with full chemistry for $C_{10}H_8$. The chemical source terms are plotted in $kg \cdot m^{-3}s^{-1}$.

where a PAH molecule A_{n-1} with $n-1$ aromatic rings and R_1 react to form a larger PAH molecule A_n and a product P_1, and A_n is consumed by reacting with another species R_2 to form products P_2 and P_3. The intent of the representative production reaction is to *lump* all reactions leading to the formation of A_n from A_{n-1}. Similarly, all reactions leading to the consumption of A_n are lumped in to the representative consumption reaction. It is worth pointing out that the representative consumption reaction for A_n may not correspond directly to the formation of A_{n+1}, since the main products of this reaction are commonly a radical associated with A_n and a small species characterized by fast chemistry.

Assuming that all other species except PAH relax within relatively short time scales, their mass fractions can be represented by the corresponding steady-state values. As such, the production rate for A_n is proportional to the yield of A_{n-1} and its consumption rate is proportional to its own mass fraction. Practically, the modeled PAH chemical source term can be written as

$$\dot{\omega}_{A_n} = a\left(Z, \chi'\right) \cdot Y_{A_{n-1}} + b\left(Z, \chi'\right) \cdot Y_{A_n}. \tag{5.32}$$

The coefficients a and b can be tabulated solely using steady-state flamelets by dividing the production and consumption rates of A_n by the mass fraction of A_{n-1} and A_n respectively.

The proposed model for PAH source terms is consistent with the general picture of relaxation for PAH species described in the previous section. Small radicals relax extremely fast, which makes the

consumption rate of A_n proportional to its own mass fraction. The production rate of A_n has been identified to be proportional to radicals associated with A_{n-1}. The mass fraction of these radicals becomes proportional to the stable molecule A_{n-1} after a short period of time ($\simeq 30\mu s$) due to the small chemical time scales (Table. 5.1). Therefore, it is reasonable to model the production rate of A_n to be proportional to the yield of A_{n-1}.

To further justify the proposed model, the modeled production and consumption rates (Eq. 5.32) for $C_{10}H_8$ are compared against the exact rates obtained from the unsteady calculations for the flamelets perturbed from various initial χ_{st} values to $\chi_{st} = 20s^{-1}$. As shown in Fig. 5.8(a,b), the production and consumption rates are both reasonably well captured by the relaxation model based on the representative reactions (Eq. 5.31). Furthermore, the model performs equally well for both smaller and larger initial χ_{st} as well as small and large fluctuations in χ_{st}. Fig. 5.8 shows a comparison of the exact overall reaction rate on the species mass fraction against that predicted with the current model. For comparison, the linear relation determined by Eq. 5.30 is also plotted in Fig. 5.8(c) for $C_{10}H_8$ for the same perturbed flamelets. It can be seen that the form of chemical source is not well captured by the previous one-step relaxation model (Eq. 5.30), which assumes that the production rate is constant and independent of species yield.

5.5.3 Discussion

In the following, we discuss a few key aspects of the proposed relaxation model. First, instead of evaluating the source terms using Eq. 5.32, the modeled source term for PAH (green curve in Fig. 5.8(c)) could be entirely tabulated as a function of $Y_{C_{10}H_8}$. However, this method may become computationally more expensive, and the insight into the major chemical pathways leading to the formation and consumption of PAH will be lost. Therefore, the proposed relaxation model (Eq. 5.32) is more advantageous.

Second, the proposed relaxation method remains valid as long as turbulent effects occur over a time scale greater than $30\mu s$ (characteristic chemical time scales for radicals). Under this condition, transient effects of radicals and small species do not need to be considered. This assumption repre-

sents the same level of approximation as considering small radicals and major species to follow the steady-state flamelet solutions, which is found to be valid in practical circumstances [63, 145, 146].

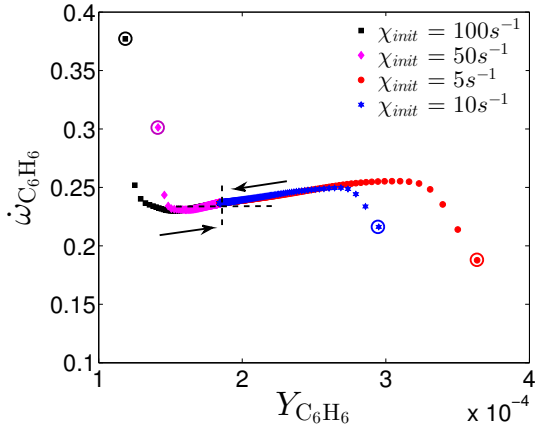

Figure 5.9: Dependence of the chemical source term of C_6H_6 on its mass fraction during the relaxation from steady-state flamelets (with various initial χ_{st}) to the final steady-state (with $\chi'_{st} = 20$) at $Z_{\mathrm{C6H6,max}} = 0.19$. The chemical source terms are plotted in $kg \cdot m^{-3}s^{-1}$. The initial steady-states are circled. The final steady-state is indicated by the dashed horizontal and vertical lines. The arrows indicate the paths that unsteady solutions follow as time increases.

Third, it is worth pointing out that the source term of C_6H_6 relaxes to the final steady-state value faster than its mass fraction (Fig. 5.6(a)), since the radicals leading to the formation of benzene relax to the new steady-state relatively fast. The variation of the source term ($\dot{\omega}_{C_6H_6}$) is within less than 10% of its final steady-state value (except for the very early stage of the relaxation process), as shown in Fig. 5.9. Therefore, the chemical source term of benzene could be treated as independent of its mass fraction and legibly tabulated based on steady-state flamelets (Method II for chemistry tabulation). As such, benzene is the first aromatic species for which unsteady effects should be considered. For aromatic molecules beyond benzene, the model represented by Eq. 5.32 should be used.

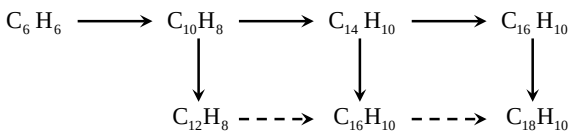

Figure 5.10: Diagram of reactions leading to the formation of PAH species.

PAH species include a lot more species than those discussed so far. PAH species such as ace-

naphthylene ($C_{12}H_8$), acephenanthrene ($C_{16}H_{10}$), and acepyrene ($C_{18}H_{10}$) were not considered in the current model. The formation of these PAH could be generally depicted in the representative graph, as shown in Fig. 5.10. The mechanism used in the present work does include these species and predicts that these species are mainly formed from their corresponding PAH without the five-membered ring (*e.g.* $C_{16}H_{10}$ is mainly formed from $C_{14}H_{10}$). Unfortunately, as the chemical compounds get larger, less is known on the major pathways controlling their chemistry. Extending the relaxation model to include PAH species listed above is possible but its final accuracy would be strongly dependent upon the accuracy of the detailed chemical model used. It is also beyond the scope of the current work.

Finally, the proposed relaxation model can be easily extended to turbulent calculations and would only be slightly more expensive than traditional chemistry tabulation methods without a relaxation model. In addition, the coefficients in the model, namely $a(Z,\chi)$ and $b(Z,\chi)$ in Eq. 5.32, can be fully tabulated with steady-state flamelets, and looked up using the local, instantaneous χ values. The proposed relaxation model is also advantageous for integration into Large-Eddy Simulations (LES) since the linearity of the model makes its future application to LES easier.

5.5.4 Validation

The unsteady flamelet equations are solved for benzene (C_6H_6), and naphthalene ($C_{10}H_8$) with the respective forms of the chemical source term tabulated using the proposed relaxation model. As for the analysis presented in Section 4, the flamelet considered has the initial $\chi_{st} = 10s^{-1}$, and is perturbed to $\chi'_{st} = 20s^{-1}$. The mass fraction profiles and time-evolutions are compared against those calculated from the same unsteady flamelet equations with the full detailed chemical mechanism for benzene and naphthalene in Fig. 5.11 and 5.12. Finally, for comparison, unsteady flamelet equations are also solved using the previously-suggested relaxation model [8] represented by Eq. 5.30.

Intermediate solutions of the unsteady flamelet equations obtained using the proposed relaxation model (Eq. 5.32) show satisfactory agreement with the detailed chemistry results for both species, whereas results obtained using the relaxation model of Eq. 5.30 show relatively large deviation.

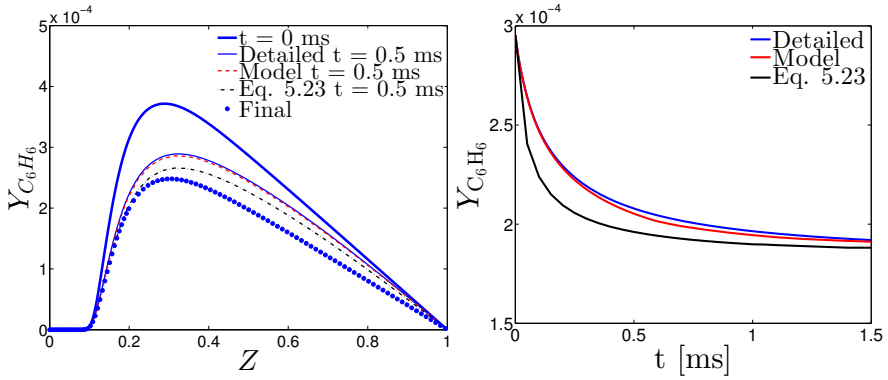

(a) Intermediate solutions. (b) Time-evolution at $Z_{C_6H_6,max} = 0.19$.

Figure 5.11: Comparison of the time evolution of benzene mass fractions resulting from the detailed chemistry mechanism and the relaxation models.

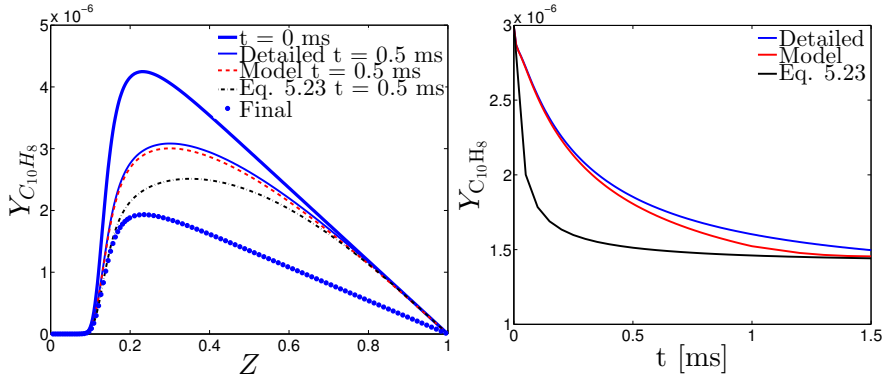

(a) Intermediate solutions. (b) Time-evolution at $Z_{C_{10}H_8,max} = 0.155$.

Figure 5.12: Comparison of the time evolution of naphthalene mass fractions resulting from the detailed chemistry mechanism and the relaxation models.

These *a posteriori* results are not surprising as Eq. 5.32 captures the correct dependence of the chemical source terms on the various species mass fractions, and the unsteady evolution of the chemical production terms of PAH species cannot be neglected.

After validating the current relaxation model for PAH species, the next step is to apply this model to the numerical simulation of a turbulent sooting flame, to investigate the effects of non-equilibrium aromatic chemistry.

Chapter 6

Effects of aromatic chemistry-turbulence interactions on soot formation in a turbulent non-premixed flame

The objective of this work is to investigate the effects of the aromatic chemistry-turbulence interactions on the formation and later evolution of Polycyclic Aromatic Hydrocarbons (PAH) and soot, using the relaxation model proposed in the previous chapter. These effects are investigated in a well-documented, piloted turbulent sooting jet flame, for its relevance to gas turbine engine combustion environment and for the available measurements on soot quantities that are characterized potentially by non-equilibrium aromatic chemistry [94]. The study of such a configuration allows the examination of the effects of aromatic chemistry-turbulence interactions on the inception, growth, and oxidation of PAH species and soot particles. Due to the extremely high computational cost associated with the direct simulation of such a configuration, as mentioned in Chapter. 1, Large-Eddy Simulations (LES) are performed. Particular attention is paid to the inception locations, magnitude and fluctuations of aromatic species and soot. This chapter is organized as follows. Section 1 describes the models used for soot transport, gas-phase combustion, radiation, LES closure, and PAH relaxation. In Section 2 and 3, the presented models are applied to the LES of an ethylene/air piloted turbulent sooting non-premixed jet flame.

6.1 Numerical algorithms

The proposed simulation framework relies on five major components: a soot model, a gas-phase chemistry model, a radiation model, a turbulence closure model, and finally a relaxation model for PAH species.

6.1.1 Soot model

In the present study, the geometry of a fractal soot aggregate is described using a bi-variate representation based on its total volume V and total surface area S [115, 147]. Accordingly, the number of primary particles per aggregate (n_p) and the diameter of the primary particles d_p can be expressed as [115]

$$n_p = \frac{1}{36\pi} V^{-2} S^3, \text{ and } d_p = 6VS^{-1}. \tag{6.1}$$

The evolution of soot particles is described, from a statistical point of view, by solving the transport equations for several key moments,

$$M_{x,y} = \iint n(V,S) V^x S^y \mathrm{d}V \mathrm{d}S, \tag{6.2}$$

of the soot Number Density Function (NDF) $n(V,S)$. Their transport equations, derived from the population balance equation of the soot NDF, are [114]

$$\frac{\partial M_{x,y}}{\partial t} + \nabla \cdot (\mathbf{u^*} M_{x,y}) = \dot{\omega}_{x,y}, \tag{6.3}$$

where

$$\mathbf{u^*} = \mathbf{u} - 0.556 \frac{\nu}{T} \nabla T \tag{6.4}$$

is the velocity vector accounting for thermophoresis effects [42, 22], ν is fluid kinematic viscosity, and $\dot{\omega}_{x,y}$ accounts for the nucleation, surface growth, coagulation, condensation, and oxidation of soot particles [114]. The soot NDF is approximated using two delta functions. The first delta function

is intended to capture the population of small, young soot particles, and the second delta function corresponds to the population of large, mature soot particles. Four soot moments are tracked in the numerical simulations, and the source terms $\dot{\omega}_{x,y}$ are closed using the Direct Quadrature Method of Moments (DQMOM) [115] to capture the multi-modal nature of the soot NDF [148, 149]. Details of the form of the different source terms and their closure can be found in [22, 114, 115].

6.1.2 Gas-phase chemistry model

Using the definition of the mixture fraction, Z, the local thermochemical state in the mixture is described using the Flamelet/Progress Variable (FPV) model proposed by Pierce and Moin [59, 22, 150]. This model predicts that all thermochemical quantities ϕ (temperature, species mass fractions, etc.) can be parametrized by the mixture fraction Z and a reaction progress variable C

$$\phi = \mathfrak{H}\left(Z, C\right). \tag{6.5}$$

The functional dependence $\mathfrak{H}$ is determined by the solutions of the following steady-state flamelet equations, in which species transport is assumed to be described by a unity Lewis number (see Section 5.1)

$$-\frac{1}{2}\chi\frac{\partial^2\phi}{\partial Z^2} = \frac{\dot{\omega}_\phi}{\rho}, \tag{6.6}$$

where $\dot{\omega}_\phi$ includes the chemical source term of the thermochemical quantity ϕ. Species source terms, mass fractions, and other thermochemical quantities are pre-computed and stored in to a flamelet library.

For the prediction of turbulent reacting flows where local extinction and re-ignition processes are present, the stable, unstable, and unburnt branches of the flamelet solutions in a S-Shaped curve have to be all included [8, 22, 150]. Therefore, a reaction progress variable, C, is required in the FPV model to overcome the ambiguity in the description of the of the steady-state flamelet solutions using the scalar dissipation rate, χ [8]. In the following , this progress variable is defined as a linear

combination of the mass fractions of the major products [150]

$$C = Y_{CO_2} + Y_{CO} + Y_{H_2O} + Y_{H_2}. \tag{6.7}$$

Assuming that the transport of all species is described using a unity Lewis number, the evolution of the progress variable can be derived from the transport equations of the individuals species included in the definition of C

$$\frac{\partial \rho C}{\partial t} + \nabla \cdot (\rho C \mathbf{u}) = \nabla \cdot (\rho D \nabla C) + \dot{\omega}_C, \tag{6.8}$$

where $\dot{\omega}_C = \dot{\omega}_{CO_2} + \dot{\omega}_{CO} + \dot{\omega}_{H_2O} + \dot{\omega}_{H_2}$ [8, 15, 22]. Further details of the FPV approach can be obtained from [8, 59, 22, 150, 26].

6.1.3 Radiation model

Radiative heat transfer from gas-phase species and soot particles was found to have a significant influence on flame structure, species profiles and soot emissions [8, 139, 151, 152, 153]. The RADCAL model [92] is used for gas-phase radiation. Under the optically thin assumptions, the radiative heat loss rate per unit volume is calculated following Eq. 2.5.

For soot radiation, the radiative heat losses of soot aggregates, $\dot{q}_{soot}$, can be calculated by considering the broadband integrated soot radiative intensity, e. This intensity can be calculated as [154]

$$e(T) = 4\pi \int_0^\infty \frac{K_e f_v}{\lambda} \cdot I(\lambda, T) \cdot d\lambda, \tag{6.9}$$

where K_e is the dimensionless extinction coefficient, f_v is the local soot volume fraction, λ is the wavelength of the electromagnetic radiation, and $I(\lambda, T)$ indicates the black-body emission following Plank's law

$$I(\lambda, T) = \frac{2hc^2}{\lambda^5} \frac{1}{e^{\frac{hc}{\lambda k T}} - 1}. \tag{6.10}$$

In the above equation, h, c, and k are the Plank constant, the speed of light, and the Boltzmann constant, respectively. Recent experimental measurements suggest that the extinction coefficient

is nearly a constant $K_e \simeq 7.0$ [154]. Accordingly, the broadband emissivity, a, for soot radiation, defined as

$$e(T) = 4a\sigma f_v T^4, \tag{6.11}$$

can be well represented by the following function

$$a \simeq 1862T. \tag{6.12}$$

This approximation for emissivity is preferred over others [151, 155, 156] since it represents a better asymptotic behavior around $T = 1700K$, at which soot particles are generally formed [154, 157]. These expressions (Eqs. 6.11 and 6.12) are used for soot radiation in the LES of the piloted ethylene/air turbulent jet flame.

A new quasi-steady-state flamelet-based radiation model has been developed to take into account the effects of radiative heat losses due to gas-phase and soot radiation [158]. An enthalpy defect parameter,

$$H = H_{rad} - H_{ad}, \tag{6.13}$$

is introduced in the flamelet library as a measure of the departure of radiating flamelet solutions from non-radiating flamelet solutions. In the above equation, H_{rad} denotes the enthalpy of the radiating gas-phase mixture, and H_{ad} denotes the enthalpy of the adiabatic gas-phase mixture. As such, radiative heat losses can be consistently taken into account using the steady-state flamelet formulation by solving the following equation for the enthalpy defect parameter, H,

$$-\frac{\rho\chi}{2}\frac{\partial^2 H}{\partial Z^2} = \dot{\omega}_H - r(\dot{q}_{rad} + \dot{q}_{soot}), \tag{6.14}$$

where r is a radiation intensity parameter ranging from 0 to 1. Accordingly, the FPV model accounting for radiative heat losses can be extended from Eq. 6.5 as

$$\phi = \mathfrak{F}\left(Z, C, H\right), \tag{6.15}$$

where the different thermochemical quantities are mapped in the three-dimensional manifold mapped by Z, C, and H [26, 158].

In physical space, assuming unity Lewis number for all species, constant pressure, and negligible heating due to viscous dissipation, a transport equation can be derived for the enthalpy defect parameter

$$\frac{\partial \rho H}{\partial t} + \nabla \cdot (\rho H \mathbf{u}) = \nabla \cdot (\rho D \nabla H) - \dot{q}_{rad} - \dot{q}_{soot}. \tag{6.16}$$

6.1.4 LES closure

6.1.4.1 Transport equations

In this LES, the continuity and momentum equations are filtered spatially and solved

$$\frac{\partial \overline{\rho}}{\partial t} + \nabla \cdot (\overline{\rho}\widetilde{\mathbf{u}}) = 0, \tag{6.17}$$

$$\frac{\partial \overline{\rho}\widetilde{\mathbf{u}}}{\partial t} + \nabla \cdot (\overline{\rho}\widetilde{\mathbf{u}}\widetilde{\mathbf{u}}) = -\nabla \overline{p} + \nabla \cdot (\overline{\rho}\widetilde{\mathbf{u}}\widetilde{\mathbf{u}} - \overline{\rho}\widetilde{\mathbf{u}\mathbf{u}}) + \nabla \cdot \overline{\tau}. \tag{6.18}$$

In physical space, the spatially filtered transport equations for the soot moments, mixture fraction, progress variable, and enthalpy defect (Eqs. 6.3, 2.6, 6.8, and 6.16) are solved

$$\frac{\overline{M_{x,y}}}{\partial t} + \nabla \cdot (\widetilde{\mathbf{u}^*\overline{M_{x,y}}}) = \nabla \cdot (\widetilde{\mathbf{u}^*\overline{M_{x,y}}} - \overline{\mathbf{u}^*M_{x,y}}) + \overline{\dot{\omega}}_{x,y}, \tag{6.19}$$

$$\frac{\partial \overline{\rho}\widetilde{Z}}{\partial t} + \nabla \cdot (\overline{\rho}\widetilde{Z}\widetilde{\mathbf{u}}) = \nabla \cdot (\overline{\rho}\widetilde{Z}\widetilde{\mathbf{u}} - \overline{\rho}\widetilde{Z\mathbf{u}}) + \nabla \cdot (\overline{\rho}\widetilde{D}\nabla\widetilde{Z}), \tag{6.20}$$

$$\frac{\partial \overline{\rho}\widetilde{C}}{\partial t} + \nabla \cdot (\overline{\rho}\widetilde{C}\widetilde{\mathbf{u}}) = \nabla \cdot (\overline{\rho}\widetilde{C}\widetilde{\mathbf{u}} - \overline{\rho}\widetilde{C\mathbf{u}}) + \nabla \cdot (\overline{\rho}\widetilde{D}\nabla\widetilde{C}) + \overline{\dot{\omega}}_C, \tag{6.21}$$

$$\frac{\partial \overline{\rho}\widetilde{H}}{\partial t} + \nabla \cdot (\overline{\rho}\widetilde{H}\widetilde{\mathbf{u}}) = \nabla \cdot (\overline{\rho}\widetilde{H}\widetilde{\mathbf{u}} - \overline{\rho}\widetilde{H\mathbf{u}}) + \nabla \cdot (\overline{\rho}\widetilde{D}\nabla\widetilde{H}) - \overline{\dot{q}}_{rad} - \overline{\dot{q}}_{soot}. \tag{6.22}$$

The modeling of the unclosed terms is detailed below.

6.1.4.2 subfilter modeling

In these filtered equations, all subfilter stresses are closed using a dynamic Smagorinsky model [11, 12, 13]. This model is based on an artificial eddy viscosity approach, where the effects of turbulence

are lumped into a turbulent viscosity. The approach treats dissipation of kinetic energy at subgrid scales as analogous to molecular diffusion. The dynamic Smagorinsky model expresses the subfiler stresses (residual stresses) as

$$\tau_{ij}^r - \frac{1}{3}\tau_{i,j}^r \delta_{ij} = -2\nu_t \widetilde{S_{ij}}, \tag{6.23}$$

where ν_t is the turbulent eddy viscosity and

$$\widetilde{S_{ij}} = \frac{1}{2}\left(\frac{\partial \widetilde{u_i}}{\partial x_j} + \frac{\partial \widetilde{u_j}}{\partial x_i}\right) \tag{6.24}$$

is the rate-of-strain tensor. In the static Smagorinsky model, the turbulent eddy viscosity is modeled as

$$\nu_t = (C_s\Delta)^2\sqrt{2\widetilde{S_{ij}}\widetilde{S_{ij}}} = (C_s\Delta)^2\left|\widetilde{S}\right|, \tag{6.25}$$

where Δ is the filter width (practically the grid size), C_s is a constant, and $\widetilde{S} = \sqrt{2\widetilde{S_{ij}}\widetilde{S_{ij}}}$. In the dynamic Smagorinsky model, the constant C_s is determined using a dynamic procedure by applying a second filtering operation $\hat{}$, usually referred to as test filtering, with filter width $\hat{\Delta}$ larger than the grid size Δ. The constant C_s is calculated as

$$C_s^2 = \frac{\mathcal{L}_{ij}\mathcal{M}_{ij}}{\mathcal{M}_{ij}\mathcal{M}_{ij}} \tag{6.26}$$

where

$$\mathcal{M}_{ij} = 2\Delta^2\left(\widehat{\left|\widetilde{S}\right|\widetilde{S_{ij}}} - \alpha^2\left|\widehat{\widetilde{S}}\right|\widehat{\widetilde{S}}_{ij}\right), \tag{6.27}$$

and

$$\mathcal{L}_{ij} = \widehat{\widetilde{u_i}\widetilde{u_j}} - \hat{\widetilde{u}}_i\hat{\widetilde{u}}_j, \tag{6.28}$$

where $\alpha = \hat{\Delta}/\Delta$,

As written, this procedure has been found numerically unstable since the numerator could become negative, and large fluctuations in C_s were often observed [11, 12, 13]. Hence, additional averaging

is often employed, leading to:

$$C_s^2 = \frac{\langle \mathcal{L}_{ij}\mathcal{M}_{ij} \rangle}{\langle \mathcal{M}_{ij}\mathcal{M}_{ij} \rangle} \tag{6.29}$$

In the current study, this averaging is applied over time following Lagrangian fluid trajectories [159, 160]. In practice, the Lagrangian-averaged value of a dummy variable, φ, at time t and location $x\,(t)$ is calculated discretely as

$$\langle \varphi \rangle\,(t, x\,(t)) = \omega \varphi\,(t, x\,(t)) + (1-\omega)\,\varphi\,(t - \Delta t, x\,(t - \Delta t))\,, \tag{6.30}$$

where Δt is the time step size, and ω is a weighting function defined as

$$\omega = \frac{\frac{2\Delta t \cdot \zeta^{\frac{1}{8}}}{3 \cdot \Delta}}{1 + \frac{2\Delta t \cdot \zeta^{\frac{1}{8}}}{3 \cdot \Delta}}. \tag{6.31}$$

In the above equation,

$$\zeta = \langle \mathcal{L}_{ij}\mathcal{M}_{ij} \rangle \langle \mathcal{M}_{ij}\mathcal{M}_{ij} \rangle\,. \tag{6.32}$$

In Eq. 6.19, the portion of the soot moment source terms which is a function of the thermochemical state of the gas is tabulated as any other gas quantities (Eq. 6.38). The other portion in the soot moment source terms is treated using laminar closure. Similarly to the residual stresses, all subfilter scalar fluxes in the above equations are closed using a dynamic Smagorinsky model [11, 12, 13] with Lagrangian averaging techniques [159, 160].

6.1.4.3 Equation of state

The Favre-filtered thermochemical quantities,

$$\widetilde{\phi} = \frac{\overline{\rho\phi}}{\overline{\rho}}, \tag{6.33}$$

are obtained from the equation of state (Eq. 6.15) by convolution with a joint subfilter Probability Density Function (PDF) $\widetilde{P}$

$$\widetilde{\phi}\left(Z,C,H\right)=\int\int\mathfrak{F}\left(Z,C,H\right)\widetilde{P}\left(Z,C,H\right)dZdCdH. \tag{6.34}$$

By introducing the mixture-fraction-independent parameters $\Lambda = C|Z_{st}$ and $\Xi = H|Z_{st}$, each solution to the steady-state flamelet equations can be uniquely identified [8], leading to

$$\phi=\mathfrak{F}\left(Z,C,H\right)=\mathfrak{G}\left(Z,\Lambda,\Xi\right). \tag{6.35}$$

The independence of Λ and Ξ on Z by definition ensures that the marginal distributions for the mixture fraction, progress variable, and enthalpy defect can be modeled separately. In the current work, the subfilter PDF is presumed to have the form [8, 131, 161, 162]

$$\widetilde{P}\left(Z,C,H\right)=\widetilde{P}\left(Z,\Lambda,\Xi\right)=\beta\left(Z;\widetilde{Z},\widetilde{Z''^2}\right)\delta\left(\Lambda-\widetilde{\Lambda}\right)\delta\left(\Xi-\widetilde{\Xi}\right), \tag{6.36}$$

where β represents a beta distribution and δ denotes a Dirac distribution. Using this presumed PDF, the filtered thermochemical state can be represented as

$$\widetilde{\phi}=\widetilde{\mathfrak{G}}\left(\widetilde{Z},\widetilde{Z''^2},\widetilde{\Lambda},\widetilde{\Xi}\right). \tag{6.37}$$

Assuming a unique inversion relation [8], the dependence on $\widetilde{\Lambda}$ and $\widetilde{\Xi}$ can be re-expressed as dependence on $\widetilde{C}$ and $\widetilde{H}$, leading to the final form of the state relation

$$\widetilde{\phi}=\widetilde{\mathfrak{L}}\left(\widetilde{Z},\widetilde{Z''^2},\widetilde{C},\widetilde{H}\right), \tag{6.38}$$

where $\widetilde{\mathfrak{L}}$ is the flamelet library established on the steady-state flamelet solution, convoluted with the presumed subfilter PDF.

6.1.4.4 Subfilter variance modeling

A scalar-gradient-based scaling law is used to obtain a closed-form algebraic equation for the subfilter variance, $\widetilde{Z''^2}$ [14, 163]

$$\widetilde{Z''^2} = C_v \Delta^2 |\nabla \widetilde{Z}|^2, \tag{6.39}$$

where C_v is the model constant determined dynamically, and Δ is the filter width. The following expression (dynamic procedure) is used to determine the model constant

$$C = \frac{\langle LM \rangle}{\langle MM \rangle}, \tag{6.40}$$

where $\langle\rangle$ indicates once again Lagrangian averaging, and the quantities L and M are defined as

$$L = \widehat{\widetilde{Z}\widetilde{Z}} - \widehat{\widetilde{Z}}\widehat{\widetilde{Z}}, \tag{6.41}$$

and

$$M = \hat{\Delta}^2 \nabla \widehat{\widetilde{Z}} \cdot \nabla \widehat{\widetilde{Z}}. \tag{6.42}$$

The top hat operator $\widehat{\ }$ indicates the second filtering operation at the test filter level, with filter width $\hat{\Delta}$.

6.1.5 PAH relaxation model

Soot formation depends critically on the concentrations of its precursors, namely aromatic hydrocarbons (AH), which exhibit substantial transient effects due to turbulent unsteadiness [42]. To account for these effects, as mentioned in the previous chapter, spatially filtered transport equations are solved for their mass fractions [22, 130]

$$\frac{\partial \overline{\rho} \widetilde{Y}_{AH}}{\partial t} + \nabla \cdot (\overline{\rho} \widetilde{Y}_{AH} \widetilde{\mathbf{u}}) = \nabla \cdot (\overline{\rho} \widetilde{Y}_{AH} \widetilde{\mathbf{u}} - \widetilde{\overline{\rho} Y_{AH} \mathbf{u}}) + \nabla \cdot (\overline{\rho} \widetilde{D} \nabla \widetilde{Y}_{AH}) + \overline{\dot{\omega}}_{AH}. \tag{6.43}$$

With a conventional dynamic model for the subfilter scalar fluxes [11, 12, 13], the only unclosed terms in the above equations are the filtered chemical source terms $\overline{\dot{\omega}}_{AH}$.

The chemical source terms for these transported aromatic species are closed using the relaxation model described in [25] (previous chapter). By grouping respectively the chemical production and consumption reactions of an aromatic species with n aromatic rings (A_n), its chemical source term is given by

$$\dot{\omega}_{A_n} = a \cdot Y_{A_{n-1}} - b \cdot Y_{A_n}. \tag{6.44}$$

The coefficients a and b (both positive) were found independent of the species mass fractions [25] and can be tabulated solely using flamelet solutions by dividing the production and consumption rates of A_n by the mass fraction of A_{n-1} and A_n, respectively

$$a = \frac{\dot{\omega}^+_{A_n}}{Y_{A_{n-1}}}, \text{ and } b = \frac{\dot{\omega}^-_{A_n}}{Y_{A_n}}. \tag{6.45}$$

Benzene (C_6H_6) is the first aromatic species formed in the gas-phase mixture. Therefore, in this model, it is the first species for which unsteady effects are considered and its overall chemical source term is tabulated directly based on flamelet solutions [25]. For aromatic molecules beyond benzene, the model represented by Eq. 6.44 is used. In the current work, as a first step, only benzene and naphthalene ($C_{10}H_8$) are considered, due to the relatively high uncertainties in the chemistry of PAH larger than naphthalene. It is important to note that the accuracy of the proposed PAH relaxation model is limited by that of the full chemical mechanism.

The correlations in both terms on the right hand side of Eq. 6.44 are closed using the turbulence closure model proposed in [8, 22, 130]. This leads to the final form of the filtered chemical source terms for C_6H_6 and $C_{10}H_8$

$$\overline{\dot{\omega}}_{C_6H_6} = \overline{\dot{\omega}}_{C_6H_6}\left(\widetilde{Z}, \widetilde{Z''^2}, \widetilde{C}, \widetilde{H}\right), \tag{6.46}$$

$$\begin{aligned}\overline{\dot{\omega}}_{C_{10}H_8} &= \overline{a}\left(\widetilde{Z},\widetilde{Z'^2},\widetilde{C},\widetilde{H}\right)\cdot\widetilde{Y}_{C_6H_6} \\ &- \overline{b}\left(\widetilde{Z},\widetilde{Z'^2},\widetilde{C},\widetilde{H}\right)\cdot\widetilde{Y}_{C_{10}H_8} \\ &- \overline{d}\left(\widetilde{Z},\widetilde{Z'^2},\widetilde{C},\widetilde{H}\right)\cdot\left(\widetilde{Y}_{C_{10}H_8}\right)^2, \end{aligned} \tag{6.47}$$

in terms of spatially filtered quantities. The third term on the right hand side of Eq. 6.47 corresponds to the removal of naphthalene due to dimerization, leading to the nucleation of soot [22, 115]. The turbulent closure of this term, same as introduced by Mueller and Pitsch [22], approximates the average of a square by the square of the average. The present work assumes that soot nucleates only from the dimerization of naphthalene, since it is the largest PAH considered [22].

6.2 Choice of the flame under study

6.2.1 Experimental studies of non-sooting turbulent non-premixed flames

Progress in the fundamental understanding of turbulent combustion and in the development of computational combustion models has been enabled by the availability of detailed scalar and velocity measurements on increasingly well-characterized flames and by both quantitative and qualitative comparisons between measured data and numerical simulation results. Previous research efforts have been devoted along this direction within the framework of the International Workshop on Measurement and Computation of Turbulent Non-premixed Flames (TNF) [164].

In the frame of TNF, laboratory-scale turbulent flames have been routinely used to study non-premixed turbulent combustion. Several types of experimental set-up (primarily flame burners) have been used. On the one hand, complex burners, such as the bluff-body combustor [165] and the TECFLAM swirl burner [166], have been designed to mimic the combustion environment in practical combustion devices. However, these configurations are either complex in construction or have limited access for optical measurements [94]. On the other hand, simple jet burners [167, 168, 169] have also been employed, since they have well characterized inlet flow conditions and can be operated as open flames, facilitating the implementation of laser diagnostic and eliminating both experimental and

computational complications arising from enclosed flows [94]. Based on simple jet burners, piloted burners, utilizing a premixed pilot flame system that surrounds the fuel jet, have been designed. These piloted turbulent jet flames [63, 92, 136] can sustain stable flames for a wide variety of fuels, and at high jet velocity without experiencing liftoff or blowout. The most well-studied piloted combustor is the so-called Sydney burner [170], which has been been used for the series of flames experimentally studied at the Sandia National Laboratories (flames A through F) [63, 92, 136]. These Sandia flames have been subject of many computational investigations [8, 58, 171, 172]. A similar poiloted burner is the Delft natural gas burner [173].

The various turbulent non-premixed flames mentioned above have been selected as target flames for the TNF workshop over more than one decade [164]. However, since the primary focus has been placed on the characterization of major combustion characteristics, the soot yield (volume fraction) in these TNF target flames is only on the order of several parts per billion (ppb). The fuels used in these flames have been selected to avoid sooting conditions, mostly methane with different levels of dilution by nitrogen. Numerical simulations [8, 56, 57, 58, 59, 60, 61, 171, 172] of these flames have been targeting the accurate prediction of the mean and variance of the velocity, temperature, mass fractions of major combustion products (e.g. H_2O, CO_2), and several intermediate combustion products with relatively high concentration (e.g. CO, NO). The flamelet-based combustion model, LES closure models, and radiation models employed in the current study have been developed and tested extensively in previous numerical investigations on these flames [8, 15, 56, 57, 58, 60]. These models have been demonstrated to be able to capture the very complex turbulent flow field and major combustion characteristics accurately.

6.2.2 Experimental studies of sooting turbulent non-premixed flames

Soot formation and oxidation introduces additional challenges in addition to those involved in turbulent non-sooting flames. Such new challenges involve chemical and physical processes interacting over a wide range of time scales, and strong thermal radiation from soot modifying the local flame temperature, which has coupled effects on the gas-phase chemistry. Motivated by the strong de-

sire to improve the predictive modeling capability for soot formation and emission, spatially and temporally resolved data in turbulent reacting flow fields, specifically for sooting fuels (fuels with higher-C-number than methane), are in pressing need for the validation of predictive models of soot formation. As mentioned previously, such data has been in development for many years for soot-free, turbulent non-premixed flames, in the frame of the TNF workshop, and more recently for a slightly sooting methane flame [174].

There have been a number of previous experimental investigations of sooting non-premixed turbulent jet flames using heavier hydrocarbon fuels than methane, notably acetylene, ethane, ethylene, propane, and kerosene [175, 176, 177, 178, 179, 180, 181, 182, 183, 184, 185, 186, 187, 188, 189, 190, 191, 192, 193, 194, 195]. Unfortunately, these sooting flames were not designed with modeling in mind and suffer from one or more important deficiencies in this regard [94]. These deficiencies include not providing a coflowing air stream to prevent ambient disturbances, having insufficient fuel tube length to achieve fully developed turbulent pipe flow profiles at the fuel pipe exit, or having a poorly characterized pilot flame exit flow.

6.2.3 Selected flame

Recently, the experimental investigation of a series of piloted non-premixed turbulent sooting jet flames has been reported by Zhang and Shaddix [94] for gaseous ethylene fuel. The design of these flames and their burner configuration is inspired from previous experimental investigations of non-sooting turbulent non-premixed flames, specifically the Sandia flames [63, 92, 136]. These recent sooting flames represent a natural progression from simple (methane) to more complex (ethylene) fuel chemistry. These flames are different from other sooting turbulent non-premixed flames for the well-characterized conditions at the exit of various nozzles, well-designed co-flowing oxidizer stream, and well-justified dimensions of the different nozzles [94]. In addition, the burner configuration and running conditions of these flame are very similar to those of the Sandia flames. The similarities between these flames and the Sandia flames further justify the appropriateness of using the various models described in the previous section, since these numerical combustion models have been

extensively validated in the numerical investigations of the Sandia flames, as mentioned previously (Section 6.2.1).

The series of ethylene/air sooting turbulent jet flames mentioned above contains four different flames. The flow parameters and the visible flame heights are listed in the table below. Fast-shutter digital photographs of these flames are reproduced in Fig. 6.1.

Fuel exit Reynolds number	Main jet exit velocity [m/s]	Pipe fuel radius R flow rate [slpm] R	Visible flame height [mm]
10,000	27.4	0.26	660
15,000	41.0	0.39	760
20,000	54.7	0.52	840
25,000	68.4	0.66	860

Table 6.1: Flow parameters for the four piloted ethylene jet flames studied by Shaddix and Zhang.

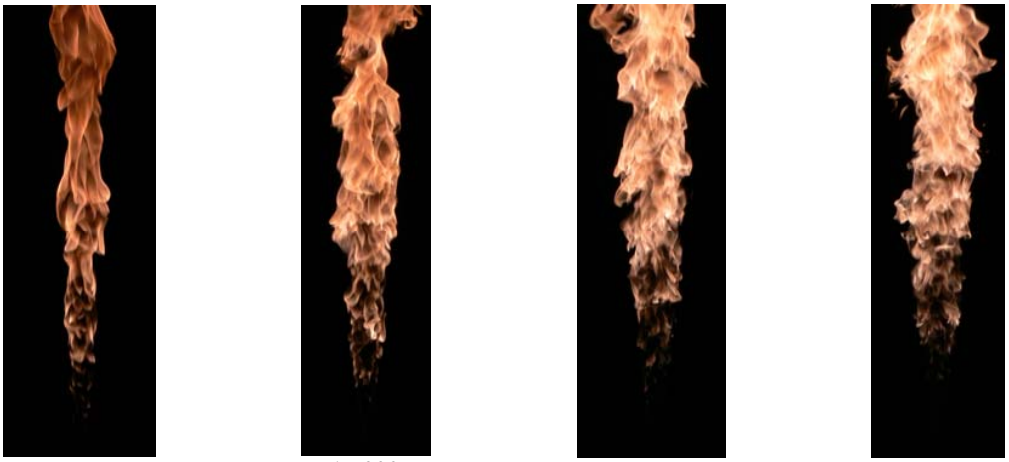

Figure 6.1: Fast-shutter photographs of ethylene jet flames stabilized on the piloted jet burner. These figures are taken from Shaddix et al. [94,157,197]

Out of these four flames, we choose the flame with a fuel exit Reynolds number of 20,000 as the target flame for our numerical investigation. This flame has sufficiently strong turbulence to test the robustness of combustion models, and yet not frequent local extinction (as in the flame with a fuel exit Reynolds number of 25,000), which would introduce additional modeling challenges to handle local extinction and re-ignition.

This flame is representative of other turbulent sooting flames, and offers an ideal combustion environment to study soot nucleation (close to the burner), soot growth by condensation and surface

reactions (mid-height of the flame), and soot oxidation (close to the flame tip). This flame has been selected as one of the target flames for the forthcoming International Sooting Flames (ISF) workshop for the same reasons, and the present LES is the very first numerical study on this flame [26]. Details about the flame configuration are provided in the next section.

6.3 Simulation details

The models previously described are integrated into LES of a non-premixed ethylene/air piloted turbulent jet flame, experimentally investigated at the Sandia National Laboratories [94, 157, 196].

6.3.1 Flame configuration

A schematic of the burner configuration is depicted in Fig. 6.2. The burner consists of two concentric

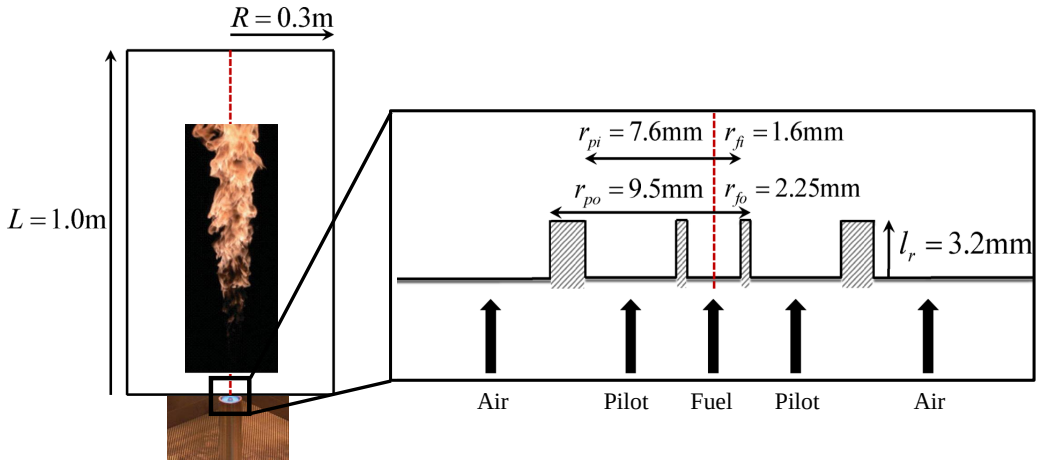

Figure 6.2: Schematic of the burner configuration.

tubes, with high-speed fuel injection in the inner one, and low-speed injection of fuel/air mixture in the outer one (pilot flame). The flame is attached to the burner and stabilized by 64 tiny premixed pilot flames arranged in three concentric rings, which guarantee a flat pilot flow profile. While the fuel jet delivers pure ethylene, premixed ethylene/air mixture at an equivalence ratio of 0.9 is supplied as pilot stream, at a flow rate corresponding to 2% of the energy release rate of the main jet. Finally, the burner sits on top of a vertical wind tunnel, providing wide co-flowing air to prevent

room-air disturbances. The characteristic parameters of the burner and the inlet co-flow are listed in Table. 6.2.

Fuel jet inner diameter D_{fi}	0.0032 m	Pilot inner diameter D_{pi}	0.0152 m
Fuel jet outer diameter D_{fo}	0.0045 m	Pilot outer diameter D_{po}	0.0191 m
Fuel jet wall thickness W_f	0.00065 m	Pilot wall thickness W_p	0.00195 m
Fuel stream bulk velocity	54.7 m/s	Oxidizer stream bulk velocity	0.6 m/s
Fuel stream inlet temperature	294 K	Oxidizer stream inlet temperature	330 K
Pilot plane recession L_r	0.0032 m	Pilot stream bulk velocity	0.43 m/s

Table 6.2: Characteristic parameters for the piloted turbulent jet flame.

A more detailed description of the burner configuration is given in [94, 157, 196]. Based on the bulk velocity and diameter of the fuel jet, the jet Reynolds number is estimated to be approximately $Re = 20,000$. This high Reynolds number justifies the unity Lewis number assumption made in the PAH relaxation model and the gas-phase combustion model described earlier [63].

6.3.2 Numerical set-up

The filtered conservation equations for mass, momentum, mixture fraction, progress variable, enthalpy loss parameter, and the two aromatic species mass fractions (benzene and naphthalene) are solved in a cylindrical coordinate system using the NGA code [90]. The scalar equations are discretized spatially using the BQUICK scheme [39].

Details about the numerical set-up, such as the boundary conditions, the choice of grid resolution, and the generation of the flamelet library are provided below.

6.3.2.1 Boundary conditions

The boundary conditions for all the velocity components and scalar quantities are similar to the case of the laminar flame, studied in Chapter. 3. These conditions are described in detail in Chapter. 3.1.3. There are three inlet boundary conditions to specify, one for each of the three streams (fuel, pilot, and air).

Instead using of a constant Dirichlet boundary inlet conditions as in the case of the laminar flame studied in Chapter. 3, a time-dependent Dirichlet boundary condition is used in this simulation.

The turbulent inlet velocity profile for the fuel stream is extracted from a separate, fully-developed periodic pipe flow simulation with the experimentally measured axial mean bulk velocity. More details are provided in Section 6.3.2.2. The velocity inlet profilesfor the pilot and air streams are treated as flat with their corresponding bulk velocities shown in Table. 6.2. These boundary conditions have been extensively used in the numerical investigations of similar turbulent non-premixed jet flames [8, 56, 57, 58, 59, 60, 61, 171, 172].

In this simulation, gas-phase combustion is modeled using the extended Flamelet/Progress Variable approach, as mentioned earlier. The species mass fractions are not transported along with the flow field; instead, the flamelet variables (Z, C, and H) are transported. Their values, along with those of the transported aromatic species mass fractions (benzene and naphthalene), at the inlet boundaries are summarized in the following table.

	Z	C	H	$Y_{C_6H_6}$	$Y_{C_{10}H_8}$
fuel steam	1	0	0	0	0
pilot steam	0.0626	0.247	0	0	0
oxidizer steam	0	0	0	0	0

Table 6.3: Details of the inlet conditions for the transported scalar quantities.

In the pilot stream, the value for the mixture fraction variable is set to the stoichiometric value for ethylene combustion in air ($Z = Z_{st} = 0.0626$). The value for the progress variable is set to the corresponding value on the burnt side of a one-dimensional ethylene/air freely-propagating premixed planar flame ($C = 0.247$). This flame is computed using the FlameMaster code [103].

6.3.2.2 Fully-developed pipe flow simulation

A separate, incompressible, fully-developed periodic pipe flow simulation is performed to generate the time history of the turbulent inlet velocity profile for the fuel stream. This time history is used as input in the turbulent flame simulation. For this purpose, only the velocity field is solved for, with no transported scalar. The pressure is imposed to be the ambient pressure, as specified in the experimental study [94]. The density and viscosity of the flow is imposed from FlameMaster calculations for ethylene at 294 K under ambient pressure (fuel conditions from [94]).

In this large-scale simulation, the fuel pipe is simulated on a periodic domain in the stream-wise direction. The pipe length is selected to be $10D_{fi}$. The azimuthal direction is discretized using 64 uniformly distributed grid points. The mesh used in the radial direction contains 64 grid points and is, beginning at the pipe wall, stretched towards the centerline of the pipe, using a hyperbolic tangent function with a stretching rate of 2.8. In the axial direction, the grid is uniform, with 128 grid points. A plane cut of the computational domain at a fixed azimuthal angle is shown in Fig. 6.3.

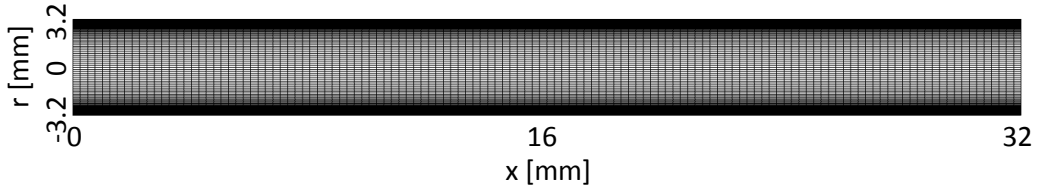

Figure 6.3: A plane cut of the computational domain at a fixed azimuthal angle ($\theta = 0$).

No-slip boundary conditions are used at the pipe walls (top and bottom boundaries in Fig. 6.3). Parabolic boundary conditions are used in the axial direction (left and right boundaries in Fig. 6.3). A parabolic profile with the experimentally measured axial mean bulk velocity is used as initial condition at the inlet boundary superimposed with random perturbations. The same LES closure models are used in this pipe flow simulation, as those used in the turbulent flame simulation (dynamic Smagorinsky model with Lagrangian averaging techniques, see Section 6.1.4.2).

The simulation is performed over 20 flow through time (0.011 second in physical time) to be statistically stationary (fully-developed pipe flow). The simulation is then recorded for 0.1 second in physical time, to provide the turbulent inlet velocity profiles, which will be used in the flame simulation. To assess the performance of the pipe flow simulation, the time-averaged velocity profile near the pipe wall is plotted in Fig. 6.4, in wall units.

The wall coordinate is calculated as

$$y^+ = \frac{yu_\tau}{\nu}. \tag{6.48}$$

The dimensionless velocity is calculated as

$$u^+ = \frac{u}{u_\tau}. \tag{6.49}$$

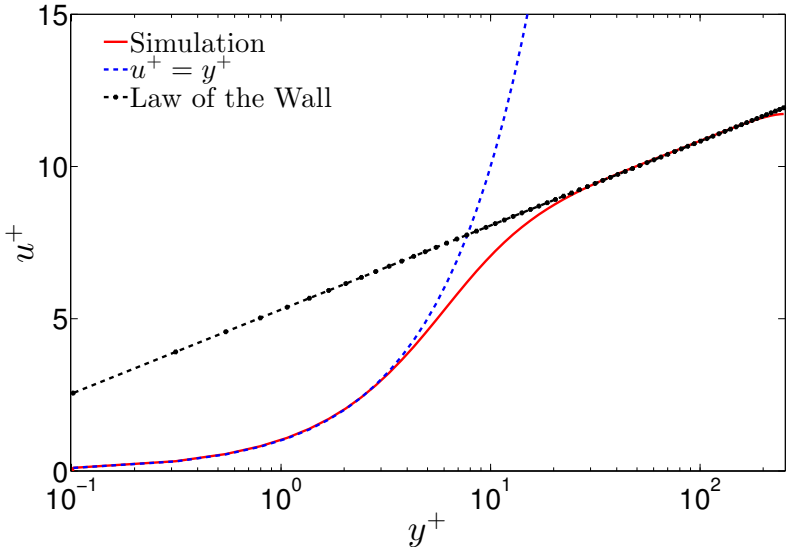

Figure 6.4: Velocity profile near the pipe wall.

In the above equations, the friction velocity is calculated as

$$u_\tau = \sqrt{\frac{\tau_w}{\rho}}, \tag{6.50}$$

where the wall shear stresses is calculated as

$$\tau_w = \mu \frac{\partial u}{\partial y}|_{y=0} \tag{6.51}$$

In Fig. 6.4, the grid point closest to the wall is shown to be at $y^+ \simeq 0.1$. Therefore, the grid resolution used in the pipe flow simulation provides a well resolved near-wall region. Quantitatively, the asymptotic behavior, $u^+ = y^+$ is well captured in the viscous sublayer, for $y^+ < 5$. In the log-law region ($20 < y^+ < 200$), the law of the wall is also well reproduced. Overall, the reasonably good results from the pipe flow simulation provide high-fidelity inlet conditions for the fuel stream, which are necessary for the accurate prediction of the turbulent flame.

6.3.2.3 Choice of the computational domain and grid resolution for flame simulation

Based on the visible flame height (0.84 m) and width (0.2 m) measured in the experiments, the size of the computational domain is selected to be $1m \times 0.3m \times 2\pi$ in the axial, radial, and azimuthal directions, respectively (Fig. 6.2).

The discretization of the computational domain should be done with great care for three reasons. First, the various co-flowing streams generate thin shear layers, which need to be well captured. It requires a minimum level of grid resolution in the radial direction to capture these shear layers. Second, soot formation occurs at downstream locations ($x/d > 50$ as observed in the experiments [94]), and is very intermittent spatially. Once again, a minimum level of grid resolution in the axial direction is required for the accurate prediction of soot formation and growth. Finally, the trade-off between computational cost and accuracy sets an upper limit to the total number of grid points (typically two to five million grid points) to make the simulation affordable. Based on the above considerations, the grid points need to be distributed in an optimal fashion, to achieve high accuracy and computational efficiency.

Following previous numerical investigations of similar piloted turbulent jet flames [8, 15, 22], the general strategy for the discretization of the computational domain is the following. The grid in the axial direction is the finest at the burner exit. To save some computational cost, the grid can be, beginning at the burner exit, stretched downstream. A larger stretch rate may be used at more downstream locations. The grid in the radial direction needs to be the finest within the shear layers between the fuel and pilot streams and between the pilot and oxidizer streams. To save some computational cost, the grid can be stretched away from the walls in each stream. In the azimuthal direction, using 64 uniformly distributed grid points is a common practice in similar previous studies and was shown to be sufficient to capture the complex turbulent flow field [8, 15, 22].

Following the general strategy described above, five different mesh configurations have been developed for this simulation. Details of these meshes are summarized in the following table. For these meshes, the smallest and largest cells in the axial direction are located at the burner exit at the outflow plane, respectively. The smallest cell in the radial direction is located in the shear layer

	Mesh 1	Mesh 2	Mesh 3	Mesh 4	Mesh 5
nx	234	296	192	384	468
ny	184	184	102	204	204
nz	64	64	64	64	64
Total grid points [$\times 10^6$]	3.3	3.5	1.25	5.0	6.1
Δx_{min} [mm]	0.15	0.1	0.2	0.1	0.1
Δx_{max} [mm]	29	24	36	18	8.2
Δr_{min} [mm]	0.03	0.03	0.05	0.025	0.025
Δr_{max} [mm]	33	33	58	29	29

Table 6.4: Details of the computation meshes tested at different grid resolutions.

between the fuel and pilot streams, while the largest cell in that direction is located at the edge of the oxidizer stream. The total number of the grid points used in these meshes range from 2.5×10^6 to 6.1×10^6.

Mesh 1 and Mesh 2 are preliminary testing meshes used to initiate the simulation. Mesh 4 is more refined than Mesh 1 and Mesh 2 in both the axial and radial directions and is the mesh used for the final simulations. Mesh 3 is twice coarser than Mesh 4 in both axial and radial directions. The grid point distribution used in Mesh 5 is the same as in Mesh 4 in the radial direction. However, the grid is more refined (by a factor of more than 2) for Mesh 5 than for Mesh 4 at downstream locations ($x/d > 50$) in the axial direction where soot forms. The grid used in the azimuthal direction for all five meshes is the same. The sensitivity of simulation results on the computational grid are illustrated in the following, using Mesh 3, Mesh 4, and Mesh 5. For these three meshes, the corresponding grid spacing diagrams in the axial (Δx) and radial directions (Δr) are shown in Fig. 6.5.

As aforementioned, the two most important locations in the flame under study are the shear layers close to the burner lip and the downstream locations where soot forms Both need to be well-captured with appropriate grid resolution. Effects of the grid resolution on important flow and combustion characteristics at these two locations are shown separately, by comparing simulation results obtained using Mesh 3, 4, and 5.

To investigate the effects of grid resolution on the shear layers, time-averaged mixture fraction, $\widetilde{Z}$, axial velocity, $\widetilde{U}$, and root mean square of mixture fraction, $Z_{\rm rms} = \widetilde{Z^2} - (\widetilde{Z})^2$, are plotted at two upstream locations (2.5 mm, $x/d \simeq 0.8$, and 5 mm, $x/d \simeq 1.6$, from the burner exit plane)

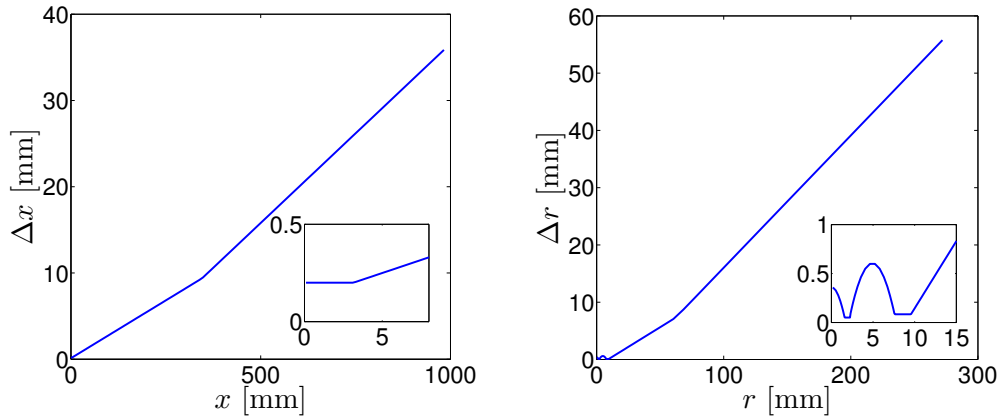

(a) Axial direction for Mesh 3.

(b) Radial direction for Mesh 3.

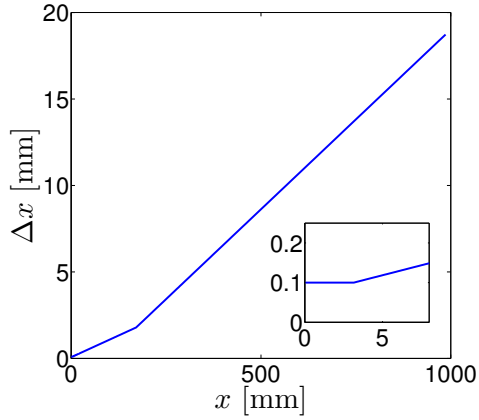

(c) Axial direction for Mesh 4.

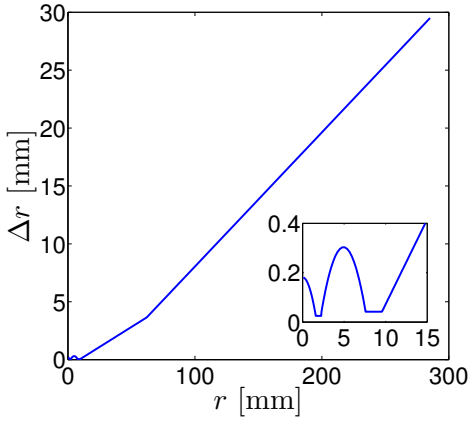

(d) Radial direction for Mesh 4.

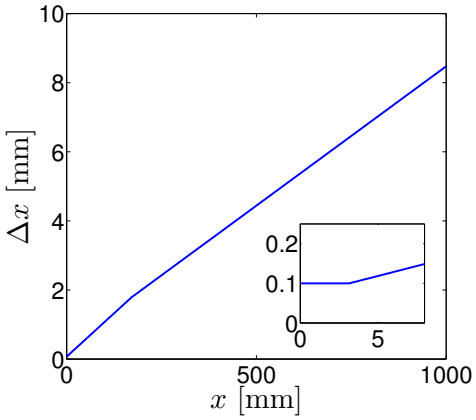

(e) Axial direction for Mesh 5.

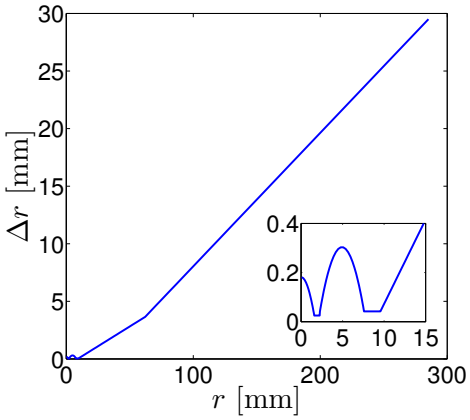

(f) Radial direction for Mesh 5.

Figure 6.5: LES grid stretching diagram for the three different resolutions. The axial direction is shown in the left column. The radial direction is shown in the right column. The insets in the graphs show zooms of the grid around the fuel nozzle.

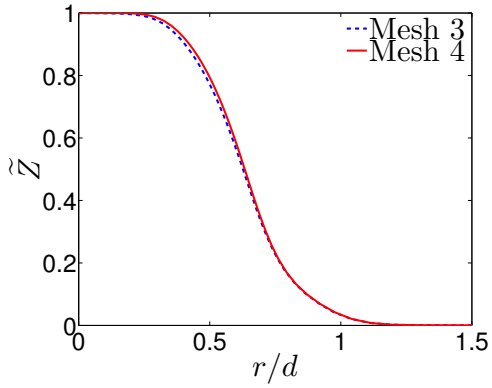

(a) Mixture fraction, 2.5 mm downstream.

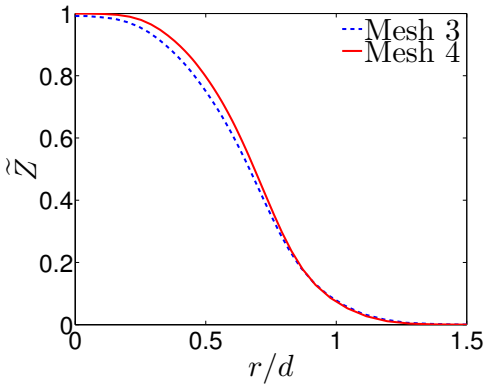

(b) Mixture fraction, 5 mm downstream.

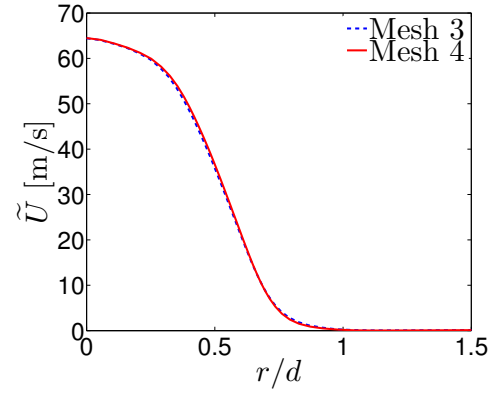

(c) Stream-wise velocity, 2.5 mm downstream.

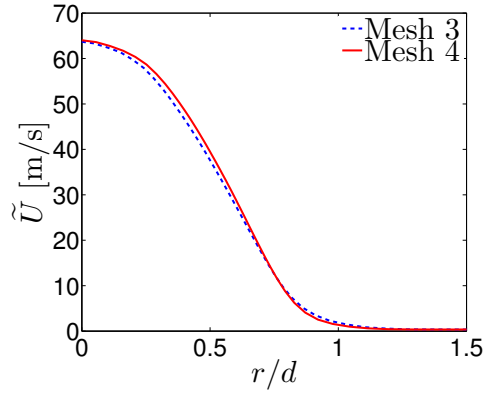

(d) Stream-wise velocity, 5 mm downstream.

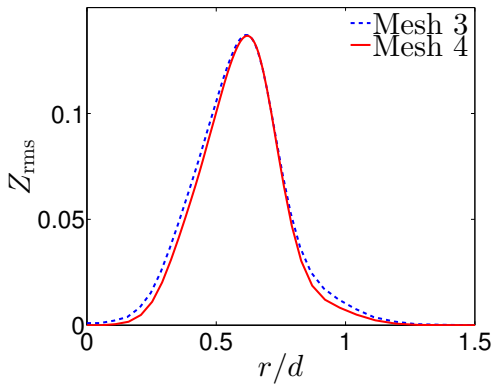

(e) RMS of mixture fraction, 2.5 mm downstream.

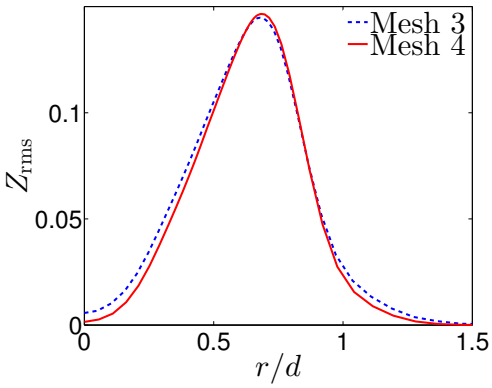

(f) RMS of mixture fraction, 5 mm downstream.

Figure 6.6: Time-averaged important characteristics at two locations close to the burner lip. Left column: 2.5 mm downstream of the burner lip. Right column: 5 mm downstream of the burner lip.

using results obtained with Mesh 3 and 4. Results obtained using Mesh 5 is not included since Mesh 5 uses the exact same grid as Mesh 4 in these shear layers. The Favre-averaged mean velocity is shown to focus on the development of the Kelvin-Helmholtz instability and the shear layer. The mean and root mean square of mixture fraction highlight the mixing of fuel and air in the turbulent shear layer. These three quantities are critical in reproducing any turbulent flames. For all these quantities, Fig. 6.6 shows that both meshes provide virtually the same results. Using an even finer grid than Mesh 4 in these shear layers will burden the simulation with additional computational cost, and is expected to have negligible effects on the fluid mechanics and primary combustion characteristics (mixture fraction). Overall, Mesh 4 provides sufficient grid resolution to characterize the shear layers without introducing too much computational overload.

Soot does not form close to the burner exit and is only present at downstream locations far from the burner exit plane ($x/d > 50$). To investigate the effects of axial grid resolution on soot formation at these locations, time-averaged soot volume fraction is plotted in Fig. 6.7 at two downstream locations (x/d =50 and 140) using results obtained with Mesh 4 and 5. The first location corresponds to where soot inception is observed, and the second location corresponds to where the maximum mean soot volume fraction is found (See Section 6.4).

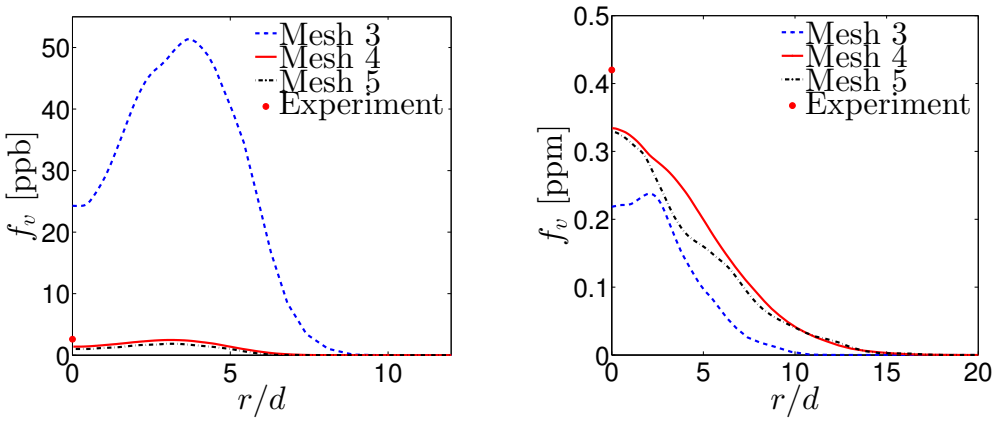

(a) Soot volume fraction at $x/d = 50$.

(b) Soot volume fraction at $x/d = 140$.

Figure 6.7: Time-averaged soot volume faction at two different locations for three different meshes.

At both downstream locations, due to the reduced axial velocity in the turbulent jet, the characteristic flow time scale is much larger than close to the burner. Therefore, simulation results need

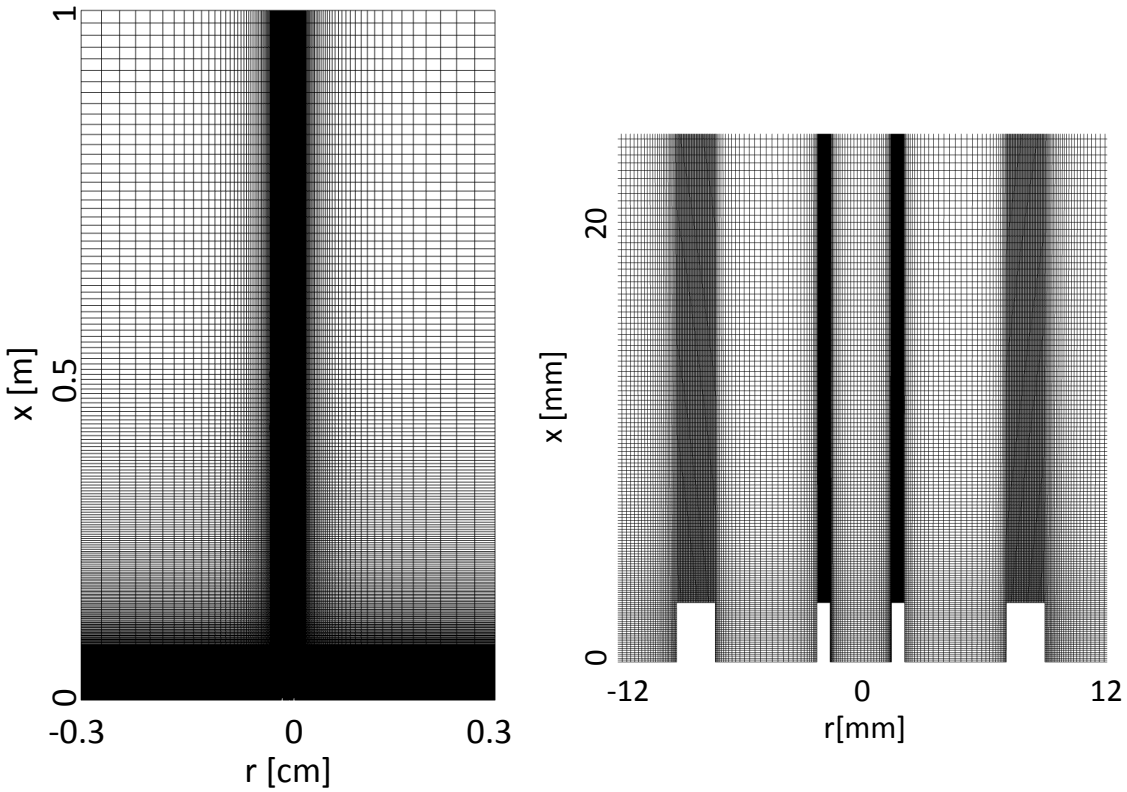

(a) Full domain.

(b) Zoom in the burner region.

Figure 6.8: A plane cut of the computational domain at a fixed azimuthal angel ($\theta = 0$).

to be averaged over a longer time period to eliminate artificial oscillations in the time-averaged statistics. This requires a longer simulation time. The run with the final mesh (mesh 4) is averaged over 0.89 second (physical time), the run with Mesh 3 is averaged over 0.11 second (physical time), and the run using Mesh 5 is averaged over 0.035 second (physical time). At both locations, only minor differences between results using Mesh 4 and 5 are observed, while large deviation is found between these results and those obtained using a coarser mesh (Mesh 3). The differences observed between results obtained with Mesh 4 and 5 at $x/d = 140$ are likely due to the short period of time, over which the simulation results using Mesh 5 are averaged.

Based on the above analysis, Mesh 4 provides sufficient grid resolution both in the shear layers close to the burner lip and at downstream locations where soot forms. This grid is used in the following for the turbulent flame simulation. A plane cut of the this mesh at a fixed azimuthal angel ($\theta = 0$) is depicted in Fig. 6.8.

The present analysis of the sensitivity of the simulation results to the resolution of the computational grid is, to the best of the author's knowledge, the best that can be done.

6.3.2.4 Generation of the flamelet library

The detailed chemical mechanism employed in the present flamelet-based combustion model is the same as the one used in the previous chapter for the perturbed flamelet analysis [25]. Similar to previous chapters, the unsteady flamelet equations (Eqs. 6.6 and 6.14) are solved using the FlameMaster code [103]. The resulting flamelet library leads to a smooth mapping of all the branches of the S-shaped curve. It is discretized with $100 \times 25 \times 100 \times 100$ grid points in $\widetilde{Z}$, $\widetilde{Z''^2}$, $\widetilde{C}$, and $\widetilde{H}$ directions, respectively. This flamelet library is the largest one that can be generated, given the memory per processor on the accessible, scientific computing platforms operated by the U.S. Department of Energy and the U.S. National Science Foundation.

6.3.2.5 Preliminary verification

The radial profile of temperature 5 mm downstream of the burner exit ($x/dsimeq1.6$) is compared to the measured temperature profile using line Rayleigh imaging [94]. It can be seen that the both the shape and magnitude of the experimentally measured profile is very well reproduced by the LES (Fig. 6.9).

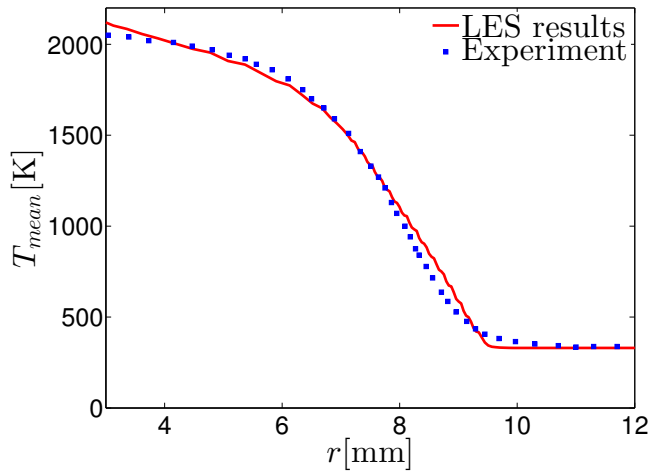

Figure 6.9: Radial profile of the temperature 5 mm downstream of the burner lip.

The good agreement with experimental measurements indicates that the current modeling strategy for the pilot flames is appropriate. More precisely, the ensemble of the 64 tiny premixed pilot flames (in the experimental set-up) can be modeled as a single pilot flame with flat velocity inlet profile, as has been done in similar previous numerical studies [8, 15, 22]. Further, the good agreement between the simulation results and experimental measurements between r =5 mm and r =10 mm indicates that the mixing process is well captured. This further justifies that the grid resolution selected is sufficient to well characterize the shear layers between different flow streams.

Unfortunately, no species measurements or other temperature measurements are provided as part of the original experimental work [94]. Under these conditions, the quality of the numerical predictions may not be fully assessed.

6.3.3 Computational cost

In this simulation, the size of the computational time step, Δt, is determined by the limiting convective Courant-Friedrichs-Lewy (CFL) number, $u\Delta t/\Delta x$, where u is the convective velocity and Δx is the computational cell size. The CFL number reaches its maximum at the burner exit where the smallest computational cells are present and the flow velocity is the highest. Given the computational cell size at the burner exit ($\Delta x = 6.5 \times 10^{-5}$m) and the fuel injection velocity ($v_f = 54.7$m/s), the time step size is fixed at $\Delta t = 1 \times 10^{-6}$s to ensure a convective CFL number smaller than 0.8 throughout the computational domain, for stability considerations. The numerical simulation is run over eight flow-through times to obtain a statistically stationary flow field. However, due to the large time scales associated with soot formation, more than ten flow-through times are required to obtain converged soot statistics. The flow-through time, defined as

$$t_f = \int_0^L \frac{dx}{u} \tag{6.52}$$

along the flame centerline, is calculated to be $t_f = 0.09$s. Therefore, the simulation is advanced for $t_f/\Delta t \simeq 9 \times 10^4$ time steps.

The simulation requires typically 168 processors to achieve the highest computational efficiency, and the computational time spent per time step is around 11s (310μs per grid point). The contribution from each of the numerical processes is shown in Table. 6.5. Under these conditions, the total

	Momentum	Pressure	Scalar	Combustion	Soot	Sub-grid models
Time/step [s]	0.82	5.70	1.43	1.02	1.37	0.66
Time/step [%]	5.05	53.1	13.3	9.55	12.8	6.2

Table 6.5: Computational time spent per time step.

computational cost of the simulation is around 0.5 million CPU hours. The actual run time of the simulation is more than three months. For reference, the simulation of the non-reacting counterpart of the same turbulent jet is found to be approximately 7 times less computationally demanding.

6.4 Results and discussion

6.4.1 Instantaneous fields

The instantaneous fields of temperature, benzene mass fraction, naphthalene mass fraction, and soot volume fraction are depicted in Fig. 6.10. As expected, the main flame is attached to the burner due to the presence of the pilot flame. The yield of aromatic species and soot is predominant in fuel rich regions inside the stoichiometric mixture fraction iso-contour.

The formation of benzene is shown to initiate at $x/d \simeq 15$, while naphthalene is observed to form only after $x/d \simeq 50$. Soot formation occurs at locations even more downstream at $x/d \simeq 90$. These lags in formation locations reflect the combined effects of the sequential formation of aromatic species and soot, and the large time scales governing their formation. Soot volume fraction and naphthalene mass fraction are found to be highly intermittent, where thin and confined regions of high soot volume fraction are followed by extended low soot volume fraction regions [42], similarly to the experimental observations [94].

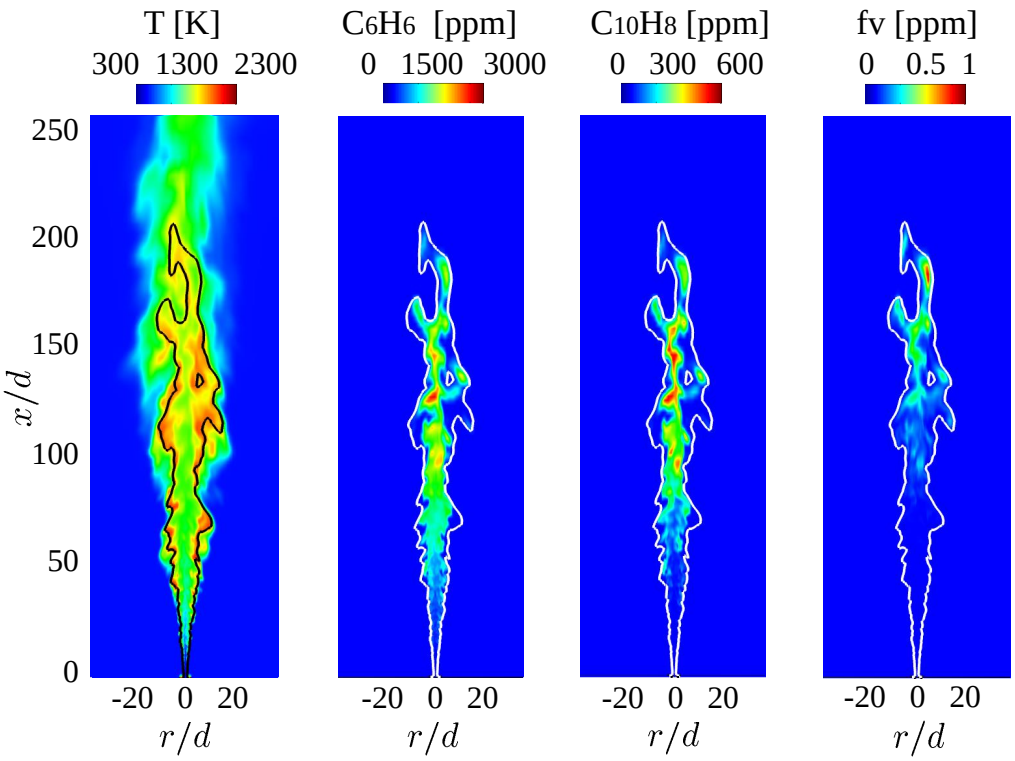

Figure 6.10: Instantaneous fields of temperature, benzene mass fraction, naphthalene mass fraction, and soot volume fraction. The iso-contour of stoichiometric mixture fraction (indicating the flame front) is shown in solid line.

6.4.2 Mean soot profile

To highlight the effects of the interactions between turbulence and PAH chemistry on soot, a separate LES is performed, in which aromatic species concentrations are tabulated directly using steady-state flamelet solutions (Eqs. 6.15 and 6.34), as for all other gas-phase species. As a consequence, aromatic chemistry-turbulence interactions are not included in this LES. In the following discussion, this second simulation is referred to as "steady-state LES", while the original simulation (aromatic species being transported) is referred to as "relaxation LES". As such, the only difference between the two LES simulations is the inclusion of the PAH relaxation model. Results from both simulations are compared to experiments, to quantify the effects of turbulence-chemistry interaction on the evolution and distribution of soot.

Figure 6.11 shows the time-averaged soot volume fractions on the flame centerline from both LES and from laser-induced incandescence measurements [196]. The relative uncertainty of the ex-

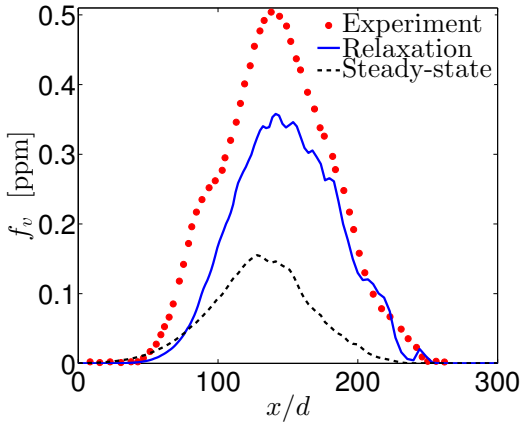

Figure 6.11: Mean soot volume fraction on the flame centerline.

perimental data was ±20% [196]. Comparison between LES data and experimental results indicates that the relaxation LES predicts the mean soot distribution reasonably accurately. The simulation predicts the correct location of soot inception around $x/d = 50$, where the gradual increase in soot volume fraction through inception and growth is also qualitatively well reproduced. The peak in soot volume fraction occurs close to $x/d = 150$ in both experiments and the relaxation LES. The location where soot peaks corresponds to where soot nucleation balances soot oxidation. Since the height of the flame is reasonably well predicted compared to experimental observations [94], the peak soot location is well predicted in the simulation. The optical depth was calculated to be 0.02 ($\ll 1$) through a flame radius at the peak soot location ($x/d \simeq 150$). The optically thin assumption made in Section 6.1.4 is therefore acceptable. The magnitude of the mean soot volume fraction is slightly under-predicted for $x/d < 180$. This might be primarily due to the under-estimated filtered naphthalene dimerization rate (Eq. 6.47) and the exclusion of PAH species larger than naphthalene in the present study. Including more species to nucleate from would increase the total soot yield. At $x/d > 180$, oxidation dominates and eliminates soot. The relatively satisfactory mean volume fraction predictions at these locations indicate that the oxidation process is also well captured.

On the other hand, the steady-state LES predicts a lower soot yield and a slightly shifted soot profile towards the burner exit (peak in soot volume fraction occurs around $x/d = 130$). Furthermore, the increase in soot volume fraction, depicting the soot inception processes, starts closer to the burner exit. This pre-mature soot nucleation is not surprising as the yield of aromatic species is already at

the flamelet-predicted steady-state values at the burner exit.

6.4.3 Effects of PAH chemistry-turbulence interaction

From steady-state flamelet calculations using the same combustion configuration as in the turbulent sooting flame, it is found that the mass fraction of benzene (C_6H_6) reaches its maximum at a mixture fraction value around $Z_{C_6H_6} = 0.25$, and the mass fraction of naphthalene ($C_{10}H_8$) reaches its maximum at a mixture fraction value around $Z_{C_{10}H_8} = 0.23$. To investigate the importance of the interactions between turbulence and aromatic chemistry, the relaxation LES results are compared to the solutions of the steady-state flamelet equations for C_6H_6 and $C_{10}H_8$ along mixture fraction iso-contours at $Z_{C_6H_6}$ and $Z_{C_{10}H_8}$, respectively, as shown in Fig. 6.12. The mean profiles of C_6H_6 and $C_{10}H_8$ mass fractions, conditioned on mixture fraction, Z, scalar dissipation rate, χ, and enthalpy defect, H, are plotted in Fig. 6.12 as well.

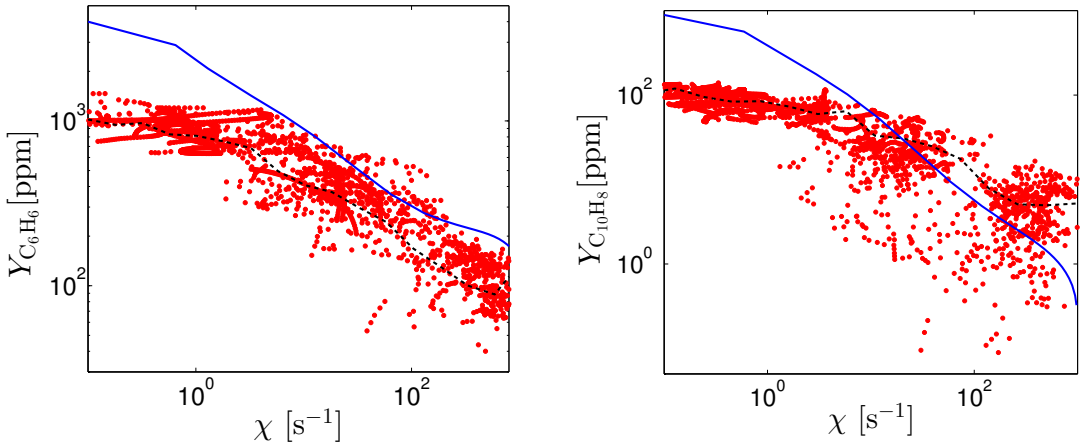

(a) Benzene. (b) Naphthalene

Figure 6.12: Mass fractions of C_6H_6 and $C_{10}H_8$ sampled at $Z_{C_6H_6}$ and $Z_{C_{10}H_8}$, respectively, from the relaxation LES are shown in red dots. Mean profiles conditioned on mixture fraction, Z, scalar dissipation rate, χ, and enthalpy defect parameter, H, are plotted in black dash line. The steady-state flamelet solutions are shown in blue solid line.

Within the range of scalar dissipation rates encountered in the relaxation LES, benzene mass fraction values fall in the range $10 < Y_{C_6H_6}[\text{ppm}] < 2000$, while naphthalene mass fraction spans a much wider range $0.1 < Y_{C_{10}H_8}[\text{ppm}] < 200$. Even in the absence of turbulent fluctuations

(steady-state flamelet solutions), the mass fraction of naphthalene displays a significantly stronger sensitivity to scalar dissipation rate compared to benzene. Significant scatter around the mean values is observed for both species, which may be explained by the rapidly changing turbulent flow field and the slowly adjusting chemical species. This result is consistent with findings from previous studies [42]. Furthermore, it can be seen that mass fractions of both benzene and naphthalene obtained from the relaxation LES do not scatter around the steady-state flamelet prediction. The difference between the conditional mean profile of the LES data and the flamelet prediction is more pronounced for naphthalene than for benzene. Similar behaviors have been found in previous studies of non-premixed flames under forced perturbation for species with relatively slow chemistry [83, 84]. These differences result primarily from the substantial turbulent unsteady effects on aromatic chemistry, and demonstrate that direct chemistry tabulation using steady-state flamelet solutions (Eqs. 6.15 and 6.34) is not appropriate for these aromatic species [25]. The flamelet solution at low scalar dissipation rate overestimates the mass fraction of both benzene and naphthalene. The difference is due to unsteady flamelet effects, which are known to be more pronounced at low scalar dissipation rate [16, 42].

In Figs. 6.13 and 6.14 time-averaged fields of naphthalene mass fraction and soot volume fraction obtained from the relaxation LES are compared against those obtained from the steady-state LES. Several observations can be made.

First of all, a systematic lag in the formation locations of benzene, naphthalene, and soot is observed between the two simulations. These aromatic species and soot are found to form at locations closer to the burner exit in the steady-state LES. Their delayed formation in the relaxation LES is due to the interactions between turbulence and their slow chemistry. It is interesting to note that the locations at which aromatic species concentrations and soot volume fraction peak ($x/d \simeq 150$) are practically the same between these LES, despite the differences in inception locations. Second, taking into account these unsteady effects (by transporting aromatic species) leads to larger aromatic species concentrations. This is primarily due to the non-monotonic time-evolution of the aromatic species and their chemical source terms [25]. The maximum mean mass fraction of benzene is around

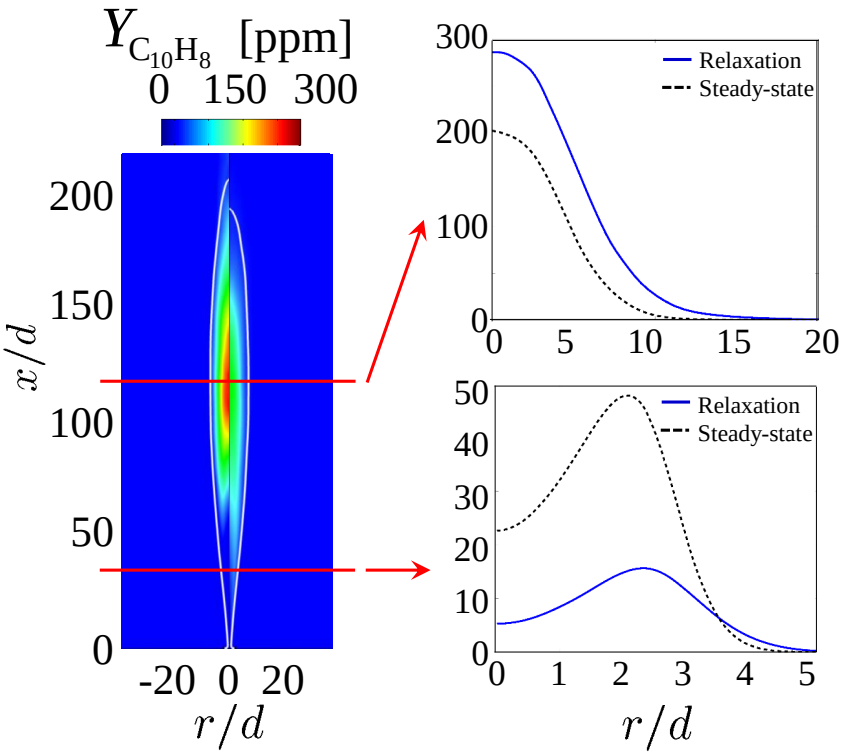

Figure 6.13: Time-averaged fields of naphthalene mass fraction. Results obtained using the relaxation model for transported aromatic species are shown on the left half. Results obtained using tabulated aromatic species concentrations are shown on the right half. The iso-contour of stoichiometric time-averaged mixture fraction (indicating the flame front) is plotted in white solid line. Radial profiles are plotted at $x/d = 30$ and $x/d = 120$.

1.6 times larger in the relaxation LES than in the steady-state LES. A similar observation can be made for naphthalene. The maximum mean soot volume fractions found in the relaxation LES and steady-state LES are 0.36 ppm and 0.15 ppm, respectively. This factor of 2.4 difference in soot is consistent with the factor of 1.5 difference observed in naphthalene, since the dimerization rate leading to soot nucleation scales as the naphthalene mass fraction to the second power (Eq. 6.47).

Finally, lower temperatures are found in the relaxation LES, compared to the steady-state LES, as shown in Fig. 6.15. These differences ($\simeq 100K$) are found at the same locations where large soot volume fraction is observed. They are due to the more pronounced radiative heat losses captured in the relaxation LES, associated with a larger predicted soot yield. Consequently, the relaxation LES predicts a flame 7% longer than that predicted by the steady-state LES [94, 197, 198].

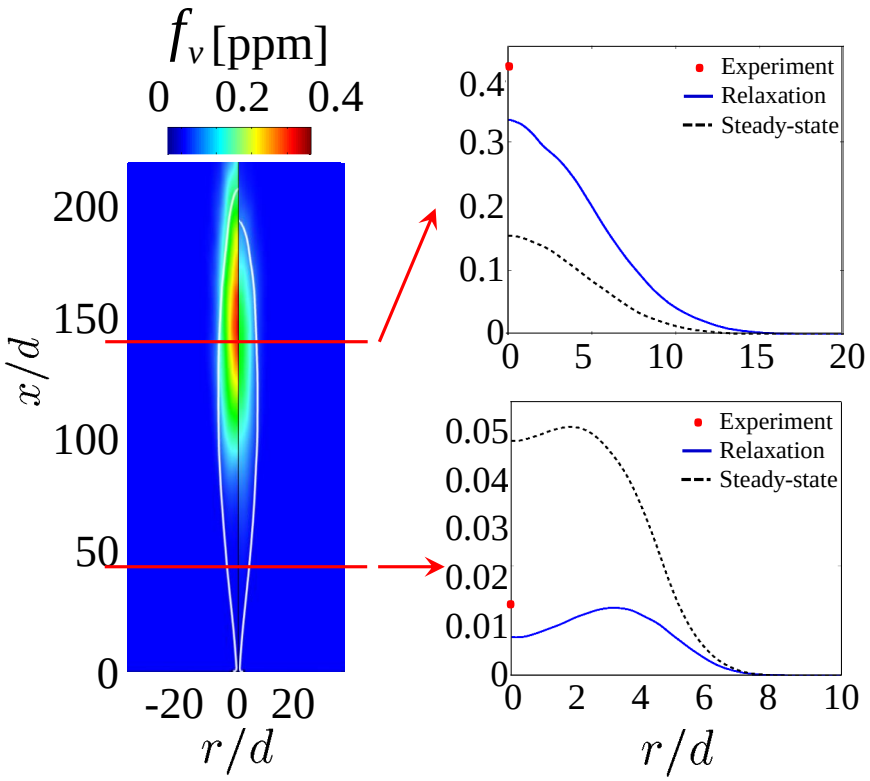

Figure 6.14: Time-averaged fields of soot volume fraction. Results obtained using the relaxation model for transported aromatic species are shown on the left half. Results obtained using tabulated aromatic species concentrations are shown on the right half. The iso-contour of stoichiometric time-averaged mixture fraction (indicating the flame front) is plotted in white solid line. Radial profiles are plotted at $x/d = 40$ and $x/d = 140$.

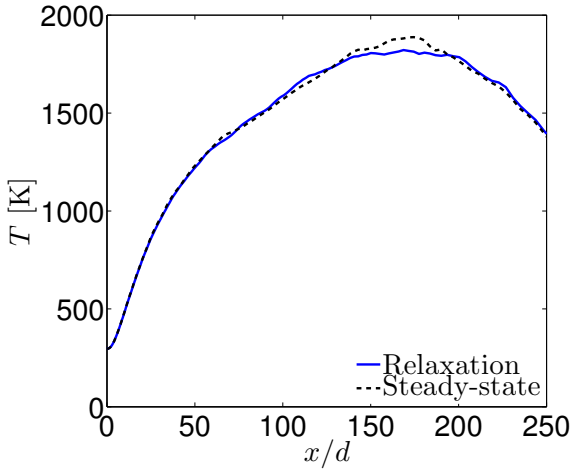

Figure 6.15: Mean profiles on the flame centerline.

6.4.4 Soot volume fraction fluctuations

Chemistry-turbulence interactions impact not only mean quantities, but also the fluctuations in soot, as shown in Fig. 6.16. Probability Density Functions (PDF) of soot volume fraction are calculated at mid-height ($x/d = 140$) and at an elevated height ($x/d = 200$) on the flame centerline, and they are compared against experimental measurements [157]. The experimental data on soot volume fractions are obtained using the 3-line diagnostic [94], with a relative uncertainty of $\pm 12\%$ [199].

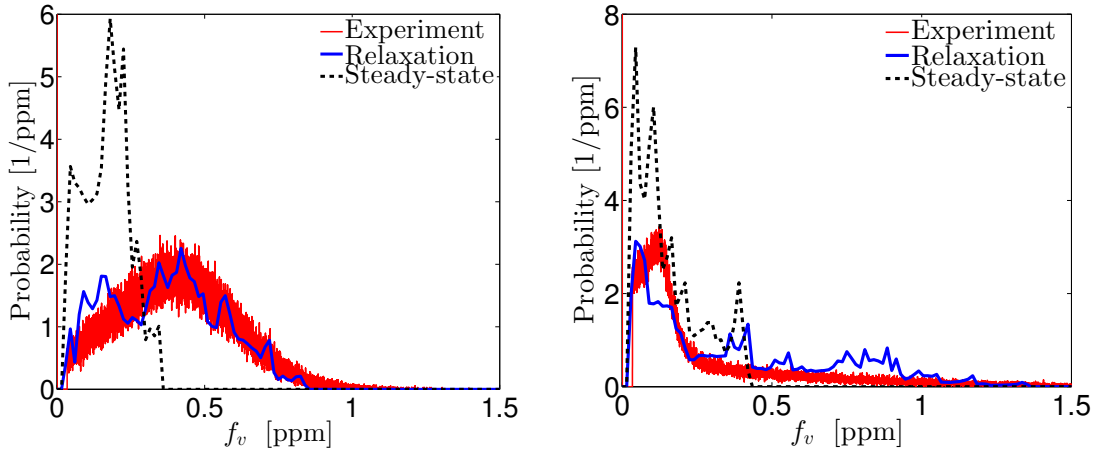

(a) $x/d = 140$ (44.8 cm). (b) $x/d = 200$ (64.0 cm).

Figure 6.16: PDFs of soot volume fraction at two locations on the flame centerline.

At $x/d = 140$, both the mean value and the magnitude of fluctuations (width of the PDF) are well captured by the relaxation LES; although occurrence of low soot volume fractions ($f_v < 0.2$ ppm) is slightly over-predicted. In contrast, the steady-state LES predicts a lower mean, as aforementioned, and significantly smaller fluctuations (narrower PDF).

At $x/d = 200$, the steady-state LES still over-predicts the occurrence of low soot volume fractions. The experimentally observed peak in soot volume fraction PDF centering at $f_v \simeq 0.2$ ppm is not well captured. It also fails to predict the tail in the experimentally measured PDF at large soot volume fractions: no occurrence of $f_v > 0.4$ ppm is predicted. In the relaxation LES, the tail of the PDF is much better reproduced, since larger fluctuations are enabled by taking into account chemistry-turbulence interactions using the relaxation model [25].

In the steady-state LES, the fluctuations in the mass fractions of different species, including PAH

species, primarily come from the fluctuations in the flamelet independent variables, namely, mixture fraction, Z, progress variable, C, and enthalpy defect, H. As can be seen in Fig. 6.16, including only these fluctuations in PAH mass fractions leads to significantly underestimated fluctuations in soot volume fraction, compared to the experimentally measured data. On the other hand, in the relaxation LES, fluctuations in the chemical source terms of PAH species are taken into account, through the relaxation model. These fluctuations come not only from the fluctuations in the flamelet independent variables through tabulation, but, also, from the turbulent transport of PAH species. By comparing the steady-state and relaxation LES results, it can be concluded that the turbulent transport of PAH species represents the major contributor to soot fluctuations.

Chapter 7

Conclusions and future directions

7.1 Conclusions

Presumed local flame structures (flamelets) have been shown to be a promising framework for the efficient numerical modeling of non-premixed reacting flows [53, 54, 55, 56, 57, 58, 59, 60, 61, 22, 62]. In the present study, new numerical models were developed for both laminar and turbulent flames, and tested under laboratory-scale configurations. Particular attention was given to the inclusion of multi-dimensional convection and diffusion effects in laminar non-premixed reacting flows and the proper treatment of unsteady chemistry-turbulence interactions for large aromatic compounds in turbulent non-premixed reacting flows.

7.2 Modified flamelet equations for YSI predictions

Conventional flamelet model was shown to be incapable of predicting the correct species mass fractions along the axis of a methane-air confined axisymmetric laminar co-flow diffusion flame. The main reasons for the failure of the conventional flamelet model were found to be the exclusion of multi-dimensional diffusion effects and the inability of capturing the strong convection effects on the rich side of the flame.

In an effort to overcome these deficiencies, a modified flamelet equation, valid only on the centerline of the flame, was proposed. Using the proposed modified flamelet model, sooting tendency (YSI) predictions were made for a wide range of aliphatic and aromatic hydrocarbons. The sooting

tendencies were estimated from the increment of PAH dimer production rate on the centerline of the flame when it is doped by a test species, without using an explicit soot model. Direct numerical simulation with detailed finite-rate chemistry was conducted *a priori* as reference results, and to provide the information required.

The present model is able to reproduce the species mass fractions correctly on the flame centerline. Furthermore, it suggests that the YSI of different hydrocarbons can be predicted by considering exclusively the chemistry mechanism, based on the knowledge of the undoped flame. This result is consistent with experimental observations [93]. Comparison between YSI in the literature and their predicted values has shown reasonably good agreement, and has highlighted deficiencies in the PAH formation sub-mechanism.

7.3 Curved flamelet formulation

The physical mechanism behind the aforementioned strong convection effects on the rich side of the flame was investigated further. A new flamelet formulation was derived, and its consistency was examined under different conditions. The convective velocities were found to result from the combined effects of the non-negligible curvature of mixture fraction iso-surfaces and the non-unity Lewis number transport of species in laminar non-premixed flames. Curvature was found to affect the transport of species by introducing a convection term in mixture fraction space.

To incorporate curvature effects in the one-dimensional flamelet formulation, tubular counter-flow diffusion flames and unsteady spherical mixing layers were selected to represent various curved flamelet structures. An approximate form for the scalar dissipation rate as a function of mixture fraction was found numerically for both configurations. Curvature was treated as constant in mixture fraction space to a first approximation. With the proposed form of scalar dissipation rate and curvature, one-dimensional numerical calculations using a detailed chemical mechanism were performed at different curvature values. Results showed that differential diffusion effects are enhanced by the presence of negative curvature, but reduced by the presence of positive curvature. Only minor curvature effects were observed for species with Lewis numbers close to unity.

The importance of this curvature-induced convection term was highlighted through a budget analysis based on the full chemistry simulation results for an axisymmetric laminar co-flow diffusion flame. A comparison was made on the flame centerline between species mass fraction profiles obtained from the full chemistry simulation and chemistry tabulation methods with and without curvature effects. A flamelet library without curvature effects was constructed *a priori* using flamelet solutions with a series of prescribed scalar dissipation rate values, while the one with curvature effects was established using flamelet solutions with the same prescribed scalar dissipation rate values and several prescribed curvature values. It was found that the chemistry tabulation based on curved flamelets gave significantly better results compared to its counterpart using planar flamelets, and achieved very good agreement with full chemistry simulation results.

Overall, chemistry tabulation based on solutions of the curved flamelet equations presents an attractive technique for gas-phase combustion modeling in laminar and mildly turbulent flames, since it has been found 100 times more efficient computationally than full chemistry calculations, yet with almost identical accuracy.

7.4 Chemistry-turbulence interactions

In previous work from the literature, the unity-Lewis number assumption has been found valid in the limit of sufficiently large Reynolds number, and the conventional flamelet model has been shown to represent well the conditional means of species mass fractions in piloted turbulent methane/air jet flames as the Reynolds number was increased [63, 66]. Consequently, the various issues pointed out for laminar flames become negligible in turbulent non-premixed reacting flows [25], as curvature effects and tangential diffusion are proportional to $1 - 1/Le_i$ [24].

In these turbulent non-premixed flames, motivated by the inability of existing steady-state flamelet formulations to account for the interactions between unsteady chemistry and fluid motions [42, 22], a new relaxation model was proposed for large aromatic compounds. This model was developed by examining the response of different species mass fractions to turbulent unsteadiness utilizing the one-dimensional unsteady diffusion flamelet model. Turbulent effects were modeled

through abrupt changes in the scalar dissipation rate. Steady-state flamelets at various initial stoichiometric dissipation rates were perturbed and the relaxation towards a new steady-state solution was analyzed.

It was found that gas-phase chemistry responds extremely fast for some radicals, such as OH and H, and still fast but to a lesser extent for small species, such as CO, CO_2, and C_2H_2. The steady-state flamelet assumption for these species is well justified and their mass fractions can be pre-tabulated legibly using the flamelet library based on solutions to the steady-state flamelet equations.

However, for polycyclic aromatic species (such as naphthalene and phenanthrene), the chemical production terms were found to be linearly proportional to the mass fraction of smaller aromatic species, and the chemical consumption terms were found to be linearly proportional to their own mass fractions. This type of behavior was explained by identifying the major pathways leading to the production and consumption of these PAH species. Based on these analyses, a linear relaxation model was proposed for PAH, and validated for several selected species in the context of unsteady flamelets. It was also shown that significantly better results were obtained using the proposed relaxation model over using previously developed relaxation models.

7.5 Effects of chemistry-turbulence interactions on soot formation

The effects of turbulent unsteadiness on the formation of aromatic species and soot were investigated further in a non-premixed ethylene/air piloted turbulent jet flame. Large-Eddy Simulations (LES) were performed on this flame. Transport equations for benzene and naphthalene mass fractions were solved along with the flow field to capture unsteady aromatic chemistry-turbulence interactions.

Several interesting conclusions can be drawn from the simulation. First, these interactions lead to a delayed inception of aromatic species away from the burner exit. The resulting inception locations for soot were shown to be in good agreement with experimental measurements [94]. Second, aromatic chemistry-turbulence interactions are also important to reproduce correctly the soot yield

in the flame. Neglecting these interactions (steady-state LES) leads to the under-prediction of the maximum mean soot volume fraction by a factor of three [157]. Finally, turbulent unsteadiness is critical to capture the strong fluctuations in soot volume fraction. Significant under-prediction of the occurrence of high soot volume fractions were observed when chemistry-turbulence interactions were not included for aromatic species [157].

7.6 Recommendations for future work

A relaxation model has been developed for the non-equilibrium reaction-diffusion process for large aromatic compounds in turbulent reacting flows [25]. The associated analysis also suggests a possible means for the systematic reduction of chemical mechanisms, not solely based on the chemical kinetics, but from a local flame structure point of view. The same methodology can be extended to investigate the evolution of other pollutants (*e.g.* NO_x and SO_x) with slow chemistry. Additionally, more fundamental concerns can be addressed, such as those associated with the effects of temporal turbulent intermittency on the formation of slow-chemistry molecules [83, 200].

Although the one-dimensional curved flamelet formulation offers attractive advantages, tangential diffusion effects are still not taken into account [24]. These effects lead to the breakdown of the presumed one-dimensional flame structure. Simple combustion modeling concepts that do not presume such a locally one-dimensional flame structure need to be developed.

As an initial step towards realizing this goal, a combined approach may be considered. More precisely, the flamelet model, which is capable of capturing main combustion features, can be used to describe the distribution of reactants and major products. In addition, concentrations of complex combustion products and intermediates can be used to represent local flow characteristics due to their high sensitivity to strains and flame curvature. Combining flamelet-predicted major species and several constrained critical intermediates, Rate-Controlled Constrained-Equilibrium (RCCE) [201] calculations can be performed to generate the database for chemistry tabulation, later used in flow simulations. This combined flamelet-RCCE approach would present a necessary first step towards reacting flow modeling without presuming local flame structures.

Appendix A

Modified flamelet equations on the centerline of axisymmetric laminar co-flow diffusion flames

Using the continuity equation (Eq 2.1), the transport equations for mixture fraction (Eq. 2.6) and species mass fractions (Eq. 2.8), and the boundary conditions on the centerline (Eq. 3.9), the complete modified flamelet equations used in Chapter 3 for sooting tendency predictions are

$$\begin{aligned}
u\frac{\partial Z}{\partial x}\left(1-\frac{1}{Le_i}\right)\frac{\partial Y_i}{\partial Z} &= \frac{1}{2}\frac{\chi'}{Le_i}\frac{\partial^2 Y_i}{\partial Z^2}+\frac{\dot{\omega}_i}{\rho} \\
-u\frac{\partial Z}{\partial x}Y_i\frac{\partial}{\partial Z}\left(\sum_j\frac{Y_j}{Le_j}\right)-\frac{Y_i}{2}\chi'\frac{\partial^2}{\partial Z^2}\left(\sum_j\frac{Y_j}{Le_j}\right) & \\
+\frac{1}{2Le_i}\frac{Y_i}{W}\chi'\frac{\partial^2 W}{\partial Z^2}-\frac{1}{2}\frac{Y_i}{W}\left(\sum_j\frac{Y_j}{Le_j}\right)\chi'\frac{\partial^2 W}{\partial Z^2} & \\
+\frac{1}{Le_i}u\frac{\partial Z}{\partial x}\frac{Y_i}{W}\frac{\partial W}{\partial Z}-u\frac{\partial Z}{\partial x}\frac{\partial W}{\partial Z}\frac{Y_i}{W}\left(\sum_j\frac{Y_j}{Le_j}\right) & \\
+\frac{\chi'}{2Le_i}\frac{\partial W}{\partial Z}\frac{\partial}{\partial Z}\left(\frac{Y_i}{W}\right)-\frac{\chi'}{2}\frac{\partial W}{\partial Z}\frac{\partial}{\partial Z}\left(\frac{Y_i}{W}\sum_j\frac{Y_j}{Le_j}\right) &
\end{aligned} \tag{A.1}$$

These equations are obtained by recombining diffusion in ϕ with diffusion in Z. The resulting complete modified flamelet equations include the molar diffusion, mass correction, and molar correction terms, with the global aggregate scalar dissipation rate χ'.

Appendix B

Curved flamelet formulation

B.1 Detailed derivation of the flamelet equations including curvature effects

The transformation rules (Eq. 4.4) are applied to the species transport equations (Eq. 2.8).

The time-dependent term becomes

$$\rho\frac{\partial Y_i}{\partial t} = \rho\left(\frac{\partial Y_i}{\partial \tau} + \frac{\partial Y_i}{\partial Z}\frac{\partial Z}{\partial t} + \frac{\partial Y_i}{\partial Z_2}\frac{\partial Z_2}{\partial t} + \frac{\partial Y_i}{\partial Z_3}\frac{\partial Z_3}{\partial t}\right). \tag{B.1}$$

Using Eq. 4.5, the convection term is transformed to

$$\rho\mathbf{u}\cdot\nabla Y_i = \rho\mathbf{u}\cdot\left(\frac{\partial Y_i}{\partial Z}\nabla Z + \frac{\partial Y_i}{\partial Z_2}\nabla Z_2 + \frac{\partial Y_i}{\partial Z_3}\nabla Z_3\right) \tag{B.2}$$

The diffusion term can be split into two parts

$$\nabla\cdot\left(\rho\frac{D}{Le_i}\nabla Y_i\right) = \frac{\rho D}{Le_i}\nabla^2 Y_i + \frac{1}{Le_i}\nabla\left(\rho D\right)\cdot\nabla Y_i \tag{B.3}$$

By applying the Laplacian operator (Eq. 4.7) to Y_i, the first part becomes

$$\begin{aligned}\frac{\rho D}{Le_i}\nabla\cdot(\nabla Y_i) &= \frac{\rho D}{Le_i}\left(\frac{\partial^2 Y_i}{\partial Z^2}|\nabla Z|^2+\frac{\partial^2 Y_i}{\partial Z_2^2}|\nabla Z_2|^2+\frac{\partial^2 Y_i}{\partial Z_3^2}|\nabla Z_3|^2\right)\\ &+\frac{\rho D}{Le_i}\left(\frac{\partial Y_i}{\partial Z}\nabla^2 Z+\frac{\partial Y_i}{\partial Z_2}\nabla^2 Z_2+\frac{\partial Y_i}{\partial Z_3}\nabla^2 Z_3\right)\\ &+\frac{2\rho D}{Le_i}\frac{\partial^2 Y_i}{\partial Z_2\partial Z_3}(\nabla Z_2\cdot\nabla Z_3)\end{aligned} \tag{B.4}$$

Using the form of the gradient operator (Eq. 4.5), the second part becomes

$$\begin{aligned}\frac{1}{Le_i}\nabla(\rho D)\cdot\nabla Y_i &= \frac{1}{Le_i}\left(\frac{\partial\rho D}{\partial Z}\frac{\partial Y_i}{\partial Z}|\nabla Z|^2+\frac{\partial\rho D}{\partial Z_2}\frac{\partial Y_i}{\partial Z_2}|\nabla Z_2|^2+\frac{\partial\rho D}{\partial Z_3}\frac{\partial Y_i}{\partial Z_3}|\nabla Z_3|^2\right)\\ &+\frac{1}{Le_i}\left(\frac{\partial\rho D}{\partial Z_2}\frac{\partial Y_i}{\partial Z_3}+\frac{\partial\rho D}{\partial Z_3}\frac{\partial Y_i}{\partial Z_2}\right)(\nabla Z_2\cdot\nabla Z_3)\,.\end{aligned} \tag{B.5}$$

Therefore, the diffusion term becomes

$$\begin{aligned}\nabla\cdot\left(\rho\frac{D}{Le_i}\nabla Y_i\right) &= \frac{\rho D}{Le_i}\frac{\partial^2 Y_i}{\partial Z^2}|\nabla Z|^2+\frac{\rho D}{Le_i}\frac{\partial Y_i}{\partial Z}\nabla^2 Z+\frac{1}{Le_i}\frac{\partial\rho D}{\partial Z}\frac{\partial Y_i}{\partial Z}|\nabla Z|^2\\ &+\frac{\rho D}{Le_i}\left(\frac{\partial Y_i}{\partial Z_2}\nabla^2 Z_2+\frac{\partial Y_i}{\partial Z_3}\nabla^2 Z_3\right)\\ &+\frac{2\rho D}{Le_i}\frac{\partial^2 Y_i}{\partial Z_2\partial Z_3}(\nabla Z_2\cdot\nabla Z_3)\\ &+\frac{1}{Le_i}\left(\frac{\partial\rho D}{\partial Z_2}\frac{\partial Y_i}{\partial Z_2}|\nabla Z_2|^2+\frac{\partial\rho D}{\partial Z_3}\frac{\partial Y_i}{\partial Z_3}|\nabla Z_3|^2\right)\\ &+\frac{1}{Le_i}\left(\frac{\partial\rho D}{\partial Z_2}\frac{\partial Y_i}{\partial Z_3}+\frac{\partial\rho D}{\partial Z_3}\frac{\partial Y_i}{\partial Z_2}\right)(\nabla Z_2\cdot\nabla Z_3)\\ &+\frac{\rho D}{Le_i}\left(\frac{\partial^2 Y_i}{\partial Z_2^2}|\nabla Z_2|^2+\frac{\partial^2 Y_i}{\partial Z_3^2}|\nabla Z_3|^2\right)\end{aligned} \tag{B.6}$$

The second and third terms on the right hand side of the above equation can be regrouped as

$$\begin{aligned}\frac{\rho D}{Le_i}\frac{\partial Y_i}{\partial Z}\nabla^2 Z+\frac{1}{Le_i}\frac{\partial\rho D}{\partial Z}\frac{\partial Y_i}{\partial Z}|\nabla Z|^2 &= \frac{1}{Le_i}\frac{\partial Y_i}{\partial Z}\left(\rho D\nabla^2 Z+\frac{\partial\rho D}{\partial Z}(\nabla Z\cdot\nabla Z)\right)\\ &= \frac{1}{Le_i}\frac{\partial Y_i}{\partial Z}\left(\rho D\nabla^2 Z+\nabla(\rho D)\cdot\nabla Z\right)\\ &= \frac{1}{Le_i}\frac{\partial Y_i}{\partial Z}\nabla\cdot(\rho D\nabla Z)\end{aligned} \tag{B.7}$$

Similarly, The following terms on the right hand side of Eq. B.6 can be recombined as

$$
\begin{aligned}
& \frac{\rho D}{Le_i}\left(\frac{\partial Y_i}{\partial Z_2}\nabla^2 Z_2+\frac{\partial Y_i}{\partial Z_3}\nabla^2 Z_3\right) \\
& +\frac{1}{Le_i}\left(\frac{\partial \rho D}{\partial Z_2}\frac{\partial Y_i}{\partial Z_3}+\frac{\partial \rho D}{\partial Z_3}\frac{\partial Y_i}{\partial Z_2}\right)(\nabla Z_2\cdot\nabla Z_3) \\
& +\frac{1}{Le_i}\left(\frac{\partial \rho D}{\partial Z_2}\frac{\partial Y_i}{\partial Z_2}|\nabla Z_2|^2+\frac{\partial \rho D}{\partial Z_3}\frac{\partial Y_i}{\partial Z_3}|\nabla Z_3|^2\right) \qquad \text{(B.8)} \\
= \quad & +\frac{1}{Le_i}\left(\rho D\frac{\partial Y_i}{\partial Z_2}\nabla^2 Z_2+(\nabla Z_2\cdot\nabla Z_3)\frac{\partial \rho D}{\partial Z_3}\frac{\partial Y_i}{\partial Z_2}+\frac{\partial \rho D}{\partial Z_2}\frac{\partial Y_i}{\partial Z_2}|\nabla Z_2|^2\right) \\
& +\frac{1}{Le_i}\left(\rho D\frac{\partial Y_i}{\partial Z_3}\nabla^2 Z_3+(\nabla Z_2\cdot\nabla Z_3)\frac{\partial \rho D}{\partial Z_2}\frac{\partial Y_i}{\partial Z_3}+\frac{\partial \rho D}{\partial Z_3}\frac{\partial Y_i}{\partial Z_3}|\nabla Z_3|^2\right) \\
= \quad & \frac{1}{Le_i}\nabla\cdot(\rho D\nabla Z_2)\frac{\partial Y_i}{\partial Z_2}+\frac{1}{Le_i}\nabla\cdot(\rho D\nabla Z_3)\frac{\partial Y_i}{\partial Z_3} \qquad \text{(B.9)}
\end{aligned}
$$

Combining the different terms and using the transport equation for mixture fraction (Eq. 2.6), one obtains the flamelet equations in its final form

$$
\begin{aligned}
& \rho\frac{\partial Y_i}{\partial \tau}+\underbrace{\rho\sum_{k=2}^{3}\left[\frac{\partial Y_i}{\partial Z_k}\left(\frac{\partial Z_k}{\partial t}+\mathbf{u}\cdot\nabla Z_k\right)\right]}_{\text{Lagrangian transport } L_t} \\
& +\underbrace{\left(1-\frac{1}{Le_i}\right)\nabla\cdot(\rho D\nabla Z)\frac{\partial Y_i}{\partial Z}}_{\text{Convection in mixture fraction } C_Z} \\
= \quad & +\underbrace{\frac{\rho\chi}{2Le_i}\frac{\partial^2 Y_i}{\partial Z^2}}_{\text{Normal diffusion } D_Z}+\dot{\omega}_i \\
& +\underbrace{\sum_{k=2}^{3}\frac{\rho\chi_k}{2Le_i}\frac{\partial^2 Y_i}{\partial Z_k^2}+\frac{2\rho D}{Le_i}(\nabla Z_2\cdot\nabla Z_3)\frac{\partial^2 Y_i}{\partial Z_2\partial Z_3}}_{\text{Tangential diffusion } D_t} \\
& +\underbrace{\frac{1}{Le_i}\nabla\cdot(\rho D\nabla Z_2)\frac{\partial Y_i}{\partial Z_2}+\frac{1}{Le_i}\nabla\cdot(\rho D\nabla Z_3)\frac{\partial Y_i}{\partial Z_3}}_{\text{Tangential convection } C_t} \\
& +\underbrace{\nabla\cdot(\rho Y_i\mathbf{V_{c,i}})}_{\text{Correction terms } R} \qquad \text{(B.10)}
\end{aligned}
$$

where χ and χ_k are defined in Eq. 4.9.

B.2 Comparisons with the flamelet equations proposed by Williams

In the limit of unity Lewis numbers, Williams proposed to rewrite the species transport equations with respect to mixture fraction [52]. These equations take the following form

$$\begin{aligned} & \rho\frac{\partial Y_i}{\partial t} + \rho\mathbf{u}_\perp \cdot \nabla_\perp Y_i \\ = \; & \dot{\omega}_i + \underbrace{\rho D|\nabla Z|^2 \frac{\partial^2 Y_i}{\partial Z^2}}_{\text{Normal diffusion } D_Z} + \nabla_\perp \cdot (\rho D \nabla_\perp Y_i) - \rho D \nabla_\perp (\ln|\nabla Z|) \cdot \nabla_\perp Y_i, \end{aligned} \tag{B.11}$$

where the subscript $\perp$ denotes components in the plane normal to the mixture fraction Z direction. More precisely,

$$\begin{aligned} \nabla_\perp s &= \nabla s - \frac{\partial s}{\partial Z}\nabla Z, \\ \nabla_\perp . \mathbf{v} &= \nabla \cdot \mathbf{v} - \frac{\partial \mathbf{v}}{\partial Z} \cdot \nabla Z, \\ \mathbf{u}_\perp &= \mathbf{u} - \mathbf{u} \cdot \nabla Z, \end{aligned} \tag{B.12}$$

where s represents an arbitrary scalar, $\mathbf{v}$ represents an arbitrary vector, and $\mathbf{u}$ is the velocity vector.

Under unity Lewis number assumption, the above the flamelet formulation proposed by Williams is equivalent to the currently proposed flamelet formulation. In this limit, Eq. 4.8 simplifies to

$$\begin{aligned} & \rho\frac{\partial Y_i}{\partial \tau} + \underbrace{\rho \sum_{k=2}^{3} \left[\frac{\partial Y_i}{\partial Z_k} \left(\frac{\partial Z_k}{\partial t} + \mathbf{u} \cdot \nabla Z_k \right) \right]}_{\text{Lagrangian transport } L_t} \\ = \; & \underbrace{\frac{\rho\chi}{2}\frac{\partial^2 Y_i}{\partial Z^2}}_{\text{Normal diffusion } D_Z} + \dot{\omega}_i \\ & + \underbrace{\sum_{k=2}^{3} \frac{\rho\chi_k}{2}\frac{\partial^2 Y_i}{\partial Z_k^2} + 2\rho D(\nabla Z_2 \cdot \nabla Z_3)\frac{\partial^2 Y_i}{\partial Z_2 \partial Z_3}}_{\text{Tangential diffusion } D_t} \\ & + \underbrace{\nabla \cdot (\rho D \nabla Z_2)\frac{\partial Y_i}{\partial Z_2} + \nabla \cdot (\rho D \nabla Z_3)\frac{\partial Y_i}{\partial Z_3}}_{\text{Tangential convection } C_t}. \end{aligned} \tag{B.13}$$

In Eq. B.11, the normal diffusion term D_Z takes the same form as in the currently proposed flamelet equations (Eq. B.13). Explicit connections can be made for the other terms between Eq. B.13 and Williams' flamelet formulation (Eq. B.11). The first two terms on the LHS of Eq. B.11 corresponds to the flamelet unsteady term (First on the LHS of Eq. B.13) and the Lagrangian transport term L_t (Williams omitted the time dependence of tangential coordinates Z_2 and Z_3).

The third term on the RHS of Eq. B.11 can be expanded as

$$\begin{aligned}
\nabla_\perp \cdot (\rho D \nabla_\perp Y_i) &= \nabla \cdot (\rho D \frac{\partial Y_i}{\partial Z_2} \nabla Z_2 + \rho D \frac{\partial Y_i}{\partial Z_3} \nabla Z_3) - \nabla Z \cdot \frac{\partial}{\partial Z} (\rho D \nabla_\perp Y_i) \\
&= \underbrace{\nabla \cdot (\rho D \nabla Z_2) \frac{\partial Y_i}{\partial Z_2} + \nabla \cdot (\rho D \nabla Z_2) \frac{\partial Y_i}{\partial Z_2}}_{\text{Tangential convection } C_t} \\
&\quad \underbrace{+ \sum_{k=2}^{3} \frac{\rho \chi_k}{2} \frac{\partial^2 Y_i}{\partial Z_k^2} + 2\rho D (\nabla Z_2 \cdot \nabla Z_3) \frac{\partial^2 Y_i}{\partial Z_2 \partial Z_3}}_{\text{Tangential diffusion } D_t} \\
&\quad \underbrace{- \nabla Z \cdot \frac{\partial}{\partial Z} (\rho D \nabla_\perp Y_i)}_{F} .
\end{aligned} \tag{B.14}$$

This term contains both the tangential diffusion D_t and the tangential convection C_t and an additional term F.

The last term on the RHS of Eq. B.11 can be rewritten as

$$\begin{aligned}
-\rho D \nabla_\perp (\ln |\nabla Z|) \cdot \nabla_\perp Y_i &= -\rho D \nabla (\ln |\nabla Z|) \cdot \nabla_\perp Y_i \\
&= -\rho D \frac{1}{2} \left[\nabla \left(\ln (\nabla Z \cdot \nabla Z) \right) \right] \cdot (\nabla_\perp Y_i) \\
&= -\frac{\rho D}{2} \left[\frac{\nabla \left((\nabla Z \cdot \nabla Z) \right)}{|\nabla Z|^2} \right] \cdot (\nabla_\perp Y_i) \\
&= -\rho D \frac{\partial}{\partial Z} (\nabla Z) \cdot (\nabla_\perp Y_i) \\
&= \nabla Z \cdot \frac{\partial}{\partial Z} (\rho D \nabla_\perp Y_i) .
\end{aligned} \tag{B.15}$$

This term compensates exactly the additional term F found in Eq. B.14.

The current form of the flamelet equations, equivalent to Williams' formulation, is preferred since the effects of the different processes can be explicitly identified.

B.3 The complete curved flamelet equations

The complete one-dimensional steady-state laminar diffusion flamelet equations including curvature effects are given by

$$\begin{aligned}
\mathbf{u}\cdot\nabla Z\left(1-\frac{1}{Le_i}\right)\frac{\partial Y_i}{\partial Z} &= \frac{1}{2}\frac{\chi}{Le_i}\frac{\partial^2 Y_i}{\partial Z^2}+\frac{\dot{\omega}_i}{\rho}\\
-\mathbf{u}\cdot\nabla Z Y_i\frac{\partial}{\partial Z}\left(\sum_j\frac{Y_j}{Le_j}\right) &- \frac{Y_i}{2}\chi\frac{\partial^2}{\partial Z^2}\left(\sum_j\frac{Y_j}{Le_j}\right)\\
+\frac{1}{2Le_i}\frac{Y_i}{W}\chi\frac{\partial^2 W}{\partial Z^2} &- \frac{1}{2}\frac{Y_i}{W}\left(\sum_j\frac{Y_j}{Le_j}\right)\chi\frac{\partial^2 W}{\partial Z^2}\\
+\frac{1}{Le_i}\mathbf{u}\cdot\nabla Z\frac{Y_i}{W}\frac{\partial W}{\partial Z} &- \mathbf{u}\cdot\nabla Z\frac{\partial W}{\partial Z}\frac{Y_i}{W}\left(\sum_j\frac{Y_j}{Le_j}\right)\\
+\frac{\chi}{2Le_i}\frac{\partial W}{\partial Z}\frac{\partial}{\partial Z}\left(\frac{Y_i}{W}\right) &- \frac{\chi}{2}\frac{\partial W}{\partial Z}\frac{\partial}{\partial Z}\left(\frac{Y_i}{W}\sum_j\frac{Y_j}{Le_j}\right).
\end{aligned} \tag{B.16}$$

In the above equation, $\mathbf{u}\cdot\nabla Z$ is calculated as

$$\mathbf{u}\cdot\nabla Z=\frac{1}{4\rho}\left(\frac{\partial\rho\chi}{\partial Z}+\frac{\chi}{D}\frac{\partial\rho D}{\partial Z}\right)+\kappa\sqrt{\frac{\chi D}{2}}. \tag{B.17}$$

Appendix C

Review of the derivation of flamelet equations including curvature effects

The steady-state flamelet model [49, 50] has been a popular modeling approach in simulating both laminar and turbulent non-premixed flames. The three substantial simplifications made by the flamelet model are that combustion takes place in a thin layer close to the flame front, diffusion in the direction parallel to the local iso-surface of mixture fraction is negligible, and the local flame surfaces are essentially flat [24]. Recently, Kortschik *et al.* proposed a new derivation of the flamelet equations with the goal of capturing the effects of flame curvature [73]. Unfortunately, several subtle inconsistencies arise in the derivation. Very recently, Xu *et al.* re-derived the flamelet equations considering curvature effects and partially addressed these inconsistencies [75]. The objective of this work is to formally identify these inconsistencies.

C.1 Galilean transformation

The coordinate transformation used in [73] and in [75] is the same and is composed of two steps. In the first step, the initial Cartesian system (X_1, X_2, X_3) is rotated in such a way that the new coordinate x_1 is normal to the mixture fraction iso-surface. Consequently, the new coordinates x_2 and x_3 lie in the plane tangent to the local mixture fraction iso-surface. In the second step, the x_1 coordinate is replaced by the mixture fraction and the other two coordinates are left unchanged.

The first inconsistency is related to the first coordinate change, namely the rotation. In itself, this coordinate transformation used by both authors is appropriate (as long as the transformation Jacobian is non-zero, *i.e.* $\partial Z/\partial x_1 \neq 0$). However, Kortschik *et al.* further assume that "the coordinate x_1 is normal to the local mixture fraction iso-surface" (page 148 of [73]). Making this assumption at *every point* in the domain implies that the first transformation is not a Galilean transformation. For reference, a Galilean transformation is a transformation between two reference frames that corresponds to a *constant relative motion* between these frames. This is equivalent to saying the entire space is rotated *all at once*. In other words, every point in the domain has the *exact same* x_1, x_2, and x_3 axes.

As every point along an iso-surface of mixture fraction does not have the same x_1 axis (*i.e.* they do not have the same normal directions), then the first transformation (used by Kortschik *et al.*) is not Galilean. This conflicts with the expression used for the species transport equations (Eq. 5 in [73]) as gradient and divergence operators are written using only the $\partial/\partial x_1$, $\partial/\partial x_2$, and $\partial/\partial x_3$ terms. Using a frame of reference that rotates with the flame (*i.e.* not a Galilean transformation) is mathematically possible, but additional terms would need to be added to these transport equations. This is analogous to what happens when changing from a Cartesian coordinate frame to a polar, cylindrical, or spherical coordinate frame (*i.e.* new terms in $1/r$ are introduced).

In summary, the various assumptions made by Kortschik *et al.* about the change of coordinates assumes *implicitly* there is no curvature, *i.e.* the flame is flat. Only under this condition, can the x_1 axis be both the same everywhere in the domain and perpendicular to the mixture fraction iso-surface.

In the more recent work by Xu *et al.*, the authors made a similar assumption of alignment between the x_1 axis and the gradient of mixture fraction (see for instance Eq. A.26 in [75]). However, the major difference is that their flamelet equations were obtained by considering flamelets *on the axis* of an axisymmetric case. Since these flamelets are located directly on the x_1 axis and x_1 is always perpendicular to the mixture fraction iso-surface for every point of these flamelets, then the condition of alignment is always fulfilled (see Fig. 3 in [75]). Unfortunately, this also means that their flamelet

equations are only valid on the axis of symmetry.

C.2 Coordinate transformation rules

After the first coordinate transformation (*i.e.* the rotation), the x_1 coordinate is replaced by the mixture fraction, while the other two coordinates are left unchanged,

$$x_1 \to Z(x_1, x_2, x_3), \quad x_2 = Z_2, \quad x_3 = Z_3\,. \tag{C.1}$$

corresponding to Eq. 13 in [73] and Eq. A.4 in [75]. This coordinate transformation leads to the following rules for derivative changes (Eq. 14 in [73] and Eq. A.5-8 in [75]),

$$\begin{aligned}
\left.\frac{\partial}{\partial x_1}\right|_{x_2,x_3} &= \frac{\partial Z}{\partial x_1}\cdot\left.\frac{\partial}{\partial Z}\right|_{Z_2,Z_3}, \\
\left.\frac{\partial}{\partial x_2}\right|_{x_1,x_3} &= \frac{\partial Z}{\partial x_2}\cdot\left.\frac{\partial}{\partial Z}\right|_{Z_2,Z_3} + \left.\frac{\partial}{\partial Z_2}\right|_{Z_1,Z_3}, \\
\left.\frac{\partial}{\partial x_3}\right|_{x_1,x_2} &= \frac{\partial Z}{\partial x_3}\cdot\left.\frac{\partial}{\partial Z}\right|_{Z_2,Z_3} + \left.\frac{\partial}{\partial Z_3}\right|_{Z_1,Z_2}.
\end{aligned} \tag{C.2}$$

The subscripts imply that the partial derivatives are taken while the other variables are held constant. These equations state that, although $Z_2 = x_2$, the *partial* derivatives with respect to Z_2 and x_2 are not equal because the other variables (held constant) are not the same. Only the *differentials* are the same, *i.e.* $dZ_2 = dx_2$.

The second mathematical error of Kortschik *et al.* follows from the above expressions and is located in Eq. 16 of their original paper [73]. Following the above transformation rules, which are the same as in the original paper, the partial derivatives in Z_k and x_k are not exchangeable. In other words, the left hand side of Eq. 16 in [73] is not equal to its middle side. Instead, Eq. 16

should be replaced by

$$\begin{aligned}\sum_{k=2}^{3}\frac{\partial^2 Y}{\partial x_k^2} &= \sum_{k=2}^{3}\frac{\partial^2 Y}{\partial Z_k^2} \\ &+\sum_{k=2}^{3}\left(\frac{\partial Z}{\partial x_k}\right)^2\frac{\partial^2 Y}{\partial Z^2}+\sum_{k=2}^{3}\left(\frac{\partial^2 Z}{\partial {x_k}^2}\right)\frac{\partial Y}{\partial Z} \\ &+\sum_{k=2}^{3}\left(\frac{\partial Z}{\partial x_k}\frac{\partial Z_2}{\partial x_k}\right)\frac{\partial^2 Y}{\partial Z\partial Z_2}+\sum_{k=2}^{3}\left(\frac{\partial Z}{\partial x_k}\frac{\partial Z_3}{\partial x_k}\right)\frac{\partial^2 Y}{\partial Z\partial Z_3}\end{aligned} \tag{C.3}$$

The additional terms appearing in the above equation and missing from Eq. 16 in [73] are the same terms that are present in Eq. 15 of [73], *i.e.* tangential diffusion (second term on the RHS), tangential convection (third term), and cross-diffusion (last two terms). Clearly, Eq. 16 in its original form is not valid. Unfortunately, as a direct consequence, the derivation that follows from it is not valid either.

This shortcoming present in the work of Kortschik *et al.* was addressed in the recent formulation of Xu *et al.* [75].

C.3 One-dimensionality

The third inconsistency resides in the *implicit* assumption of one-dimensionality of the flamelet equations. This is illustrated by writing the final flamelet equations as a function of a single variable, the mixture fraction (see Eq. 23 in [73] and Eq. 21 in [75]). In other words, all variables can be written as $Y_i = Y_i(Z)$.

A trivial consequence of this dependence is that the species mass fractions are not a function of the other two coordinates, namely Z_2 and Z_3. Therefore, the fifth term in Eq. 15 in the work of Kortschik *et al.* [73], which only involves these two variables, is identically zero. As this term encompasses all curvature effects, then curvature effects are non-existent.

Xu *et al.* made a similar inconsistency in their derivation of the curved flamelet equations. In their final forms, the flamelet equations (Eq. 21 and 22 in [75]) contain the difference between two curvature terms, namely κ_Z and $\hat{\kappa}_i$. Under the assumption of one-dimensionality, *i.e.* the species

mass fractions are only a function of mixture fraction, then it can be shown that the mixture fraction curvature (κ_Z) and the species mass fraction curvature (κ_i) are identical.

$$\kappa_i = -\nabla \cdot \left(\frac{\nabla Y_i}{|\nabla Y_i|} \right) = -\nabla \cdot \left(\frac{\frac{dY_i}{dZ}\nabla Z}{|\frac{dY_i}{dZ}|\,|\nabla Z|} \right) = \pm\nabla \cdot \left(\frac{\nabla Z}{|\nabla Z|} \right) = \pm\kappa_Z \tag{C.4}$$

The $\pm$ comes from the sign of the derivative of the species mass fraction with respect to mixture fraction and is the reason why Xu *et al.* introduced the modified curvature, $\hat{\kappa}_i$. The above equation shows that the second term on the right hand side of Eq. 22 in [75] is identically zero. This result comes from the one-dimensionality of the flamelet equations and is independent of the values of the species Lewis numbers.

C.4 Tangential diffusion

Regardless of the one-dimensionality of the flamelet equations, it is interesting to investigate further the term referred to as fc_1 in Eq. 21 in the recent work of Xu *et al.* [75]. This term is equivalent to the $CT1$ term in Eq. A.25 of [75]. First, it should be noted that this expression (Eq. A.25) is not an approximation (as stated in the original paper), but an exact equation due to the axi-symmetry of the configuration investigated (see section 1).

Second, Xu *et al.* rightfully refer to the fc_1 term as "tangential diffusion". Nevertheless, the reader might be confused by the final form of this term as a diffusion term usually refers to a second order derivative, while the fc_1 term only involves first order derivative of the species mass fraction. The diffusion nature of this term and more importantly its *tangential* property are more easily described by considering a different coordinate system.

We consider a curvilinear coordinate transformation where the Z_2 and Z_3 coordinates lie *within* the iso-contour of mixture fraction (see Fig. 4.1). With such transformation and utilizing the axi-symmetry of the configuration, one can show that the two terms on the final right hand side of

Eq. A.25 in [75] are related. In two dimensions, this gives exactly

$$\frac{\partial^2 Y_i}{\partial x_2^2} = |\nabla Z_2|^2 \frac{\partial^2 Y_i}{\partial Z_2^2} + \nabla^2 Z \frac{\partial Y_i}{\partial Z} = |\nabla Z_2|^2 \frac{\partial^2 Y_i}{\partial Z_2^2} - \kappa_Z |\nabla Z| \frac{\partial Y_i}{\partial Z}. \tag{C.5}$$

By combining the above expression with Eq. A.25 in [75], one can show that the fc_1 term takes the form (again in two dimensions)

$$fc_1 = |\nabla Z_2|^2 \frac{\partial^2 Y_i}{\partial Z_2^2}. \tag{C.6}$$

In this form, it is clear that the fc_1 term corresponds to a diffusion process in the tangential direction, *i.e.* in the direction perpendicular to the gradient of mixture fraction. We also see that the difference of the two curvature terms (κ_i and κ_Z) drops out.

C.5 Summary

In summary, after identifying these various inconsistencies, the only mathematically correct form of Eq. 23 in [73] or Eq. 22 in [75] in the limit of unity Lewis numbers is given by

$$\rho \frac{\partial Y_i}{\partial \tau} = \frac{\rho \chi}{2} \frac{\partial^2 Y_i}{\partial Z^2} + \dot{\omega}_i \,, \tag{C.7}$$

which is the original flamelet equation derived by Peters [49, 50]. The above results suggest that, under the assumption of a thin flame, curvature does not have any effects on the flamelet solution when unity Lewis number is assumed [24].

It is important to note that the above derivations do not invalidate in any way the experimental work presented in Kortschik *et al.* [73]. The major assumption used to derive the flamelet equation in [73] is that the flame is *thin*. This is clearly not the case for the experimental work reported therein. Consider the mixture fraction and formaldehyde-LIF images shown in Fig. 8 of [73] (top two images), the right-most circle highlights a region of high curvature. If the flame thickness is estimated either from the mixture fraction gradient or from the CH_2O profile, it would be found that the product of flame curvature by flame thickness is of order unity. Under these conditions, it is

difficult to argue that the flame is thin. Curvature effects might re-appear if the flamelet equations are re-derived *without* the assumption of thin flame [24].

Appendix D

Description of the simulation code: NGA

NGA is an extension of the high order conservative finite difference scheme initially developed by Morinishi *et al.* [99]. It allows for three-dimensional, variable-density turbulent flows to be simulated in complex geometries, which can be either cylindrical or cartesian, on uniform or non-uniform meshes [90]. It is discretely conservative of mass, momentum, and kinetic energy, and it can provide an arbitrarily high order of accuracy. The various variables are staggered both in space and time. All scalar quantities, such as the density, ρ, pressure, P, and species mass fractions, Y_i, are stored at the cell (volume) centers. The velocity components are stored at the faces of the cell volumes. An overview of the NGA code and the time marching procedure is provided here in support of the simulation data presented in this thesis.

D.1 Treatment of the convective and viscous terms

In the simulations performed using NGA, the convective term is discretized spatially with second order accuracy in all simulations performed in this thesis. Second order interpolation operators are applied when necessary (for instance when computing cell centered values from face values). The density field is limited to second-order interpolation in the discretization of the momentum equation, such that it is Total Variation Diminishing (TVD). Imposing a state of TVD prevents the density field from becoming unbounded, and ensures the simulations remain realizable. It should be stated

that the density interpolation is limited to second-order. When a study was performed, it was found that such a limitation had little effect on the quality of the results obtained [90].

As viscous terms are dissipative by nature, they are inherently more stable than the convective terms that were addressed previously. Accordingly, they are more easily discretized, and an approach based on Lagrange polynomials is applied. The operators that are necessary to discretize the viscous terms are different than those presented for the discretization of the convective terms, and these new operators are based on a local Lagrange polynomial representation of the quantity to which they are applied [90]. To develop an n^{th} order accurate interpolation and differentiation operator for a given quantity ϕ at a given location in a given direction, an $(n-1)^{\text{th}}$ order Lagrange polynomial is needed. This $(n-1)^{\text{th}}$ order Lagrange polynomial is fit through the n data points that are present in the stencil. As this fitting operation is centered about the point being evaluated, the interpolation or differentiation of the quantity ϕ is calculated from an equal number of points on either side of the point being evaluated. In the simulations performed in this thesis, second order discretization is used for viscous terms. A similar treatment is applied to the diffusive terms in the discretization of the scalar transport equations.

As a consequence of this discretization, mass, momentum, and the scalar quantity solved for through a scalar transport equation (without a source term) are discretely conserved.

D.2 Time-integration

An iterative procedure is applied to fully take into account the non-linearities in the Navier-Stokes equations. This iterative procedure has been found of critical importance for stability and accuracy considerations [90, 202, 203].

The numerical algorithmic sequence for one time step is described below, where a uniform time step Δt is employed. The density, pressure, and scalar fields are advanced from time level $t^{n+1/2}$ to $t^{n+3/2}$, and the velocity fields are advanced from time level t^n to t^{n+1}. A total number of Q sub-iterations is assumed.

0. Upon convergence of the previous time step, the density, $\rho^{n+1/2}$, pressure, $P^{n+1/2}$, velocity fields, $\mathbf{u}^n$, and scalar fields, $\mathbf{Y}^{n+1/2}$, are stored, where $\mathbf{Y}$ represents the vector of species mass fractions $(Y_1, ..., Y_N)$ (the reacting mixture is assumed to contain a total number of N species). These solutions are used as initial best guesses for the forthcoming iterative procedure

$$\rho_0^{n+3/2} = \rho^{n+1/2},\ P_0^{n+3/2} = P^{n+1/2},\ \mathbf{u}_0^{n+1} = \mathbf{u}^n,\ \text{and}\ \mathbf{Y}_0^{n+3/2} = \mathbf{Y}^{n+1/2}, \tag{D.1}$$

where the subscript indicates the index of the sub-iteration. The vector of chemical source terms is denoted by $\mathbf{\Omega} = (\dot{\omega}_1, ..., \dot{\omega}_N)$, and $\mathbf{\Omega}_0^{n+3/2}$ is evaluated using the thermochemical quantities obtained at the conclusion of the previous time step.

For the sub-iteration $k = 1, \ldots, Q$

1. The scalar fields are advanced in time using the semi-implicit Crank-Nicolson method [90, 203] for the convective and diffusive terms, and explicit integration for the chemical source terms

$$\mathbf{Y}_k^* = \frac{\mathbf{Y}^{n+1/2} + \mathbf{Y}_{k-1}^{n+3/2}}{2}, \tag{D.2}$$

$$\begin{aligned} \rho_{k-1}^{n+3/2}\mathbf{Y}_k^{n+3/2} &= \rho^{n+1/2}\mathbf{Y}^{n+1/2} + \Delta t \cdot \left[\left(\mathbf{C}_k^{n+1} + \mathbf{D}_k^{n+1}\right) \cdot \mathbf{Y}_k^* + \mathbf{\Omega}_k^*\right] \\ &+ \frac{\Delta t}{2}\left(\frac{\partial \mathbf{C}}{\partial \mathbf{Y}} + \frac{\partial \mathbf{D}}{\partial \mathbf{Y}}\right)_k^{n+1} \cdot \left(\mathbf{Y}_k^{n+3/2} - \mathbf{Y}_{k-1}^{n+3/2}\right). \end{aligned} \tag{D.3}$$

To simplify the discrete notations for spatial differential operators, the operators corresponding to the convective and diffusive terms in the scalar equations (Eq. 2.8) are written as $\mathbf{C}$ and $\mathbf{D}$, respectively. The symbolic operators $\frac{\partial \mathbf{C}}{\partial \mathbf{Y}}$ and $\frac{\partial \mathbf{D}}{\partial \mathbf{Y}}$ denotes the Jacobian matrices corresponding to the convective and diffusive terms, respectively. Depending on the order of discretization, these operators are generally banded diagonal matrices (*e.g.* tri-diagonal for 2^{nd} order discretization and penta-diagonal for 4^{th} order discretization). It is important to note that the semi-implicit Crank-Nicolson method proposed by Pierce and Moin [203] is not applied to the time-integration of the species chemical source terms, Ω_k^*. This is due to the extremely high

computational cost associated with the calculation of the chemical Jacobian matrix, $\left(\frac{\partial \boldsymbol{\Omega}}{\partial \mathbf{Y}}\right)_k^{n+1}$, and the even more expensive inversion of this matrix. The temperature equation (Eq. 2.4) is advanced in time in the exact same fashion as the species mass fractions at the same time, the discretized temperature equation is not shown for clarity.

2. The density field is predicted from thermodynamics using

$$\rho_k^{n+3/2} = \frac{P_0 \cdot \left(\sum_{i=1}^{N} \frac{Y_{i,k}^{n+3/2}}{W_i}\right)^{-1}}{\widehat{R} T_k^{n+3/2}}. \tag{D.4}$$

It is important to note that this density evaluation does not ensure primary conservation, since no density rescaling such as the one proposed by Shunn *et al.* [202] is used. However, upon convergence of the sub-iterations, this formulation is equivalent to the density treatment proposed by Shunn *et al.*.

3. The momentum equation is advanced in time using the same semi-implicit Crank-Nicolson method as for the scalar fields

$$\mathbf{u}_k^* = \frac{\mathbf{u}^n + \mathbf{u}_{k-1}^{n+1}}{2}, \tag{D.5}$$

$$\begin{aligned} \frac{\rho^{n+1/2} + \rho_k^{n+3/2}}{2} \mathbf{u}_k^{n+1} &= \frac{\rho^{n-1/2} + \rho^{n+1/2}}{2} \mathbf{u}^n + \Delta t \cdot \left[\left(\mathbf{C}_{\rho,k}^{n+1/2} + \mathbf{D}_{\rho,k}^{n+1/2} \right) \cdot \mathbf{u}_k^* + \nabla p_{k-1}^{n+3/2} \right] \\ &+ \frac{\Delta t}{2} \left(\frac{\partial \mathbf{C}_\rho}{\partial \mathbf{u}} + \frac{\partial \mathbf{D}_\rho}{\partial \mathbf{u}} \right)_k^{n+1/2} \cdot \left(\mathbf{u}_k^{n+1} - \mathbf{u}_{k-1}^{n+1} \right). \end{aligned} \tag{D.6}$$

4. A Poisson equation is then solved for the fluctuating hydrodynamic pressure

$$\nabla^2 \delta p_k^{n+3/2} = \frac{1}{\Delta t} \left[\nabla \cdot \left(\frac{\rho^{n+1/2} + \rho_k^{n+3/2}}{2} \mathbf{u}_k^{n+1} \right) + \frac{\rho_k^{n+3/2} - \rho^{n+1/2}}{\Delta t} \right] \tag{D.7}$$

The Poisson equation is solved using the high-fidelity HYPRE package [90, 204]. The predicted

velocity field is then updated through a projection step

$$\mathbf{u}_k^{n+1} = \mathbf{u}_k^{n+1} - \frac{2\Delta t}{\rho^{n+1/2} + \rho_k^{n+3/2}} \cdot \left[\nabla \left(\delta p_k^{n+3/2} - \delta p_{k-1}^{n+3/2}\right)\right]. \tag{D.8}$$

Convergence achieved after Q sub-iterations ($\phi_Q - \phi_{Q-1} \to 0$, where ϕ represents any flow and thermochemical variable at the current time level).

7. Upon convergence of the sub-iterations, the new solutions are updated

$$\rho^{n+3/2} = \rho_Q^{n+3/2},\ P^{n+3/2} = P_Q^{n+3/2},\ \mathbf{u}^{n+1} = \mathbf{u}_Q^{n+1},\ \text{and}\ \mathbf{Y}^{\mathrm{n+3/2}} = \mathbf{Y}_{\mathrm{Q}}^{\mathrm{n+3/2}}. \tag{D.9}$$

The above iterative time-marching scheme has been used for both laminar and turbulent flow modeling [8, 15, 42, 22]. It is important to note that the above formulation becomes equivalent to the fully-implicit Crank-Nicolson time-integration scheme upon convergence of the sub-iterations [203].

Appendix E

Description of the FlameMaster code

The FlameMaster code is a program designed to solve numerically typical problems found in combustion processes. Several different configurations are supported such as computations of homogeneous ignition delay times, laminar burning velocities, premixed flames, or counterflow diffusion flames. The following description provides an overview of the configurations and the equations solved.

E.1 General Description

The FlameMaster code relies on detailed chemical mechanisms to solve the different combustion problems. These chemical mechanisms are composed of thermodynamic and transport properties for each species in the system and a list of reactions among these species.

E.1.1 Thermodynamic Properties

The thermodynamic properties for agiven species at a given temperature T, such as heat capacity ($C_p(T)$), enthalpy content ($H(T)$), and entropy ($S(T)$), are evaluated by polynomial interpolation as follows

$$\frac{C_p(T)}{R} = a_1 + a_2 T + a_3 T^2 + a_4 T^3 + a_5 T^4 \tag{E.1}$$

$$\frac{H(T)}{R} = a_1 + \frac{a_2}{2} T + \frac{a_3}{3} T^2 + \frac{a_4}{4} T^3 + \frac{a_5}{5} T^4 + \frac{a_6}{T} \tag{E.2}$$

$$\frac{S(T)}{R} = a_1 \ln T + a_2 T + \frac{a_3}{2} T^2 + \frac{a_4}{3} T^3 + \frac{a_5}{4} T^4 + a_7 \tag{E.3}$$

where R is the universal gas constant. The seven parameters (a_1 to a_7) are constant and are different for different species. To improve the quality of the polynomial fit, two sets of parameters are used. The first set is used for low temperatures ($1000\,\mathrm{K} > T$) and the second set for high temperatures ($T > 1000\,\mathrm{K}$).

E.1.2 Reaction Rates

Suppose the following reaction

$$\sum_{j=1}^{n} \nu_{ij}\, \mathrm{S_j} \leftrightarrows \sum_{j=1}^{n} \nu_{ij}^{'}\, \mathrm{S_j}\,, \tag{E.4}$$

where $\mathrm{S_j}$ is the j-th species in the system and ν_{ij} is the stoichiometric coefficient for species j in reaction i. For a given reaction, the rate constant of the reaction is expressed in the modified Arrhenius form which describes its temperature dependence

$$k_i(T) = A_i T^{n_i} \exp\left(-\frac{E_i}{RT}\right). \tag{E.5}$$

The reaction rate is simply evaluated from the forward (k_{if}) and backward (k_{ib}) rate constants as

$$\omega_i = k_{if} \prod_{j=1}^{n} \left(\frac{\rho Y_j}{W_j}\right)^{\nu_{ij}} - k_{ib} \prod_{j=1}^{n} \left(\frac{\rho Y_j}{W_j}\right)^{\nu_{ij}^{'}}, \tag{E.6}$$

where ρ is the density and Y_j and W_j are the mass fraction and the molecular weight of species j, respectively.

E.1.3 Transport Properties

The diffusion velocity is decomposed into three parts

$$v_j = v_j^D + v_j^T + v_c \tag{E.7}$$

where v_j^D is the molecular diffusion, v_j^T is the thermal diffusion (Soret effect), and v_c is the velocity correction (the same value for each species). The molecular diffusion takes the following form

$$v_j^D = -\frac{D_j}{X_j}\nabla X_j \tag{E.8}$$

where X_j is the mole fraction of species j and D_j is the average diffusion coefficient of species j in the mixture. This coefficient is evaluated from the binary diffusion coefficient as

$$D_j = \frac{1 - \sum_{k=1}^{n} Y_k}{\sum_{k \neq j} \frac{X_k}{D_{jk}}} \tag{E.9}$$

In order to conserve mass, the total mass flux due to diffusion should be exactly zero

$$\sum_{j=1}^{n} Y_j v_j = 0\,. \tag{E.10}$$

This condition is ensured by defining the velocity correction as

$$v_c = -\sum_{j=1}^{n} Y_j \cdot (v_j^D + v_j^T)\,. \tag{E.11}$$

E.1.4 Mixture-averaged properties

Dynamic viscosity and thermal conductivity of the mixture are calculated with semi-empirical formulae

$$\mu = \sum_{j=1}^{n} \frac{Y_j \mu_j}{\Delta_j} \tag{E.12}$$

with

$$\Delta_j = \sum_{k=1}^{n} G_{jk} \frac{M_j}{M_k} Y_k \tag{E.13}$$

where

$$G_{jk} = \frac{1}{\sqrt{8}} \left(1 + \frac{W_j}{W_k}\right)^{-1/2} \left[1 + \left(\frac{\mu_j}{\mu_k}\right)^{1/2} \left(\frac{W_k}{W_j}\right)^{1/4}\right]^2 . \tag{E.14}$$

The mixture-averaged thermal conductivity is evaluated as

$$\lambda = \frac{1}{2}\left[\sum_{j=1}^{n} X_j \lambda_j + \left(\sum_{j=1}^{n} \frac{X_j}{\lambda_j}\right)^{-1}\right]. \tag{E.15}$$

E.2 Laminar diffusion flamelet calculations

The laminar diffusion flamelet equations are derived in mixture fraction space to predict temperature and species distribuations on the centerline of a laminar counterflow diffusion flame. Figure E.1 shows a sketch of a typical laminar counterflow diffusion flame configuration in physical space. In

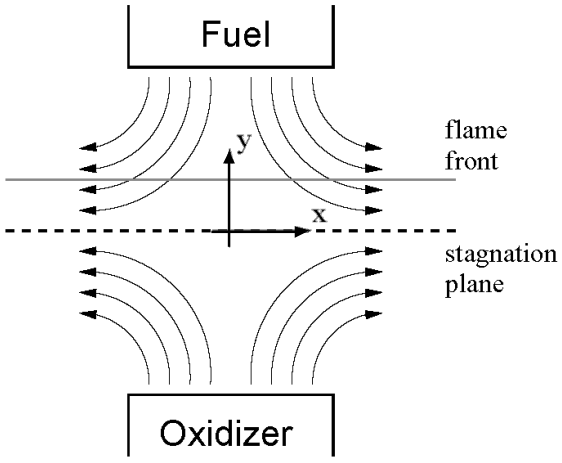

Figure E.1: Sketch of a counterflow diffusion flame

this configuration, the fuel is injected though a nozzle and the oxidizer is injected though a different nozzle. In certain cases, a mixture of both oxidizer and fuel could be injected. As the flow coming from both nozzles are diverted away, a stagnation plane is formed. The flame front typically sits on the fuel side of the stagnation plane. On the centerline of the flame ($x = 0$), the governing equations in physical space (equations described in Chapter. 2) can be rewritten in mixture fraction space, considering the symmetry of the different quantities. These equations in mixture fraction are called flamelet equations (Eq. 3.3), which are solved in the original version of the code [103]. The FlameMaster code has been modified to solve both the centerline modified flamelets (Appendix. A) as well as the curve flamelets (Appendix. C).

Bibliography

[1] U. E. Information Administration, International energy outlook (Jul. 2013).
URL http://www.eia.gov/forecasts/ieo/

[2] H. Wang, M. Frenklach, A detailed kinetic modeling study of aromatics formation in laminar premixed acetylene and ethylene flames, Combustion and Flame 110 (12) (1997) 173 – 221.

[3] G. Blanquart, P. Pepiot-Desjardins, H. Pitsch, Chemical mechanism for high temperature combustion of engine relevant fuels with emphasis on soot precursors, Combustion and Flame 156 (3) (2009) 588–607.

[4] H. Curran, P. Gaffuri, W. Pitz, C. Westbrook, A comprehensive modeling study of iso-octane oxidation, Combustion and Flame 129 (3) (2002) 253 – 280.

[5] C. K. Westbrook, W. J. Pitz, O. Herbinet, H. J. Curran, E. J. Silke, A comprehensive detailed chemical kinetic reaction mechanism for combustion of n-alkane hydrocarbons from n-octane to n-hexadecane, Combustion and Flame 156 (1) (2009) 181 – 199.

[6] H. Pitsch, Large-eddy simulation of turbulent combustion, Annu. Rev. Fluid Mech. 38 (2006) 453–482.

[7] G. Eggernspieler, S. Menon, Large-eddy simulation of pollutant emission in a doe-hat combustor, J. Propuls. Power 20 (6) (2004) 1076 – 1085.

[8] M. Ihme, H. Pitsch, Modeling of radiation and nitric oxide formation in turbulent nonpremixed flames using a flamelet/progress variable formulation, Physics of Fluids 20 (2008).

[9] F. di Mare, W. Jones, K. Menzies, Large eddy simulation of a model gas turbine combustor, Combustion and Flame 137 (3) (2004) 278 – 294.

[10] P. Moin, Advances in large eddy simulation methodology for complex flows, International Journal of Heat and Fluid Flow 23 (5) (2002) 710 – 720.

[11] M. Germano, U. Piomelli, P. Moin, W. H. Cabot, A dynamic subgrid-scale eddy viscosity model, Physics of Fluids A: Fluid Dynamics 3 (7) (1991) 1760–1765.

[12] D. K. Lilly, A proposed modification of the germano subgrid-scale closure method, Physics of Fluids A: Fluid Dynamics 4 (3) (1992) 633–635.

[13] P. Moin, K. Squires, W. Cabot, S. Lee, A dynamic subgrid-scale model for compressible turbulence and scalar transport, Physics of Fluids A: Fluid Dynamics 3 (11) (1991) 2746–2757.

[14] C. D. Pierce, P. Moin, A dynamic model for subgrid-scale variance and dissipation rate of a conserved scalar, Physics of Fluids 10 (12) (1998) 3041–3044.

[15] M. Ihme, H. Pitsch, Prediction of extinction and reignition in nonpremixed turbulent flames using a flamelet/progress variable model, Combustion and Flame 155 (1-2) (2008) 70–89.

[16] N. Peters, Turbulent combustion, Cambridge University Press UK.

[17] T. U. of Adelaide, International sooting flame(isf) workshop (Jul. 2014).
URL http://www.adelaide.edu.au/cet/isfworkshop/

[18] M. Day, S. Tachibana, J. Bell, M. Lijewski, V. Beckner, R. K. Cheng, A combined computational and experimental characterization of lean premixed turbulent low swirl laboratory flames: I. methane flames, Combustion and Flame 159 (1) (2012) 275 – 290.

[19] J. Bell, M. Day, M. Lijewski, Simulation of nitrogen emissions in a premixed hydrogen flame stabilized on a low swirl burner, Proceedings of the Combustion Institute 34 (1) (2013) 1173 – 1182.

[20] F. Perini, E. Galligani, R. D. Reitz, A study of direct and krylov iterative sparse solver techniques to approach linear scaling of the integration of chemical kinetics with detailed combustion mechanisms, Combustion and Flame 161 (5) (2014) 1180 – 1195.

[21] X. Gou, W. Sun, Z. Chen, Y. Ju, A dynamic multi-timescale method for combustion modeling with detailed and reduced chemical kinetic mechanisms, Combustion and Flame 157 (6) (2010) 1111 – 1121.

[22] M. E. Mueller, H. Pitsch, LES model for sooting turbulent nonpremixed flames, Combustion and Flame 159 (6) (2012) 2166–2180.

[23] Y. Xuan, G. Blanquart, Numerical modeling of sooting tendencies in a laminar co-flow diffusion flame, Combustion and Flame 160 (9) (2013) 1657 – 1666.

[24] Y. Xuan, G. Blanquart, M. E. Mueller, Modeling curvature effects in diffusion flames using a laminar flamelet model, Combustion and Flame 0 (0) (2013) –.

[25] X. Yuan, G. Blanquart, A flamelet-based a priori analysis on the chemistry tabulation of polycyclic aromatic hydrocarbons in non-premixed flames, Combustion and Flame (2013) in press.

[26] Y. Xuan, G. Blanquart, Effects of aromatic chemistry-turbulence interactions on soot formation in a turbulent non-premixed flame, Proceedings of the Combustion Institute , under review.

[27] A. Aspden, M. Day, J. Bell, Turbulence-flame interactions in lean premixed hydrogen: transition to the distributed burning regime, Journal of Fluid mechanics 680 (2011) 287–320.

[28] A. Aspden, M. Day, J. Bell, Lewis number effects in distributed flames, Proceedings of the Combustion Institute 33 (1) (2011) 1473 – 1480.

[29] J. B. Bell, A. J. Aspden, M. S. Day, M. J. Lijewski, Numerical simulation of low mach number reacting flows, in: Journal of Physics: Conference Series, Vol. 78, IOP Publishing, 2007, p. 012004.

[30] J. H. Chen, Petascale direct numerical simulation of turbulent combustion-fundamental insights towards predictive models, Proceedings of the Combustion Institute 33 (1) (2011) 99 – 123.

[31] D. O. Lignell, J. H. Chen, P. J. Smith, Three-dimensional direct numerical simulation of soot formation and transport in a temporally evolving nonpremixed ethylene jet flame, Combustion and Flame 155 (12) (2008) 316 – 333.

[32] D. O. Lignell, J. H. Chen, P. J. Smith, T. Lu, C. K. Law, The effect of flame structure on soot formation and transport in turbulent nonpremixed flames using direct numerical simulation, Combustion and Flame 151 (12) (2007) 2 – 28.

[33] K. Narayanaswamy, G. Blanquart, H. Pitsch, A consistent chemical mechanism for oxidation of substituted aromatic species, Combustion and Flame 157 (10) (2010) 1879–1898.

[34] S. Lam, D. Goussis, Understanding complex chemical kinetics with computational singular perturbation, Symposium (International) on Combustion 22 (1) (1989) 931 – 941.

[35] U. Maas, S. Pope, Simplifying chemical kinetics: Intrinsic low-dimensional manifolds in composition space, Combustion and Flame 88 (34) (1992) 239 – 264.

[36] U. Maas, S. Pope, Implementation of simplified chemical kinetics based on intrinsic low-dimensional manifolds, Symposium (International) on Combustion 24 (1) (1992) 103 – 112, twenty-Fourth Symposium on Combustion.

[37] Y. Xuan, B. Savard, B. Bobbitt, G. Blanquart, An efficient semi-implicit time-integration scheme for stiff chemical source terms, Jounal of Computational Physics , under review.

[38] A. Attili, F. Bisetti, M. E. Mueller, H. Pitsch, Formation, growth, and transport of soot in a three-dimensional turbulent non-premixed jet flame, Combustion and Flame (0) (2014) –.

[39] M. Herrmann, G. Blanquart, V. Raman, Flux Corrected Finite Volume Scheme for Preserving Scalar Boundedness in Reacting Large-Eddy Simulations, AIAA Journal 44 (12) (2006) 2879–2886.

[40] S. Verma, Y. Xuan, G. Blanquart, An improved bounded semi-lagrangian scheme for the turbulent transport of passive scalars, Jounal of Computational Physics , under review.

[41] A. Attili, F. Bisetti, Application of a robust and efficient lagrangian particle scheme to soot transport in turbulent flames, Computers and Fluids 84 (0) (2013) 164 – 175.

[42] F. Bisetti, G. Blanquart, M. E. Mueller, H. Pitsch, On the formation and early evolution of soot in turbulent nonpremixed flames, Combustion and Flame 159 (1) (2012) 317–335.

[43] N. Peters, Reducing mechanisms, in: M. D. Smooke (Ed.), Reduced Kinetic Mechanisms and Asymptotic Approximations for Methane-Air Flames, Vol. 384 of Lecture Notes in Physics, Springer Berlin Heidelberg, 1991, pp. 48–67.

[44] T. Lu, C. K. Law, C. S. Yoo, J. H. Chen, Dynamic stiffness removal for direct numerical simulations, Combustion and Flame 156 (2009) 1542–1551.

[45] S. Lam, Singular perturbation for stiff equations using numerical methods, in: Recent Advances in the Aerospace Sciences, Springer, 1985, pp. 3–19.

[46] O. Gicquel, D. Thévenin, M. Hilka, N. Darabiha, et al., Direct numerical simulation of turbulent premixed flames using intrinsic low-dimensional manifolds, Combustion Theory and Modelling 3 (3) (1999) 479–502.

[47] O. Gicquel, N. Darabiha, D. Thvenin, Liminar premixed hydrogen/air counterflow flame simulations using flame prolongation of {ILDM} with differential diffusion, Proceedings of the Combustion Institute 28 (2) (2000) 1901 – 1908.

[48] J. van Oijen, F. Lammers, L. de Goey, Modeling of complex premixed burner systems by using flamelet-generated manifolds, Combustion and Flame 127 (3) (2001) 2124 – 2134.

[49] N. Peters, Local quenching due to flame stretch and non-premixed turbulent combustion, Combust. Sci. Technol 30 (1) (1983) 1–17.

[50] N. Peters, Laminar diffusion flamelet models in non-premixed turbulent combustion, Prog. Energy combust. Sci 2180 (10) (1984) 319–339.

[51] R. W. Bilger, The structure of diffusion flames, Combustion Science and Technology 13 (1-6) (1976) 155–170.

[52] F. A. Williams, Combustion Theory 2nd Edition, Addison-Wesley, 1985.

[53] K. Seshadri, F. Mauss, N. Peters, J. Warnatz, A flamelet calculation of benzene formation in coflowing laminar diffusion flames, Symposium (International) on Combustion 23 (1) (1991) 559 – 566.

[54] K. Claramunt, R. Consul, D. Carbonell, C. Perez-Segarra, Analysis of the laminar flamelet concept for nonpremixed laminar flames, Combustion and Flame 145 (4) (2006) 845 – 862.

[55] B. Connelly, M. Long, M. Smooke, R. Hall, M. Colket, Computational and experimental investigation of the interaction of soot and no in coflow diffusion flames, Proceedings of the Combustion Institute 32 (1) (2009) 777 – 784.

[56] A. W. Cook, J. J. Riley, Subgrid-scale modeling for turbulent reacting flows, Combustion and Flame 112 (4) (1998) 593 – 606.

[57] A. Kempf, A. Sadiki, J. Janicka, Prediction of finite chemistry effects using large eddy simulation, Proceedings of the Combustion Institute 29 (2) (2002) 1979 – 1985.

[58] H. Pitsch, H. Steiner, Scalar mixing and dissipation rate in large-eddy simulations of non-premixed turbulent combustion, Proceedings of the Combustion Institute 28 (1) (2000) 41 – 49.

[59] C. D. Pierce, P. Moin, Progress-variable approach for large-eddy simulation of non-premixed turbulent combustion, Journal of Fluid Mechanics 504 (2004) 73–97.

[60] V. Raman, H. Pitsch, R. O. Fox, Hybrid large-eddy simulation/lagrangian filtered-density-function approach for simulating turbulent combustion, Combustion and Flame 143 (12) (2005) 56 – 78.

[61] M. Chen, M. Herrmann, N. Peters, Flamelet modeling of lifted turbulent methane/air and propane/air jet diffusion flames, Proceedings of the Combustion Institute 28 (1) (2000) 167 – 174.

[62] M. E. Mueller, H. Pitsch, Large eddy simulation subfilter modeling of soot-turbulence interactions, Physics of Fluids 23 (11) (2011) 115104.

[63] R. Barlow, J. Frank, a. Karpetis, J. Chen, Piloted methane/air jet flames: Transport effects and aspects of scalar structure, Combustion and Flame 143 (4) (2005) 433–449.

[64] W. Bilger, R. W. Dibble, Differential molecular diffusion effects in turbulent mixing, Combustion Science and Technology 28 (3-4) (1982) 161–172.

[65] A. L. Sanchez, A. Linan, F. A. Williams, G. Balakrishnan, Theory of structures of hydrogen-air diffusion flames, Combustion Science and Technology 110-111 (1) (1995) 277–301.

[66] R. Barlow, J.-Y. Chen, On transient flamelets and their relationship to turbulent methane-air jet flames, Symposium (International) on Combustion 24 (1) (1992) 231 – 237.

[67] A. Vranos, B. Knight, W. Proscia, L. Chiappetta, M. Smooke, Nitric oxide formation and differential diffusion in a turbulent methane-hydrogen diffusion flame, Symposium (International) on Combustion 24 (1) (1992) 377 – 384, twenty-Fourth Symposium on Combustion.

[68] K. Claramunt, R. Cnsul, C. Prez-Segarra, A. Oliva, Multidimensional mathematical modeling and numerical investigation of co-flow partially premixed methane/air laminar flames, Combustion and Flame 137 (4) (2004) 444 – 457.

[69] L. Verhoeven, W. Ramaekers, J. van Oijen, L. de Goey, Modeling non-premixed laminar co-flow flames using flamelet-generated manifolds, Combustion and Flame 159 (1) (2012) 230 – 241.

[70] H. Pitsch, M. Chen, N. Peters, Unsteady flamelet modeling of turbulent hydrogen-air diffusion flames, Symposium (International) on Combustion 27 (1) (1998) 1057 – 1064, twenty-Seventh Sysposium (International) on Combustion Volume One.

[71] M. Ihme, H. Pitsch, Modeling of radiation and nitric oxide formation in turbulent nonpremixed flames using a flamelet/progress variable formulation, Physics of Fluids 20 (2008).

[72] F. A. Williams, Combustion Theory 1st Edition, Addison-Wesley, 1975.

[73] C. Kortschik, S. Honnet, N. Peters, Influence of curvature on the onset of autoignition in a corrugated counterflow mixing field, Combustion and Flame 142 (12) (2005) 140 – 152.

[74] S. Hu, P. Wang, R. W. Pitz, M. D. Smooke, Experimental and numerical investigation of non-premixed tubular flames, Proceedings of the Combustion Institute 31 (1) (2007) 1093 – 1099.

[75] H. Xu, F. Hunger, M. Vascellari, C. Hasse, A consistent flamelet formulation for a reacting char particle considering curvature effects, Combustion and Flame 160 (11) (2013) 2540 – 2558.

[76] C. Angelberger, D. Veynante, F. Egolfopoulos, Les of chemical and acoustic forcing of a premixed dump combustor, Flow, Turbulence and Combustion 65 (2) (2000) 205–222.

[77] J. Shinjo, Y. Mizobuchi, S. Ogawa, Les of unstable combustion in a gas turbine combustor, in: A. Veidenbaum, K. Joe, H. Amano, H. Aiso (Eds.), High Performance Computing, Vol. 2858 of Lecture Notes in Computer Science, Springer Berlin Heidelberg, 2003, pp. 234–244.

[78] Yunardi, R. Woolley, M. Fairweather, Conditional moment closure prediction of soot formation in turbulent, nonpremixed ethylene flames, Combustion and Flame 152 (3) (2008) 360 – 376.

[79] D. Haworth, M. Drake, S. Pope, R. Blint, The importance of time-dependent flame structures in stretched laminar flamelet models for turbulent jet diffusion flames, Symposium (International) on Combustion 22 (1) (1989) 589 – 597.

[80] B. M. Cetegen, D. R. Bogue, Combustion in a stretched fuel strip with finite rate chemistry, Combustion and Flame 86 (4) (1991) 359 – 370.

[81] H. G. Im, C. K. Law, J. Kim, F. Williams, Response of counterflow diffusion flames to oscillating strain rates, Combustion and Flame 100 (1-2) (1995) 21 – 30.

[82] B. Cuenot, F. Egolfopoulos, T. Poinsot, An unsteady laminar flamelet model for non-premixed combustion, Combustion Theory and Modelling 4 (2000) 77 – 97.

[83] H. G. Im, J. H. Chen, J.-Y. Chen, Chemical response of methane/air diffusion flames to unsteady strain rate, Combustion and Flame 118 (1-2) (1999) 204 – 212.

[84] F. N. Egolfopoulos, C. S. Campbell, Unsteady counterflowing strained diffusion flames: diffusion-limited frequency response, Journal of Fluid Mechanics 318 (1996) 1–29.

[85] J. M. Donbar, J. F. Driscoll, C. D. Carter, Strain rates measured along the wrinkled flame contour within turbulent non-premixed jet flames, Combustion and Flame 125 (4) (2001) 1239 – 1257.

[86] J. M. Donbar, J. F. Driscoll, C. D. Carter, Reaction zone structure in turbulent nonpremixed jet flamesfrom ch-oh {PLIF} images, Combustion and Flame 122 (12) (2000) 1 – 19.

[87] P. E. Vervisch, O. Colin, J.-B. Michel, N. Darabiha, NO Relaxation Approach (NORA) to predict thermal NO in combustion chambers, Combustion and Flame 158 (8) (2011) 1480 – 1490.

[88] M. E. Mueller, H. Pitsch, Large eddy simulation of soot evolution in an aircraft combustor, Physics of Fluids (1994-present) 25 (11) (2013) –.

[89] M. Smooke, C. McEnally, L. Pfefferle, R. Hall, M. Colket, Computational and experimental study of soot formation in a coflow, laminar diffusion flame, Combustion and Flame 117 (1-2) (1999) 117–139.

[90] O. Desjardins, G. Blanquart, G. Balarac, H. Pitsch, High order conservative finite difference scheme for variable density low Mach number turbulent flows, Journal of Computational Physics 227 (15) (2008) 7125–7159.

[91] A. Nonaka, J. B. Bell, M. S. Day, C. Gilet, A. S. Almgren, M. L. Minion, A deferred correction coupling strategy for low mach number flow with complex chemistry, Combustion Theory and Modelling 16 (6) (2012) 1053–1088.

[92] R. S. Barlow, A. N. Karpetis, J. H. Frank, Scalar Profiles and NO Formation in Laminar Opposed-Flow Partially Premixed Methane / Air Flames, Combustion and Flame 2118 (2001) 2102–2118.

[93] C. McEnally, L. Pfefferle, Improved sooting tendency measurements for aromatic hydrocarbons and their implications for naphthalene formation pathways, Combustion and Flame 148 (4) (2007) 210–222.

[94] J. Zhang, C. R. Shaddix, R. W. Schefer, Design of "model-friendly" turbulent non-premixed jet burners for C2+ hydrocarbon fuels, Review of Scientific Instruments 82 (7) (2011) 074101.

[95] W. L. Grosshandler, Radcal, a narrow-band model for radiation calculations in a combustion environment, NIST Technical Note 1402.

[96] R. Bilger, Reaction rates in diffusion flames, Combustion and Flame 30 (0) (1977) 277 – 284.

[97] R. Bilger, The structure of turbulent nonpremixed flames, Symposium (International) on Combustion 22 (1) (1989) 475 – 488.

[98] S. Dworkin, M. Smooke, V. Giovangigli, The impact of detailed multicomponent transport and thermal diffusion effects on soot formation in ethylene/air flames, Proceedings of the Combustion Institute 32 (1) (2009) 1165 – 1172.

[99] Y. Morinishi, O. V. Vasilyev, T. Ogi, Fully conservative finite difference scheme in cylindrical coordinates for incompressible flow simulations, Journal of Computational Physics 197 (2) (2004) 686 – 710.

[100] B. Leonard, A stable and accurate convective modelling procedure based on quadratic upstream interpolation, Computer Methods in Applied Mechanics and Engineering 19 (1) (1979) 59 – 98.

[101] R. Bird, W. Stewart, E. Lightfooot, Transport phenomena, John Wiley and Sons, New York.

[102] Mathur, P. Tondon, S. Saxena, Molecular Physics, Vol. 569, 1967.

[103] H. Pitsch, A C++ computer program for 0D combustion and 1D laminar flame calculations, Technical Report University of Technology (RWTH), Aachen, 1998.

[104] I. Glassman, Combustion, Academic Press, Orlando, FL Second ed. (1987) 370–373.

[105] C. McEnally, L. Pfefferle, Sooting tendencies of nonvolatile aromatic hydrocarbons, Proceedings of the Combustion Institute 32 (1) (2009) 673–679.

[106] C. S. McEnally, L. D. Pfefferle, Sooting tendencies of oxygenated hydrocarbons in laboratory-scale flames., Environmental Science and Technology 45 (6) (2011) 2498–503.

[107] M. D. Smooke, M. B. Long, M. B. Colket, R. J. Hall, Soot Formation in Laminar Coflow Ethylene Diffusion Flames, Combustion and Flame 143.

[108] M. Saffaripour, P. Zabeti, S. B. Dworkin, Q. Zhang, H. Guo, F. Liu, G. J. Smallwood, M. J. Thomson, A Numerical and Experimental Study of a Laminar Sooting Coflow Jet-A1 Diffusion Flame, Proc. Combust. Inst 33 (2011) 601–608.

[109] S. B. Dworkin, Q. Zhang, M. Thomson, N. A. Slavinskaya, U. Riedel, Application of an enhanced PAH growth model to soot formation in a laminar coflow ethylene/air diffusion flame, Combustion and Flame 158 (2011) 1682–1695.

[110] B. A. V. Bennett, C. S. McEnally, L. D. Pfefferle, M. D. Smooke, Computational and experimental study of axisymmetric coflow partially premixed methane/air flames, Combustion and Flame 123 (4) (2000) 522 – 546.

[111] C. McEnally, L. D. Pfefferle, Aromatic and linear hydrocarbon concentration measurements in a non-premixed flame, Combustion science and technology 116-117 (1996) 183–209.

[112] H. Pitsch, N. Peters, A consistent flamelet formulation for non-premixed combustion considering differential diffusion effects, Combustion and Flame 2180 (98) (1998) 26–40.

[113] H. Pitsch, H. Steiner, Large-eddy simulation of a turbulent piloted methane/air diffusion flame (Sandia flame D), Physics of Fluids 12 (10) (2000) 2541.

[114] G. Blanquart, H. Pitsch, A joint volume-surface-hydrogen multi-variate model for soot formation, in: H. Bockhorn, A. DAnna, A.F. Sarofim, H. Wang (Eds.), Karlsruhe University Press, Karlsruhe, 2008.

[115] G. Blanquart, H. Pitsch, Analyzing the effects of temperature on soot formation with a joint volume-surface-hydrogen model, Combustion and Flame 156 (8) (2009) 1614–1626.

[116] S. Kevin, G. Blanquart, Numerical modeling and analysis of hydrocarbon soot formation pathways, Proceedings of 7th US Combustion Meeting Altanta, Georgia.

[117] E. V. Kalmthout, D. Veynante, Direct numerical simulations analysis of flame surface density models for nonpremixed turbulent combustion, Physics of Fluids 10 (9) (1998) 2347–2368.

[118] J. O. Hirschfelder, J. Heimerl, Molecular theory of gases and liquids, John Wiley and Sons New York.

[119] G. Blanquart, H. Pitsch, Modeling autoignition in non-premixed turbulent combustion using a stochastic flamelet approach, Proceedings of the Combustion Institute 30 (2) (2005) 2745 – 2753.

[120] S. Sreedhara, K. Lakshmisha, Autoignition in a non-premixed medium: Dns studies on the effects of three-dimensional turbulence, Proceedings of the Combustion Institute 29 (2) (2002) 2051 – 2059.

[121] S. Ishizuka, On the behavior of premixed flames in a rotating flow field: Establishment of tubular flames, Proceedings of the Combustion Institute 20 (1985) 287 – 294.

[122] P. Wang, J. A. Wehrmeyer, R. W. Pitz, Stretch rate of tubular premixed flames, Combustion and Flame 145 (12) (2006) 401 – 414.

[123] C. J. Montgomery, C. Yang, A. R. Parkinson, J.-Y. Chen, Selecting the optimum quasi-steady-state species for reduced chemical kinetic mechanisms using a genetic algorithm, Combustion and Flame 144 (12) (2006) 37 – 52.

[124] M. D. Smooke, Reduced Kinetic Mechamisms and Asymptotic Approximation for Mathane-Air Flames, Springer-Verlag, Berline, 1991.

[125] N. Peters, B. Rogg, Reduced Kinetic Mechanisms for Applications in Combustion Systems, Springer-Verlag, Berline, 1993.

[126] S. Viswanathan, H. Wang, S. B. Pope, Numerical implementation of mixing and molecular transport in les/pdf studies of turbulent reacting flows, Journal of Computational Physics 230 (17) (2011) 6916 – 6957.

[127] S. B. Pope, Turbulent flows, Cambridge university press, 2000.

[128] B. Savard, G. Blanquart, An a priori model for the effective species lewis numbers in premixed turbulent flames, Combustion and Flame (0) (2014) –.

[129] D. C. Wilcox, Turbulence modeling for CFD, Vol. 2, DCW industries La Canada, CA, 1998.

[130] P. Donde, V. Raman, M. E. Mueller, H. Pitsch, Les/pdf based modeling of sootturbulence interactions in turbulent flames, Proceedings of the Combustion Institute 34 (1) (2013) 1183 – 1192.

[131] A. W. Cook, J. J. Riley, A subgrid model for equilibrium chemistry in turbulent flows, Physics of Fluids 6 (8) (1994) 2868–2870.

[132] M. Oevermann, Ein finite-volumen-verfahren auf unstrukturierten dreiecksgittern zur berechnung turbulenter diffusionsflammen in kompressiblen strömungsfeldern, FORSCHUNGSBERICHT-DEUTSCHES ZENTRUM FUR LUFT UND RAUMFAHRT.

[133] D. Pfuderer, A. Neuber, G. Frchtel, E. Hassel, J. Janicka, Turbulence modulation in jet diffusion flames: Modeling and experiments, Combustion and Flame 106 (3) (1996) 301 – 317.

[134] J. C. Ferreira, Flamelet modeling of stabilization in turbulent non-premixed combustion eth, Dissertation.

[135] R. S. Barlow, C. D. Carter, Raman/rayleigh/lif measurements of nitric oxide formation in turbulent hydrogen jet flames, Combustion and Flame 97 (3) (1994) 261–280.

[136] R. Barlow, J. Frank, Effects of turbulence on species mass fractions in methane/air jet flames, Symposium (International) on Combustion 27 (1) (1998) 1087 – 1095.

[137] H. Pitsch, Large-eddy simulation of turbulent combustion, Annu. Rev. Fluid Mech. 38 (2006) 453–482.

[138] C. Chou, J-Y. Chen, C. G. Yam, and K. D. Marx, Numerical Modeling of NO Formation in Laminar Bunsen Flames - A Flamelet Approach, Combustion and Flame 114 (34) (1998) 420 – 435.

[139] S. Chan, J. Yin, B. Shi, Structure and extinction of methane-air flamelet with radiation and detailed chemical kinetic mechanism, Combustion and Flame 112 (3) (1998) 445 – 456.

[140] A. Heyl, H. Bockhorn, Flamelet modeling of no formation in laminar and turbulent diffusion flames, Chemosphere 42 (57) (2001) 449 – 462.

[141] H. Pitsch, C. M. Cha, S. Fedotov, Flamelet modelling of non-premixed turbulent combustion with local extinction and re-ignition, Combustion Theory and Modelling 7 (2) (2003) 317–332.

[142] P. Vedula, P. Yeung, R. Fox, Dynamics of scalar dissipation in isotropic turbulence: A numerical and modelling study, J. Fluid Mech 433 (2001) 29.

[143] Z. Luo, C. S. Yoo, E. S. Richardson, J. H. Chen, C. K. Law, T. Lu, Chemical explosive mode analysis for a turbulent lifted ethylene jet flame in highly-heated coflow, Combustion and Flame 159 (1) (2012) 265 – 274.

[144] S. Sreedhara, K. Lakshmisha, Assessment of conditional moment closure models of turbulent autoignition using dns data, Proceedings of the Combustion Institute 29 (2) (2002) 2069 – 2077.

[145] L. Smith, R. Dibble, L. Talbot, R. Barlow, C. Carter, Laser raman scattering measurements of differential molecular diffusion in turbulent nonpremixed jet flames of {H2CO2} fuel, Combustion and Flame 100 (12) (1995) 153 – 160.

[146] R. Barlow, C. Carter, Relationships among nitric oxide, temperature, and mixture fraction in hydrogen jet flames, Combustion and Flame 104 (3) (1996) 288 – 299.

[147] M. E. Mueller, G. Blanquart, H. Pitsch, A joint volume-surface model of soot aggregation with the method of moments, Proceedings of the Combustion Institute 32 (1) (2009) 785 – 792.

[148] A. D. Abid, N. Heinz, E. D. Tolmachoff, D. J. Phares, C. S. Campbell, H. Wang, On evolution of particle size distribution functions of incipient soot in premixed ethyleneoxygenargon flames, Combustion and Flame 154 (4) (2008) 775 – 788.

[149] B. Oktem, M. P. Tolocka, B. Zhao, H. Wang, M. V. Johnston, Chemical species associated with the early stage of soot growth in a laminar premixed ethyleneoxygenargon flame, Combustion and Flame 142 (4) (2005) 364 – 373.

[150] M. Ihme, C. M. Cha, H. Pitsch, Prediction of local extinction and re-ignition effects in non-premixed turbulent combustion using a flamelet/progress variable approach, Proceedings of the Combustion Institute 30 (1) (2005) 793 – 800.

[151] P. Chatterjee, J. L. de Ris, Y. Wang, S. B. Dorofeev, A model for soot radiation in buoyant diffusion flames, Proceedings of the Combustion Institute 33 (2) (2011) 2665 – 2671.

[152] Y. Ju, H. Matsumi, K. Takita, G. Masuya, Combined effects of radiation, flame curvature, and stretch on the extinction and bifurcations of cylindrical ch4/air premixed flame, Combustion and Flame 116 (4) (1999) 580 – 592.

[153] D. Messig, F. Hunger, J. Keller, C. Hasse, Evaluation of radiation modeling approaches for non-premixed flamelets considering a laminar methane air flame, Combustion and Flame 160 (2) (2013) 251 – 264.

[154] T. Williams, C. Shaddix, K. Jensen, J. Suo-Anttila, Measurement of the dimensionless extinction coefficient of soot within laminar diffusion flames, International Journal of Heat and Mass Transfer 50 (78) (2007) 1616 – 1630.

[155] G. L. Hubbard, C. L. Tien, Infrared mean absorption coefficient of luminous flames and smoke, Journal of Heat Transfer 100 (1978) 235.

[156] C. L. Tien, K. Y. Lee, A. J. Stretton, Radiation Heat Transfer, SFPE Handbook of Fire Protection Engineering, 3rd ed., National Fire Protection Association, Quincy, MA, 2002.

[157] C. R. Shaddix, J. Zhang, Joint temperature-volume fraction statistics of soot in turbulent non-premixed jet flames, Proceedings of the 8th U.S. Combustion Meeting (2013).

[158] N. Burali, X. Y., G. Blanquart, A new radiation model for tabulated chemistry based on steady state flamelets, Proceedings of the Western States Section Meeting of the Combustion Institute Fort Collins, Colorado.

[159] C. Meneveau, T. S. Lund, W. H. Cabot, A lagrangian dynamic subgrid-scale model of turbulence, Journal of Fluid Mechanics 319 (1996) 353–385.

[160] J. Reveillon, L. Vervisch, Response of the dynamic les model to heat release induced effects, Physics of Fluids 8 (8) (1996) 2248–2250.

[161] J. Jimenez, A. Linan, M. M. Rogers, F. J. Higuera, A priori testing of subgrid models for chemically reacting non-premixed turbulent shear flows, Journal of Fluid Mechanics 349 (1997) 149–171.

[162] C. Wall, B. J. Boersma, P. Moin, An evaluation of the assumed beta probability density function subgrid-scale model for large eddy simulation of nonpremixed, turbulent combustion with heat release, Physics of Fluids 12 (10) (2000) 2522–2529.

[163] G. Balarac, H. Pitsch, V. Raman, Development of a dynamic model for the subfilter scalar variance using the concept of optimal estimators, Physics of Fluids 20 (3).

[164] S. N. Laboratories, International workshop on measurement and computation of turbulent nonpremixed flames.

URL http://www.ca.sandia.gov/TNF

[165] A. Masri, R. Bilger, Turbulent diffusion flames of hydrocarbon fuels stabilized on a bluff body, Symposium (International) on Combustion 20 (1) (1985) 319 – 326, twentieth Symposium (International) on Combustion.

[166] T. Landenfeld, A. Kremer, E. Hassel, J. Janicka, T. Schfer, J. Kazenwadel, C. Schulz, J. Wolfrum, Laser-diagnostic and numerical study of strongly swirling natural gas flames, Symposium (International) on Combustion 27 (1) (1998) 1023 – 1029, twenty-Seventh Sysposium (International) on Combustion Volume One.

[167] W. Meier, S. Prucker, M.-H. Cao, W. Stricker, Characterization of turbulent hytvair jet diffusion flames by single-pulse spontaneous raman scattering, Combustion science and technology 118 (4-6) (1996) 293–312.

[168] V. Bergmann, W. Meier, D. Wolff, W. Stricker, Application of spontaneous raman and rayleigh scattering and 2d lif for the characterization of a turbulent ch4/h2/n2 jet diffusion flame, Applied Physics B 66 (4) (1998) 489–502.

[169] R. Barlow, G. Fiechtner, C. Carter, J.-Y. Chen, Experiments on the scalar structure of turbulent jet flames, Combustion and Flame 120 (4) (2000) 549–569.

[170] A. Masri, R. Dibble, R. Barlow, The structure of turbulent nonpremixed flames revealed by raman-rayleigh-lif measurements, Progress in Energy and Combustion Science 22 (4) (1996) 307–362.

[171] W. Jones, V. Prasad, Large eddy simulation of the sandia flame series (d–f) using the eulerian stochastic field method, Combustion and Flame 157 (9) (2010) 1621–1636.

[172] M. Sheikhi, T. Drozda, P. Givi, F. Jaberi, S. Pope, Large eddy simulation of a turbulent non-premixed piloted methane jet flame (sandia flame d), Proceedings of the Combustion Institute 30 (1) (2005) 549–556.

[173] T. Peeters, P. Stroomer, J. De Vries, D. Roekaerts, C. Hoogendoorn, Comparative experimental and numerical investigation of a piloted turbulent natural-gas diffusion flame, in: Symposium (International) on Combustion, Vol. 25, Elsevier, 1994, pp. 1241–1248.

[174] N. Qamar, Z. T. Alwahabi, Q. N. Chan, G. Nathan, D. Roekaerts, K. D. King, Soot volume fraction in a piloted turbulent jet non-premixed flame of natural gas, Combustion and Flame 156 (7) (2009) 1339–1347.

[175] B. F. Magnussen, An investigation into the behavior of soot in a turbulent free jet c2h2-flame, Symposium (International) on Combustion 15 (1) (1975) 1415 – 1425, fifteenth Symposium (International) on Combustion.

[176] B. Magnussen, B. Hjertager, J. Olsen, D. Bhaduri, Effects of turbulent structure and local concentrations on soot formation and combustion in {C2H2} diffusion flames, Symposium (International) on Combustion 17 (1) (1979) 1383 – 1393, seventeenth Symposium (International) on Combustion.

[177] H. Becker, S. Yamazaki, Soot concentration field of turbulent propane/air diffusion flames, Symposium (International) on Combustion 16 (1) (1977) 681 – 691.

[178] H. Becker, D. Liang, Visible length of vertical free turbulent diffusion flames, Combustion and Flame 32 (0) (1978) 115 – 137.

[179] H. Becker, S. Yamazaki, Entrainment, momentum flux and temperature in vertical free turbulent diffusion flames, Combustion and Flame 33 (0) (1978) 123 – 149.

[180] H. Becker, D. Liang, Total emission of soot and thermal radiation by free turbulent diffusion flames, Combustion and Flame 44 (13) (1982) 305 – 318.

[181] J. Kent, S. Bastin, Parametric effects on sooting in turbulent acetylene diffusion flames, Combustion and Flame 56 (1) (1984) 29 – 42.

[182] S. Jeng, G. Faeth, Predictions of mean scalar properties in turbulent propane diffusion flames, Journal of Heat Transfer 106 (4) (1984) 891–893.

[183] J. Gore, G. Faeth, Structure and spectral radiation properties of turbulent ethylene/ air diffusion flames, Symposium (International) on Combustion 21 (1) (1988) 1521 – 1531, twenty-First Symposuim (International on Combustion).

[184] J. Gore, G. Faeth, Structure and radiation properties of luminous turbulent acetylene/air diffusion flames, Journal of heat transfer 110 (1) (1988) 173–181.

[185] Y. Sivathanu, J. Gore, J. Dolinar, Transient scalar properties of strongly radiating jet flames, Combustion science and technology 76 (1-3) (1991) 45–66.

[186] Y. Zheng, J. P. Gore, Measurements and inverse calculations of spectral radiation intensities of a turbulent ethylene/air jet flame, Proceedings of the Combustion Institute 30 (1) (2005) 727–734.

[187] W. Flower, An investigation of soot formation in axisymmetric turbulent diffusion flames at elevated pressure, Symposium (International) on Combustion 22 (1) (1989) 425 – 435.

[188] S. Turns, J. Lovett, H. Sommer III, Visualization of soot zones in turbulent diffusion flames, Combustion and flame 77 (3) (1989) 405–409.

[189] S. Turns, J. Lovett, Measurements of oxides of nitrogen emissions from turbulent propane jet diffusion flames, Combustion science and technology 66 (4-6) (1989) 233–249.

[190] S. R. Turns, F. H. Myhr, Oxides of nitrogen emissions from turbulent jet flames: Part ifuel effects and flame radiation, Combustion and Flame 87 (3) (1991) 319–335.

[191] S. R. Turns, R. V. Bandaru, Carbon monoxide emissions from turbulent nonpremixed jet flames, Combustion and flame 94 (4) (1993) 462–468.

[192] S.-Y. Lee, S. R. Turns, R. J. Santoro, Measurements of soot, oh, and pah concentrations in turbulent ethylene/air jet flames, Combustion and Flame 156 (12) (2009) 2264–2275.

[193] K. Young, C. Stewart, J. Moss, Soot formation in turbulent nonpremixed kerosine-air flames burning at elevated pressure: Experimental measurement, Symposium (International) on Combustion 25 (1) (1994) 609 – 617, twenty-Fifth Symposium (International) on Combustion.

[194] B. Hu, B. Yang, U. O. Koylu, Soot measurements at the axis of an ethylene/air non-premixed turbulent jet flame, Combustion and flame 134 (1) (2003) 93–106.

[195] B. Yang, U. O. Koylu, Detailed soot field in a turbulent non-premixed ethylene/air flame from laser scattering and extinction experiments, Combustion and Flame 141 (1) (2005) 55–65.

[196] C. R. Shaddix, J. Zhang, W. Scheffer, J. Doom, J. C. Oefelein, S. Kook, L. M. Pickett, H. Wang, Understanding and predicting soot generation in turbulent non-premixed jet flames, Sandia National Laboratories Report, Sand2010-7178.

[197] M. Delichatsios, Transition from momentum to buoyancy-controlled turbulent jet diffusion flames and flame height relationships, Combustion and Flame 92 (4) (1993) 349 – 364.

[198] S. R. Turns, An Introduction to Combustion: Concepts and Applications, McGraw-Hill, Boston, 2000.

[199] J. Murphy, C. Shaddix, Soot properties and species measurements in a two-meter diameter jp-8 pool fire, Sandia National Laboratories Report, SAND2003–8246.

[200] K. T. Kim, J. G. Lee, B. D. Quay, D. A. Santavicca, The dynamic response of turbulent dihedral v flames: An amplification mechanism of swirling flames, Combustion Science and Technology 183 (2) (2010) 163–179.

[201] J. C. Keck, Rate-controlled constrained-equilibrium theory of chemical reactions in complex systems, Progress in Energy and Combustion Science 16 (2) (1990) 125 – 154.

[202] L. Shunn, F. Ham, P. Moin, Verification of variable-density flow solvers using manufactured solutions, Journal of Computational Physics 231 (9) (2012) 3801–3827.

[203] C. D. Pierce, Progress-variable approach for large-eddy simulation of turbulent combustion, Ph.D. thesis, Stanford University (2001).

[204] R. D. Falgout, U. M. Yang, hypre: A library of high performance preconditioners, in: Computational ScienceICCS 2002, Springer, 2002, pp. 632–641.